On the Design and Realization of Broadband Seismic Metamaterials

Yi Zeng

Doctoral School **Chemistry-Mechanics-Materials-Physics**

University Department **Institut Jean Lamour**

Thesis defended by **Yi Zeng**

in **May, 11 2023**

In order to become Doctor from Université de Lorraine

Academic field: **Physics**

On the Design and Realization of Broadband Seismic Metamaterials

---

Committee Members

President of Jury

Prof. Ning Hu	Professor, Hebei University of Technology

Referees

Prof. Yan Pennec	Professor, Université de Lille
Prof. Xiaoming Zhou	Professor, Beijing Institute of Technology

Examiners

Prof. Abdelkrim Khelif	Director of Research CNRS, Université de Franche-Comté

Supervisors

Prof. Yue-Sheng Wang	Professor, Tianjin University
Prof. Badreddine Assouar	Director of Research CNRS, Université de Lorraine

Keywords: seismic metamaterial; Rayleigh waves; bandgap; wide-low frequency; Inverse dispersion; local resonance; inertial amplification

Mots clés: Métamatériau sismique; ondes de Rayleigh; bande interdite; large-basse fréquence; dispersion inverse; résonance locale; amplification inertielle

祸兮福之所倚,福兮祸之所伏.

-《老子》

Misfortune, that is where happiness depends;

happiness, that is where misfortune underlies.

-Tao Te Ching

Acknowledgments

The work of this thesis was completed under the careful guidance of my supervisors, Prof. Yue-Sheng Wang and Prof. Badreddine Assouar, whose rigorous academic attitude and scientific working methods have given me great help and influence. I would like to express my sincere gratitude to Prof. Yue-Sheng Wang and Prof. Badreddine Assouar for their care and guidance over the past four years.

I would like to express my sincere gratitude to Professor Yan-Feng Wang for his valuable advice on my research work and thesis, and for his great care and help in my study and life.

Professor Yi-Ze Wang has given me many valuable comments on my scientific work and thesis, and I would like to express my heartfelt thanks to him.

During the period of working in the lab and writing my thesis, Dr. Li-Yun Cao, Dr. Yi-Fan Zhu, Dr. Sheng Wan, Dr. Shuo-Wei An, Dr. Xiao-Shuang Li, Dr. Krupali Donda and students Hong-Tao Zhou, Tong Guo, Shu-Yan Zhang and Xuan-Bo Miao gave me enthusiastic help in my work in the thesis. I would like to express my gratitude to them.

I would also like to thank my family, Ms. Jia-Ping Chen and Mr. Xian-Zhong Zeng, for their understanding and support, which allowed me to focus on completing my studies at school. Special thanks to Miss. Keke Deng for your constant companionship and encouragement.

Finally, I would like to thank the National Natural Science Foundation of China (Nos. 12021002, 12122207, 11991031, 11991032 and 41974059), the CARNOT ICEEL Institute Project, and the China Scholarship Council (No. 202006250084) for their financial support.

Contents

List of Figures

List of Tables

Chapter 1 State of the Art

1.1 Introduction

Earthquake refers to the vibration of the earth's surface caused by the vibration of a place or a certain area on the earth's surface or below the earth's surface. [1-5] It is usually caused by some natural phenomena such as crustal movement, meteorite impact and volcanic eruption. It can also be caused by human activities such as nuclear weapon explosions. The catastrophic earthquakes known so far are all caused by violent movement of the earth's crust. Earthquakes can cause surface faults, surface tremors, surface liquefaction, landslides, aftershocks and even tsunamis. [2,4-7] The time of earthquake occurrence, the number and intensity of aftershocks will make the disaster more serious. Compared with other natural disasters, earthquakes cause a great threat to the safety of people's lives and properties. In ancient times, such as the Jiajing Earthquake that occurred on January 1556, 830,000 people were killed and immeasurable economic losses were caused. [8] Modern cities are characterized by dense buildings and high occupancy rates, as well as problems such as underdeveloped early warning systems and lack of public awareness of earthquake risks, which all exacerbate the severity of earthquake disasters.

After the founding of the PRC, the Haicheng Earthquake occurred in Liaoning Province. [9-12] This is the only successful case where the government evacuated people in an orderly manner and significantly reduced the damage based on an accurate prediction of an earthquake. The number of casualties from the earthquake was 18,308, representing only 0.22% of the total number of people in the quake area, with only 0.02% of the total number of fatalities. A year later, the Tangshan Earthquake claimed the lives of more than 242,000 people. [10,13,14] Although there were numerous seismic observatories in the area where the earthquake occurred, the short-term forecasts completely failed. Because there was little foreshock activity prior to the Tangshan Earthquake and other precursor phenomena appeared late. As a result, the Tangshan earthquake was also listed as one of the top ten natural disasters of the 20th century. As of today, accurate earthquake prediction is still difficult to achieve.

Seismic resistant technology is an important method of protecting target buildings by designing and arranging them before earthquakes. [15-17] Conventional seismic

resistant technology resists the forces of earthquakes by increasing the strength, stiffness and ductility of the structural elements of the building, specifically by increasing the cross-sectional size of the structural elements and adding reinforced concrete walls to resist earthquakes. [15-20] In recent years, new seismic resistant technology have become more "flexible", using seismic isolation and damping devices such as rubber bearings [21-25] and dampers [15,26-29], as shown in Fig. 1-1, to isolate and dissipate seismic energy. When an earthquake occurs, the damping devices dissipate the seismic wave energy in the building by compressing, bending and deflecting it in a way that will change its structure and shape, thus protecting the building.

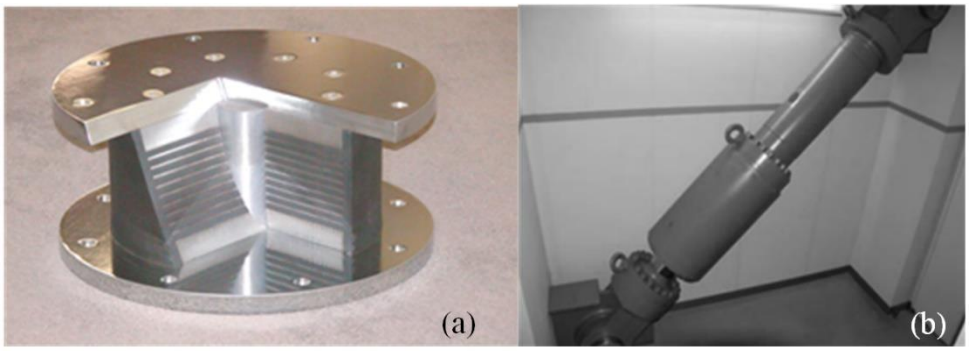

Figure 1-1 Seismic isolations [30]

(a) Rubber bearing. (b) Viscous dampers

In contrast, seismic metamaterials, [31-39] proposed in recent years, can control seismic wave based on local resonance and Bragg scattering due to the bandgap properties. [40-49] In the frequency range of the bandgap, seismic metamaterials can isolate seismic wave or even change the direction of seismic wave propagation. Seismic metamaterials can be placed around or at the base of a protected building to strongly attenuate seismic waves. [35,50-54] Because the resonant frequencies of most man-made buildings are below 20 Hz, [31,55] the bandgaps of most seismic metamaterials are in this range. However, there is still relatively little research into the design and theory of seismic metamaterials that can operate in the wide low-frequency range.

This thesis uses theoretical model analyses, numerical simulations and experimental measurements to study seismic metamaterials with a wide low-frequency bandgap, which further advances seismic metamaterials towards practical applications.

This work is supported by the National Natural Science Foundation of China (NSFC), the China Scholarship Council (CSC) and la Région Grand Est.

1.2 Earthquake prediction, early warning and resistant technology

1.2.1 **Earthquake prediction and early warning technology**

Earthquake prediction [9,56-63] refers to the prediction of the time, location and magnitude of earthquakes that will occur. It is specifically subdivided into long-term, medium-term and short-term forecasts. Although the scientific community can identify and focus on monitoring and prevention of "key earthquake risk areas" for long-term predictions on a decadal scale, and strengthen preparations for earthquake prevention and mitigation in key areas for medium-term predictions, there is still an urgent need to solve the problems of scientific methods and accuracy of earthquake predictions, especially short-term predictions. In particular, short-term prediction is still a worldwide scientific challenge. Current methods for predicting earthquakes are mainly based on empirical analysis rather than physical mechanisms, mainly because of three main reasons: [56,60-62]

1. Although man-made space probes have flown more than 20 billion kilometers in space and may even fly out of the solar system in the future, the deepest excavation on earth is only 10 kilometers.

2. Earthquakes are small probability events. Although the annual number of earthquakes is nearly one million, the time interval between two major earthquakes in the same region is long. In some areas, the interval is even as high as tens of thousands of years, and the observation of geophysics is only a few decades, so it is difficult to generalize a reliable law.

3. The difficulty of earthquake prediction experiments. Real earthquake sources are difficult to be accurately excited in experiments, so it is difficult to obtain accurate experimental data for summarizing experience.

The earthquake early warning technology [64-69], which has been commonly used in recent years, can also be realized under certain conditions to send warning messages to areas at a certain distance from the earthquake source several seconds or even tens of seconds in advance, thus reducing human casualties. The principle is that near-field seismic waves include longitudinal and transverse waves, where longitudinal waves are

faster than transverse waves, but longitudinal waves are much less destructive than transverse waves. When the seismograph near the source detects the longitudinal wave and the trailing transverse wave, the time difference between the two can be used to calculate the time it takes for the transverse wave to reach the nearby areas. The time information is sent to various terminals, including but not limited to cell phones, TVs and smart watches, using developed communication networks. Thus, the earthquake warning can be sent to the nearby areas several seconds or even tens of seconds in advance.

On September 14, 1995, this technology enabled the release of earthquake alerts 72 seconds in advance for the Guerrero earthquake, which was the first time an earthquake alert was released to the public. [66,69,70] In China, after the Wenchuan earthquake, the Chinese government has increased the construction of earthquake alerts in areas with high seismicity. As a result, research and technology in earthquake warning has advanced rapidly. In Sichuan Province, the earthquake warning system can be sent to the people nearby through village radios, TVs and mobile phone apps. When a 6.1 magnitude earthquake struck Lushan County, Ya'an City, Sichuan Province on 1 June 2022, the system issued an alert at the fourth second after the earthquake had occurred. The city of Ya'an and the city of Chengdu received the alert 9 and 29 seconds before the arrival of the seismic waves, respectively. [71] However, there are certain problems with earthquake warning technology, i.e., the closer the epicenter, the greater the hazard but the shorter the warning time.

1.2.2 **Earthquake resistant technology**

Earthquake resistant technology has been an important method since ancient times to protect target buildings. For example, during the Ming Dynasty in China, the rulers designed the construction of the Forbidden City in Beijing to incorporate glutinous rice layer with damping effect to achieve earthquake resistance. This allowed the Forbidden City in Beijing to remain intact after many earthquakes over hundreds of years. [72-74] Conventional seismic resistant technologies are designed to resist earthquake forces by increasing the strength, stiffness, and ductility of structural elements in buildings. [15-20] Although they are effective, they have the following problems:

1. For large earthquakes, the safety of buildings needs urgent consideration.

2. It is difficult to apply to buildings that have suffered earthquake damage or other equipment and instruments inside the buildings that need to be protected.

3. The increase in the cross-sectional size of structural members and the thickening of reinforced concrete walls will make the building cost much higher.

4. The current building technology uses more high-strength and lightweight materials, which makes the cross-section of the structural members of the building smaller, the height of the building higher and the structural span of the building larger, thus making it difficult for the traditional Earthquake resistant technology to be adopted.

In recent years, the new earthquake resistant technologies (vibration isolation and damping technologies) have become more " use softness to conquer strength". The seismic isolation technology [30,75-79] refers to the use of seismic isolation devices for fixing between the building foundation and the main body of the building. Seismic isolation devices can extend the self-oscillation period of a building to reduce the seismic acceleration response of the building. In earthquakes, seismic isolation devices can isolate seismic waves in the building foundation from the main body of the building, thus achieving protection for the building. [30,76] The seismic damping technology [80-89] refers to the use of seismic damping devices (e.g., connecting elements) to fix and connect certain locations in the building. Seismic damping devices can dissipate seismic wave energy in buildings by changing their structure and shape through compression, bending, and deflection to protect the buildings. [81,82] The excellent earthquake resistant devices should have the following characteristics: [30,76]

1. Sufficient load-bearing capacity. Because earthquake resistant devices are generally placed between building structures, they need to carry most or even the entire mass of the building structure in the vertical direction.

2. Excellent seismic isolation capacity. As an earthquake resistant device, this performance is essential, especially the horizontal stiffness should be variable.

3. Better resetting ability. Good resetting ability can make the building automatically return to its original position after the occurrence of flat motion.

4. Good damping ability. Earthquake resistant devices need to have damping energy dissipation characteristics to lose the seismic wave energy transmitted from the bottom of the building to the superstructure.

At present, there are some limitations of earthquake resistant devices:

1. The earthquake resistant effect for high-rise buildings is not obvious.

2. It needs to be specifically analyzed according to the vibration direction of the building structure. The propagation direction of seismic waves will have a significant impact on the vibration direction of the building structure.

3. High-rise buildings are susceptible to wind effects. The horizontal stiffness of seismically isolated buildings is generally small, but high-rise buildings are susceptible to large wind loads and require high shear resistance.

4. The service life of some earthquake resistant devices is well below the life cycle of the building, requiring replacement at a later stage.

5. Earthquake resistant devices can take up a lot of space and can affect the aesthetics and functionality of a building.

6. Most earthquake resistant device is costly.

1.3 Seismic metamaterials

In the early 1990s, Sigalas, Economou [90] and Kushwaha [91] introduced the concept of phononic crystals based on photonic crystals. Acoustic waves or elastic waves in a phononic crystal will not propagate in certain frequency range due to Bragg scattering. Theoretical studies on periodic structures can be traced back to 1883, when Floquet [92] studied wave propagation in one-dimensional periodic spring oscillators. In 1928, Bloch [93] proposed Bloch's theorem, which extended Floquet's conclusion to three dimensions. Already in 1946, Brillouin suggested that mechanical and electromagnetic waves are analogous and uniform. Wave propagation in periodic discrete structures was studied and discussed in the book *Wave Propagation in Periodic Structures*. [94] In 1995, Martinez-Sala et al. [95] tested the acoustic transmission properties of a periodically arranged sculpture "Flowing Melody". The existence of an acoustic bandgap was experimentally demonstrated for the first time. The most distinctive feature of a phononic crystal is the bandgap property. The band structure of a phononic crystal consists of bandgaps and bands. In the frequency range of the bandgap, waves cannot propagate in phononic crystals. In the frequency range of the passband, waves can propagate normally in phononic crystals.

In 2000, Liu et al. [96] proposed an acoustic metamaterial based on the local resonance mechanism. The lowest bandgap of this acoustic metamaterial corresponds

to a wavelength 300 times the lattice constant, achieving the purpose of "small size control of large wavelength". The frequency of the bandgap of the acoustic metamaterial is almost independent of the periodicity of the unit cell, but closely related to the resonance frequency of the resonance unit cell. The flat bands and the bandgaps can be found in the band structures. The group velocity of the wave in the acoustic metamaterial is zero at this time, so the wave cannot propagate in the acoustic metamaterial. Since then such artificial structures composed of periodic materials have been widely studied and designed for engineering applications such as subwavelength imaging, [97-99] cloak, [100-104] energy harvesting, [105-107] and vibration & noise reduction. [39,49,108-114] Based on the photonic crystals, phononic crystals and metamaterials, the metasurface [115-121] and topological phononic crystals [122-127] have been proposed in recent years.

In recent years, researchers inspired by the phononic crystals and acoustic metamaterials, have proposed seismic metamaterials. Its protection of buildings is achieved in a new way: Seismic metamaterials are placed around buildings to reflect and attenuate seismic waves for protection purposes.

1.3.1 **An overview of seismic metamaterials**

After an earthquake occurs, mechanical vibrations generated at the source propagate inside and on the surface of the Earth thus forming seismic waves. [1-5] Seismic waves can be simply distinguished into two main categories: bulk waves and surface waves. In the mid- and far-field regions of an earthquake, bulk waves are coupled on the half-space surface to form Rayleigh surface waves (also known as Rayleigh waves). [1,3-5,16,57,59,60] The amplitude of its mass vibration decays exponentially along the ground depth direction, so that the energy of Rayleigh waves is almost entirely concentrated near the ground. [128] Rayleigh waves are usually found far from the earthquake source. Rayleigh waves have large amplitude, slow decay, and can propagate in the earth's surface many times after a large earthquake and still have great energy. [129,130] Therefore, in the mid- and far-field regions of an earthquake, Rayleigh waves are more destructive to buildings than bulk waves and can threaten buildings at a greater distance. So, the design and research of seismic metamaterials for Rayleigh waves is of great importance.

Seismic metamaterials, usually based on local resonance and Bragg scattering, use

the bandgap properties [40-49] to isolate and attenuate seismic waves or even change the direction of seismic waves propagation. Seismic metamaterials can be placed around or at the bottom of a building to control seismic waves. The resonant frequency of most man-made buildings is below 20 Hz, [31,55] so most of the current seismic metamaterials are design for this range. In addition, researchers often use common materials on construction sites to reduce the cost of seismic metamaterials, such as steel, industrial rubber, and concrete.

1.3.2 Research background of seismic metamaterials

There are a large number of theoretical studies and experimental verifications on seismic metamaterials. Seismic metamaterials can be divided into three categories according to the type of seismic waves they mainly target: seismic metamaterials that mainly target seismic bulk waves (referred to as bulk wave seismic metamaterials), seismic metamaterials that mainly target seismic Lamb waves (referred to as Lamb wave seismic metamaterials), and seismic metamaterials that mainly target seismic Rayleigh waves (referred to as Rayleigh wave seismic metamaterials).

Bulk wave seismic metamaterials are mostly composed of three-dimensional periodic structures and generally have a complete bandgap, which can attenuate seismic transverse and longitudinal waves from any direction. [31,32,36,131] Lamb wave seismic metamaterials are mostly composed of one- and two-dimensional periodic structures and generally have a complete bandgap. [34,50,132] Seismic Lamb waves are coupled by seismic transverse and longitudinal waves in plate-like geological layers and are mostly found in earthquakes with sources close to the Earth's surface. Seismic Lamb waves are also of great interest because they can carry large amounts of energy to propagate to longer distances, thus threatening buildings in the mid and far fields. [132] When the thickness of the plate layer is large enough, both symmetric and antisymmetric waves of Lamb waves will propagate as Rayleigh waves on the surface of the plate. Therefore, Lamb wave seismic metamaterials can also be used to control Rayleigh waves under certain conditions. [33,34,50,51,132] Rayleigh wave seismic metamaterials are also mostly composed of one- and two-dimensional periodic structures, generally with directional bandgaps or complete bandgaps, and are mainly used to attenuate seismic Rayleigh waves in the low-frequency range. [35,52,133-138]

1.3.2.1 Bulk wave seismic metamaterials

As shown in Fig. 1-2, [139-143] the bulk wave seismic metamaterial is generally placed at the base of a building as a building foundation or around the building to isolate seismic waves.

Bao et al. [144] designed a one-dimensional seismic metamaterial composed of concrete and rubber. The band structure of this seismic metamaterial was calculated using the transfer matrix method and the parameter optimization was given. As shown in Fig. 1-3(a), to verify the effectiveness of this seismic metamaterial, they used the finite element method to compare the dynamic response of a seven-story frame structure on a concrete foundation, a seismic foundation and the seismic metamaterial, considering the seismic waves propagating from any direction. The results show that the seismic metamaterial can well attenuate the seismic waves in horizontal, vertical and oblique incidence directions and efficiently reduce the dynamic response in the seven-story frame structure due to the bandgap property of the seismic metamaterial.

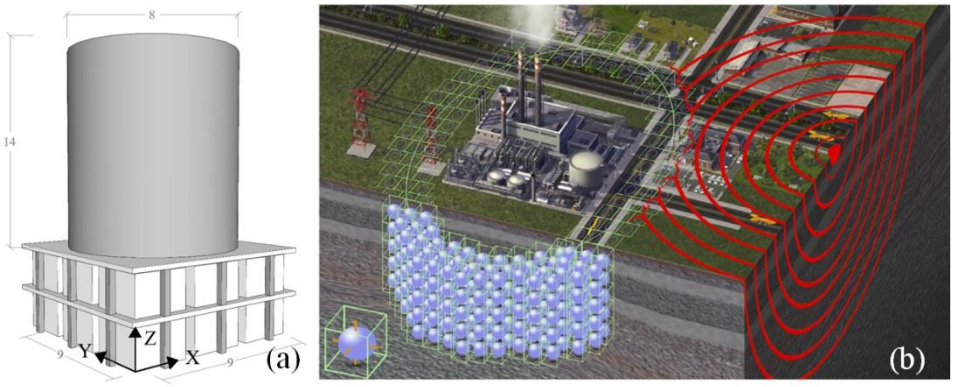

Figure 1-2 Placement of bulk wave seismic metamaterials [142,143]

(a) At the bottom of the building and (b) around the building

Xiang et al. [145] proposed a one-dimensional seismic metamaterial consisting of a periodic arrangement of reinforced concrete and rubber. They calculated the band structure of the seismic metamaterial and analyzed the generation mechanism of the bandgap based on the Bloch-Floquet theorem. As shown in Fig. 1-3(b), they designed a lab-scaled sample based on the finite element model and experimentally demonstrated its attenuation effect on seismic waves. The results of the dynamic response of the upper frame show that the seismic metamaterials are able to attenuate environmental

vibrations, seismic loads and harmonic excitations well in the bandgap. They pointed out that although it is difficult to design seismic metamaterials with low-frequency bandgaps, the attenuation of seismic waves by seismic metamaterials is obvious. Experimental data show that in the bandgap, seismic metamaterials can reduce the horizontal acceleration of seismic waves by about 50% and can reduce the vertical acceleration by about 16%.

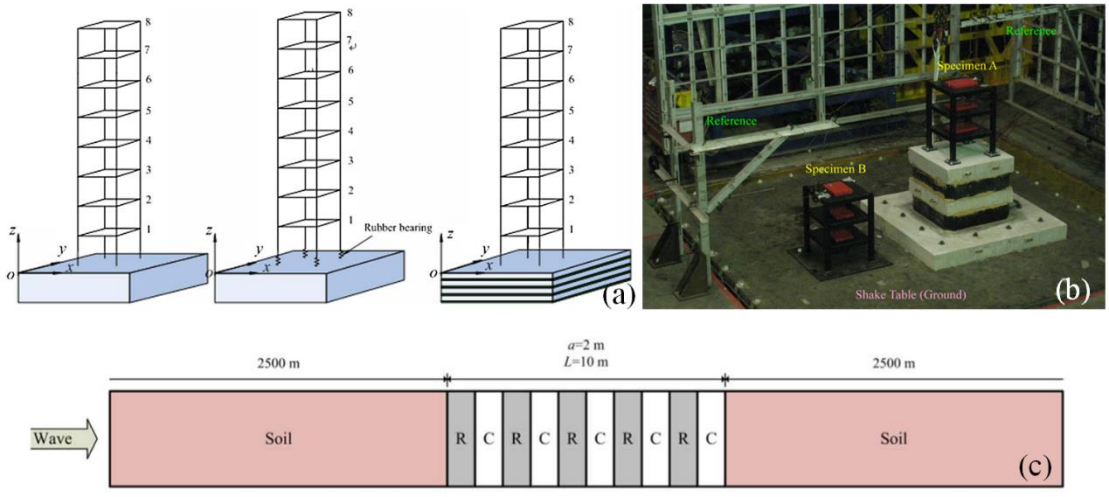

Figure 1-3 The 1D bulk waves seismic metamaterials

(a) Comparison of concrete foundation, seismic isolations and seismic metamaterial. [144] (b) Experimental layout of the seismic metamaterial. [145] (c) study on the transmission of bulk waves in the seismic metamaterial [37]

A one-dimensional seismic metamaterial composed of two elastic materials was also proposed by Geng et al. [37] The variation of the seismic metamaterial under different material combination conditions was analyzed using an analytical model. It was found that the larger the width of the bandgap, the smaller the center frequency of the seismic metamaterial when the difference between the mass density and wave velocity of the two materials is large. Moreover, reducing the filling rate of the softer material is also beneficial to the attenuation of seismic waves. This is consistent with the findings of Zhou et al. [146] in phononic crystals. In addition, as shown in Fig. 1-3(c), they constructed numerical models of seismic metamaterials using the finite element method to calculate the responses of seismic metamaterials to seismic waves. The results show that the increase in the number of unit cells of seismic metamaterials leads

to the enhancement of the ability of seismic metamaterials to attenuate seismic waves. The combination of unit cells with different lattice constants leads to an increase in the attenuation frequency range of the seismic metamaterials.

Yan et al. [147] designed a three-dimensional three-component seismic metamaterial consisting of steel, rubber and concrete from the concept of the phononic metamaterial. The unit cell of the seismic metamaterial is shown in the left of Fig. 1-4(a). Its central section is shown in the right of Fig. 1-4(a). They calculated the band structure of the seismic metamaterial using the finite element software ABAQUS and found that it has a complete bandgap in the range of 32.9-35.6 Hz. In addition, they used the seismic metamaterial for field experimental verification. It is found that the seismic metamaterial can well attenuate the seismic transverse and longitudinal waves due to the bandgap property. Compared with the traditional reinforced concrete foundation, the seismic metamaterial can reduce the acceleration by more than 90%. The experimental results are basically consistent with the simulation results.

Aravantinos-Zafiris et al. [148] proposed a three-dimensional seismic metamaterial consisting of periodically arranged concrete pillars. The unit cell is shown in Fig. 1-4(b). The left shows the three-dimensional view and the right shows the central section of the unit cell. The six concrete pillars are connected at the center of the unit cell by a solid with a very small cross section. They calculated the band structure of the seismic metamaterial by the time-domain finite difference method. It was found it can be used to attenuate seismic waves below 50 Hz when the structural parameters of the concrete pillars are appropriate. When the lattice constant is 10 m, the complete bandgap is 7.9-124 Hz.

Achaoui et al. [142] proposed a three-dimensional seismic metamaterial with a unit cell consisting of a rubber pillar, a steel sphere and concrete. The unit cell is shown in the lower left corner in Fig. 1-4(c). The steel sphere and concrete are connected by six rubber pillars. Each sphere is free to translate and rotate in the cavity in which it is located. This seismic metamaterial can be placed around a building or used as the foundation of a building. They used asymptotic formulas for the eigenfrequencies associated with the steel sphere to infer the frequency of the low-frequency bandgap. The band structure is also calculated using the finite element software COMSOL Multiphysics. A wide bandgap of 8-49 Hz can be obtained for seismic metamaterials with a lattice constant of 1 m. The transmission results show that the seismic

metamaterial based on the local resonance mechanism can attenuate seismic waves well.

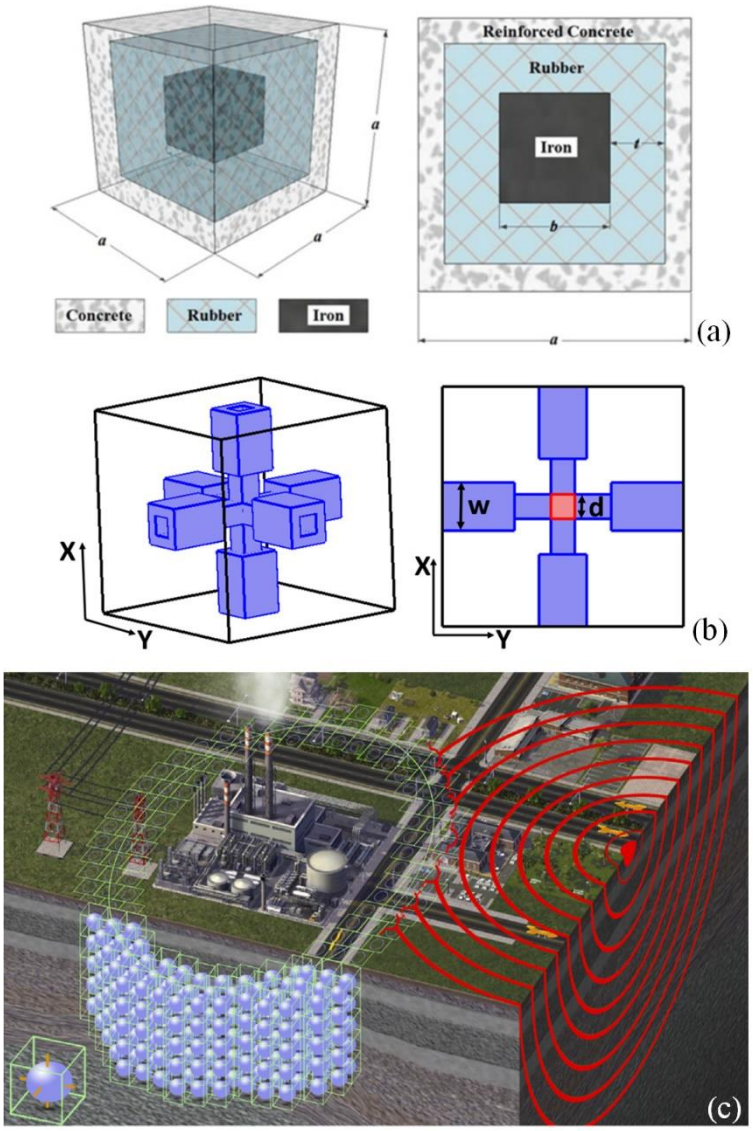

Figure 1-4 The 3D bulk waves seismic metamaterials

(a) The unit cell of the 3D seismic metamaterial consisting of concrete, rubber, and iron. [147] (b) the unit cell of the 3D seismic metamaterial consisting of six concrete pillars. [148] (c) the unit cell of the 3D seismic metamaterial consisting of concrete, rubber pillars and iron ball [142]

The literature mentioned in this section is all about bulk wave seismic metamaterials. It can be found that such seismic metamaterials can separate the building from the building foundation where seismic waves can propagate to. Thus, the building

is protected from the seismic waves during an earthquake. However, the seismic metamaterials arranged at the bottom of the building need to hold the weight of the building. So, the structural strength of seismic metamaterials should be higher. These seismic metamaterials can isolate most seismic waves and can be an excellent seismic technology for major infrastructures, such as nuclear power plants and important military facilities.

1.3.2.2 Rayleigh wave seismic metamaterials

As shown in Fig. 1-5, Rayleigh wave seismic metamaterials are typically placed around buildings to protect them by isolating seismic wave propagation. This seismic metamaterial generally has a half-space substrate, so the sound cone is found in the band structure. The sound cone is usually necessary to study the surface waves. The bandgaps for surface waves are within the sound cone. [35,132,134,149-152] These seismic metamaterials can be simply divided into two categories, one in which the artificial structure is placed on the ground (including half-buried), and one in which the artificial structure is completely buried in the soil.

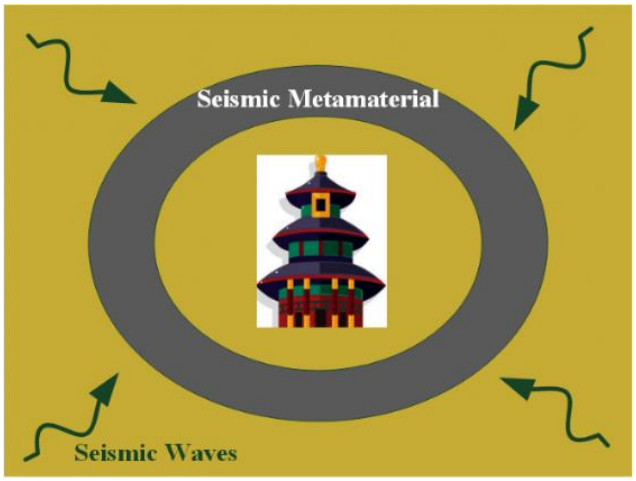

Figure 1-5 Placement of seismic metamaterial

The first one is the Rayleigh wave seismic metamaterials formed by placing artificial structures on the ground (including half-buried). These seismic metamaterials originate from phononic crystals that control surface waves in devices such as MEMS. The phononic crystals can be used to filter Rayleigh waves at the millimeter-micron scale. [42,43,153-156]

Colombi et al. [133] and Roux et al. [136] found that forest can be considered as a complex resonator for attenuating low-frequency seismic Rayleigh waves. The test site is shown in Fig. 1-6(a), [136] where the periodically arranged yellow dots are seismometers distributed on the boundaries of rapeseed fields (upper area) and forests (lower area). They found that the good attenuation effect in the experiments depends on the longitudinal resonance and flexural resonance of trees with different heights, shapes and thicknesses. Meanwhile, the simulation results using the finite element method demonstrated that the seismic metamaterial composed of trees and the soil substrate produces low-frequency bandgaps due to its longitudinal resonance and flexural resonance of the trees.

Colombi et al. [35] introduced the Rainbow trapping effect to propose a seismic metawedge composed of trees of different heights arranged in a gradient on the soil as shown in Fig. 1-6(b). The different resonant frequencies of trees of different heights make the seismic metawedge can attenuate seismic Rayleigh waves in a large wide-frequency range. The simulation results show that the seismic metawedge can completely attenuate the Rayleigh waves when Rayleigh waves are incident from the left side; when incident from the right side, the seismic metamaterial converts the Rayleigh waves into bulk waves.

Muhammad et al. [157] considered that trees would have different branches as shown in Fig. 1-6(c). Seismic metamaterials consisting of these two types of trees arranged periodically were studied. They obtained the bandgap of Rayleigh waves using the sound cone based on the finite element method for calculations. The results show that both types of trees can well attenuate Rayleigh waves in the bandgap. In addition, they introduced the metawedge and also found that the seismic metawedges completely attenuate the Rayleigh waves when Rayleigh waves are incident from the left side; when incident from the right side, the Rayleigh waves are converted to bulk waves. Therefore, they suggested that afforestation could be an effective way to resist earthquakes.

To obtain wide low-frequency bandgaps, Zeng et al. [135] replaced trees with steel pillars. They compared seismic metamaterials made of circular, rectangular, and I-shaped pillars arranged periodically on the soil. They found that seismic metamaterials composed of I-shaped pillars are easy to obtain wider bandgaps for low-frequencies

Rayleigh waves. Du et al. [134] and Zeng et al. [137] also proposed seismic metamaterials consisting of periodic H-shaped fractal pillars and Matryoshka-like pillars on a half space, respectively. These metamaterials can obtain bandgaps for Rayleigh wave in multiple frequencies due to that there are multilevel resonance structure in each unit cell. As the number of resonance levels increases, the bandgaps at lower frequencies are also obtained. As shown in Fig. 1-6(d), Wu et al. [158] also proposed to replace trees with concrete pillars. They compared seismic metamaterials consisting of periodic concrete pillars standing on the ground, rubber-coated concrete pillars buried in the ground, and a combination of these two. They found that the half-buried seismic metamaterial is easy to obtain a bandgap at low frequency. In addition, after introducing the metawedge, they also found that the seismic metamaterials completely attenuate the Rayleigh waves when they are incident from the left side; when they are incident from the right side, the Rayleigh waves are converted into bulk waves.

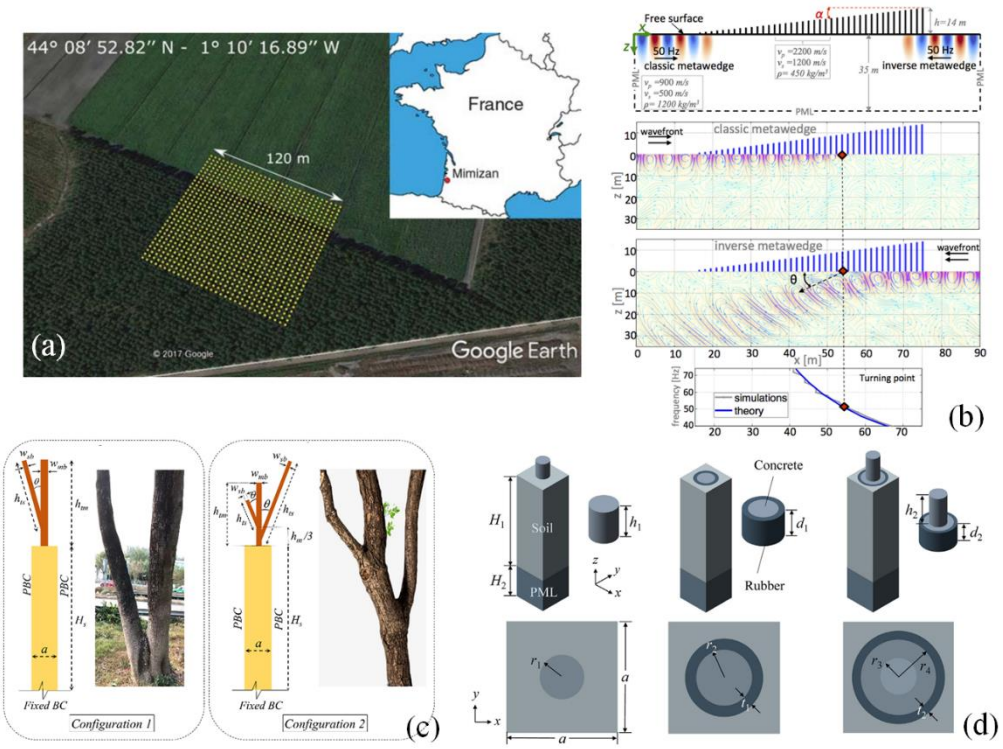

Figure 1-6 The Rayleigh waves seismic metamaterial

(a) Experimental layout of forest seismic metamaterials. [136] (b) Comparison of three seismic metamaterial. [35] (c) Effects of tree collaterals and bifurcations on seismic metamaterials. [157] (d) Comparison of three seismic metamaterial[158]

Colquitt et al. [151] presented the typicality problem of standing rods on thin plates and half-space substrates. They theoretically explained the interaction between the waves in the substrate (in the plate and half-space) and the resonator structure (rods) on the substrate. They calculated the band structures of a metamaterial composed of periodic standing rods on a plate and half-space as shown in Fig. 1-7(a) by the improved Spectral Element Method. They found that the bending and compression resonance of the rod caused by the interaction of the elastic wave with the rod attenuates the wave propagation, both in the plate and in the half space. Pu et al. [116] proposed a multiple scattering formulation to study the interaction between Rayleigh waves and a plate standing on an elastic half-space surface as shown in Fig. 1-7(b). They found that the scattered wave field caused by the bending resonance of the plate has an attenuating effect on Rayleigh waves. These works all provide a theoretical basis for the study of Rayleigh wave seismic metamaterials.

Liu et al. [39] proposed that topology optimization can be used to design Rayleigh wave seismic metamaterials. As shown in Fig. 1-7(c), part of the region above the half-space can be set as a design domain consisting of many small pixels. A "0" in a pixel means no solid material, while a "1" means a solid material is present. Finally, all "1" pixels form the topology of the seismic metamaterial. Rayleigh wave seismic metamaterials with an ultra-wide and ultra-low frequency bandgap composed of two materials were realized by topology optimization with set constraints and boundary restrictions. They found that the bandgap of the topologically optimized seismic metamaterial can have a minimum frequency as low as 1.6 Hz and a relative bandwidth of 150%. They also found that optimized structures consisting of "1" pixels generally have large masses and slim connecting axes. This kind of structure can enhance the local resonance capability of the structure and reduces the frequency of the local resonance bandgap.

The second one is Rayleigh wave seismic metamaterials formed by burying artificial structure in the soil. In 1999, Meseguer et al. [40] drilled two-dimensional honeycomb lattice and triangular lattice cylindrical holes in the marble surface to measure the attenuation effects of such holes on Rayleigh waves. They demonstrated experimentally that this seismic metamaterial can attenuate Rayleigh waves in a frequency range. They demonstrated that this is due to the bandgap property of the

seismic metamaterial by using theoretical calculations. They proposed for the first time that phononic crystals can be used to attenuate seismic Rayleigh waves, and also provided an experimental basis for the study of seismic metamaterials.

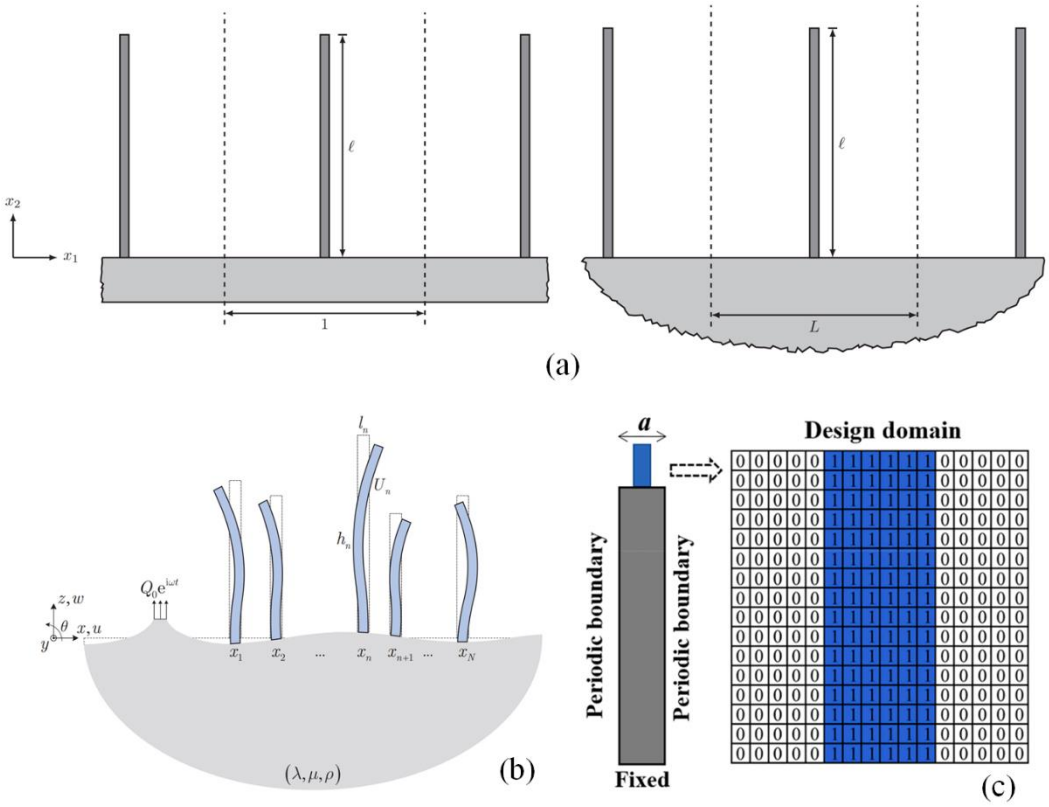

Figure 1-7 Study of the pillar-shaped seismic metamaterials

(a) Periodic rods on an elastic thin plate and a half space. [151] (b) Periodic plates on an elastic half space. [116] (c) Topology optimization design of the pillar-shaped seismic metamaterial[39]

Krödel et al. [152] proposed an elastic metamaterial based on a kind of local resonance structure. This resonant structure is shown in the left of Fig. 1-8(a), where soft material connects the upper and lower ends of the steel mass to the aluminum box. This elastic metamaterial can obtain a wide attenuation zone using multiple resonant structures. Using simulations and experiments shown in the right of 1-8(a), they found that the attenuation effect of this elastic metamaterial increases with the number of resonant structures.

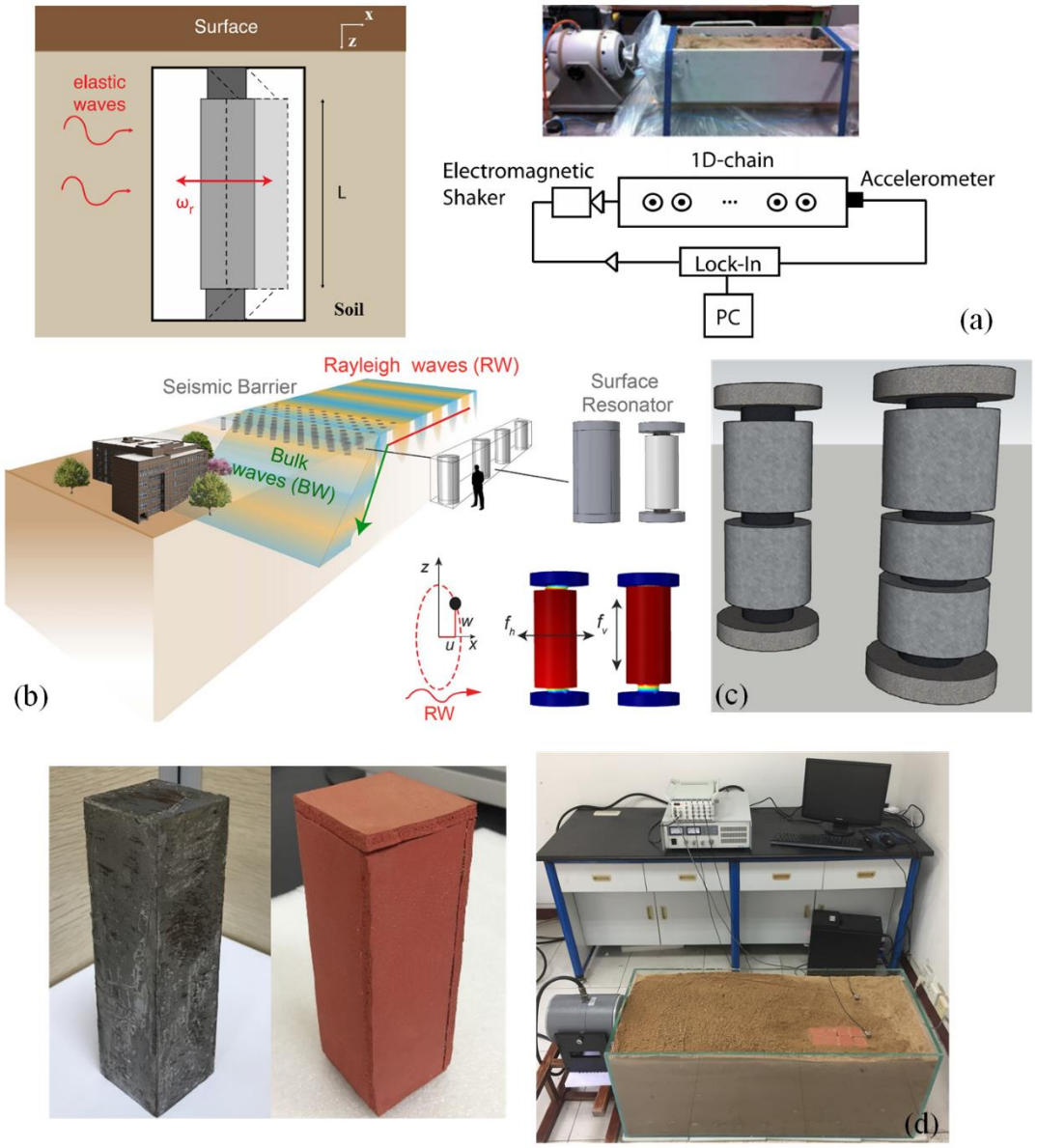

Figure 1-8 The buried seismic metamaterial

(a) The buried seismic metamaterials and experimental layout. [136,152] (b) The transmission of the Rayleigh waves in the buried seismic metamaterials. [149] (c) The buried seismic metamaterials with multiple mass resonance. [159] (d) The simple buried seismic metamaterials and experimental layout [160]

Palermo et al. [149] introduced a similar resonant structure to design a Rayleigh wave seismic metamaterial as shown in Fig. 1-8(b). They found that the seismic metamaterial can convert seismic Rayleigh waves to bulk waves and proposed an analytical model based on effective medium theory to explore the mechanism of this

mode conversion. They used model experiments to demonstrate the attenuation effect of this seismic metamaterial on Rayleigh waves. The results show that this seismic metamaterial can reduce the surface motion by up to 50% in the bandgap. Palermo et al. [159] proposed a Rayleigh wave seismic metamaterial composed of multi-mass resonators as shown in Fig. 1-8(c). This seismic metamaterial can attenuate seismic Rayleigh waves in multiple frequency ranges. They designed a multi-mass resonator with minimum total mass to attenuate seismic Rayleigh waves in an ultra-wide frequency range by using genetic algorithm.

Zeng et al. [160] proposed a Rayleigh wave seismic metamaterial using rubber covered steel blocks and periodically buried in the ground as shown in the left of Fig. 1-8(d) for a unit cell. This seismic metamaterial has a simple and easy-to-implement structure with a wide low-frequency bandgap with a relative bandwidth of about 1. The 1:30 lab-scale experiments shown in the right of Fig. 1-8(d). Experimental results and simulations results show that this seismic metamaterial can attenuate Rayleigh waves well within the bandgap.

Liu et al. [161] proposed that a topological optimization framework based on genetic algorithm and finite element method can be used to design Rayleigh wave seismic metamaterials. As shown in Fig. 1-9, this seismic metamaterial is composed of a periodic artificial structure buried in the ground. The part of the area below the half space can be set as a design domain consisting of many small pixels. The "light blue area" within the pixel indicates the substrate material (soil), while the "red area" indicates that it contains the design material (steel, concrete or lead). The "light blue area" and the "red area" form the topology of the seismic metamaterial. The topological optimization results show that as the mass density of the scatterer represented by the "red region" increases, the surface modes of the seismic metamaterial become richer and the bandgap becomes larger. The bandgap also widens as the depth of the design domain increases, especially the high-frequency bandgap. They found a feature of the optimal artificial structure with the first bandgap: there is a main scatterer and multiple small scatterers in the structure, with the main scatterer located at the center of the design domain within the unit cell and the multiple small scatterers near the surface. The main scatterer determines the lower boundary of the first bandgap, and the small scatterers determine the upper boundary of the first bandgap.

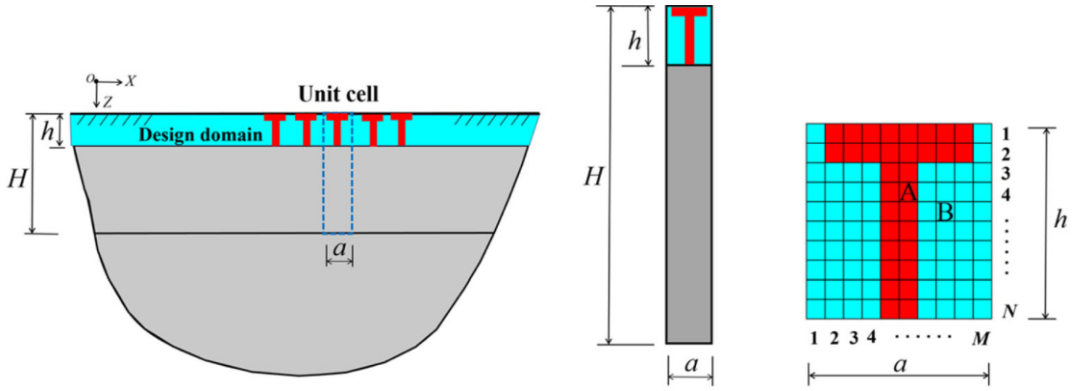

Figure 1-9 Topological optimization of buried seismic metamaterials [161]

This subsection presents some of the research on Rayleigh wave seismic metamaterials. There is also a large amount of related work, [36,38,49,51,53,54,131,138,162-164] which is not detailed here.

1.3.2.3 Lamb wave seismic metamaterials

As shown in Fig. 1-5, Lamb wave seismic metamaterials are generally placed around buildings to isolate the seismic waves. [165,166] As mentioned earlier, when the thickness of the plate waveguide is large enough, both symmetric and antisymmetric Lamb waves modes will propagate as Rayleigh waves on the surface of the plate. Therefore, Lamb wave seismic metamaterials can also be used to control seismic Rayleigh waves under certain conditions.

Brûlé et al. [33] proposed a seismic metamaterial composed of periodic holes in the ground as shown in Fig. 1-10(a). They calculated the band structure of the seismic metamaterial using the Mindlin plate model. [167] The first large-scale field experiments on seismic metamaterials were designed. As shown in the right of Fig. 1-10(a), a large exciter is used to generate the seismic source on one side of the seismic metamaterial, and three-component velocimeters are used to measure the elastic waves on the surface. The results show that the experimental results are consistent with simulations using the Mindlin plate model: this seismic metamaterial can shield elastic waves around 50 Hz.

Miniaci et al. [34] comparatively studied three Lamb waves seismic metamaterials with different unit cells as shown in Fig. 1-10(b). Using the finite element software COMSOL Multiphysics, they calculated and compared the band structures of these three seismic metamaterials for different geometrical parameters. The attenuation of

seismic metamaterials to seismic Lamb and Rayleigh waves are analyzed respectively. In addition, they discussed the effect of viscoelasticity of soil on seismic wave attenuation based on simulation analysis of large-scale seismic metamaterials. They pointed out that considering the wavelength of low-frequency seismic waves, the depth of the structure buried in the soil substrate can be deepened to increase the attenuation effect. The viscoelasticity of the soil plays a positive role in the effect of seismic wave attenuation.

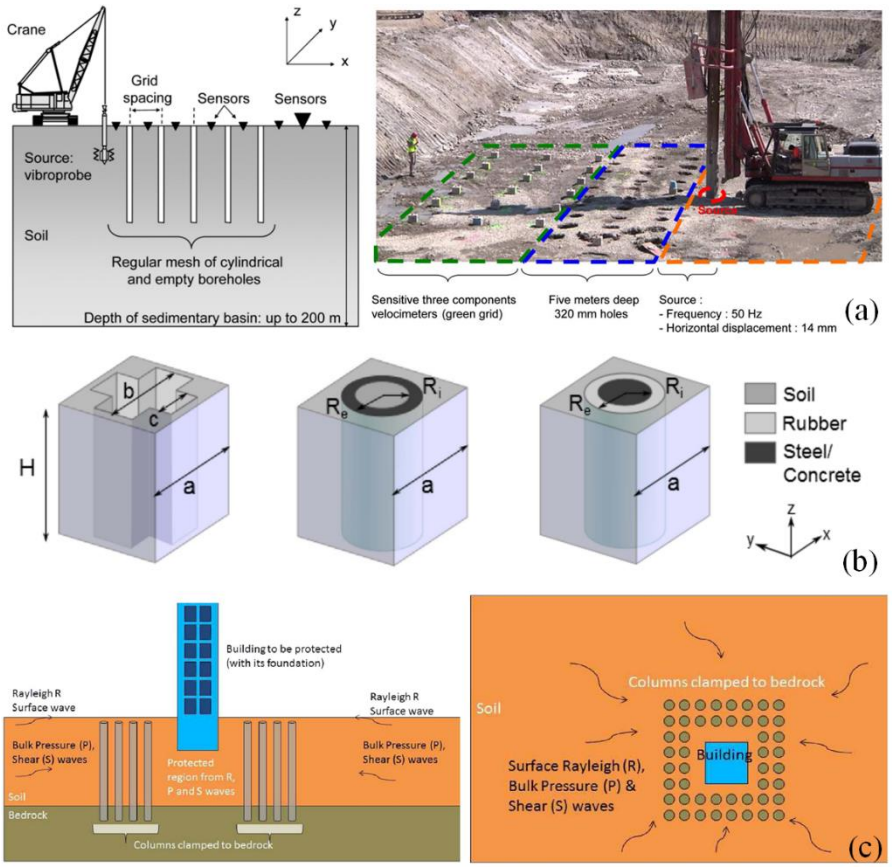

Figure 1-10 The Lamb waves seismic metamaterial

(a) The seismic metamaterial formed by periodically arranging holes in soil. [33] (b) Comparison of three seismic metamaterial. [34] (c) The seismic metamaterials formed by periodically arranging pillars on bedrock [50]

As shown in Fig. 1-10(c), Achaoui et al. [50] introduced a plate structure model with the bottom being fixed to design a two-dimensional seismic metamaterial. In the Kirchhoff-Love thin-plate model with the bottom surface being fixed, the periodic structure easily obtains a zero-frequency bandgap, i.e., a bandgap starting from 0 Hz.

In practical applications, the seismic metamaterials can attenuate ultra-low frequency seismic waves by periodically inserting pillars into the soil and clamping pillars in a giant bedrock. In a sedimentary basin environment with a giant bedrock at the bottom and a soil depth of 15 meters, this seismic metamaterial can attenuate seismic waves below 30 Hz.

Du et al. [132] proposed a two-dimensional seismic metamaterial composed of periodically arranging square concrete pillars in soil. Attenuation of Lamb and Rayleigh waves can be achieved. For Lamb waves, they found that the square-shape pillar is easier to obtain a wider complete bandgap compared to cylindrical pillar. For Rayleigh waves, they found that this seismic metamaterial also has a low-frequency bandgap after introducing a half-space substrate. In addition, they discussed the effects of geometrical and material parameters on the width of the bandgap.

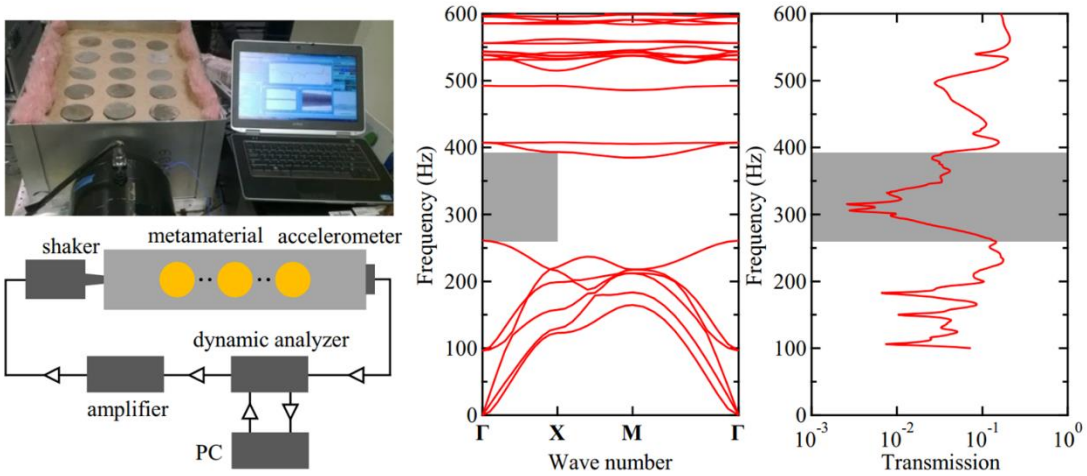

Figure 1-11 The Lab-scale experiments [168]

Chen et al. [168] proposed a two-dimensional seismic metamaterial that can attenuate low-frequency seismic waves in multilayered soils. They demonstrated the attenuation effect of the seismic metamaterial constituted of periodic pillars in soil by using the lab-scale experiments shown in Fig. 1-11. The attenuation frequency range coincides with the bandgap calculated by numerical simulation. They introduced multiple layered soil. It was found that zero-frequency bandgap can be achieved when the underlying material can clamp the pillars.

The literature mentioned in this section are Lamb wave seismic metamaterials,

which can also attenuate Rayleigh waves at sufficient depth. These seismic metamaterials can improve the seismic performance of existing buildings such as ancient buildings. For Lamb waves, these seismic metamaterials can have a significant effect. For Rayleigh waves, these seismic metamaterials need to be buried at sufficient depth to be effective. To achieve attenuation of seismic waves in the low frequency range, specific conditions need to be met, such as a giant bedrock.

1.4 Conclusions

The state of art and literature review introduces the main hazards of earthquakes to humans, as well as earthquake prediction, early warning methods, earthquake resisting techniques, and points out the shortcomings in these methods and techniques. Then the seismic metamaterials, detailing bulk waves, Lamb waves, and Rayleigh wave seismic metamaterials are presented in this chapter.

Chapter 2 Methods

Seismic metamaterials are composed of periodic artificial structures, similar to crystals in solid state physics. [91,169-174] Therefore, seismic waves in seismic metamaterials have dispersive properties, also known as dispersion curves or band structures. [90,91,169] Usually there is a special phenomenon in the band structure, which is the bandgap. [40-44,46,139,146,154,155,166,171,175-177] When the seismic wave frequency falls inside the bandgap, it is difficult for the seismic waves to propagate in the seismic metamaterial. When it falls outside the bandgap, seismic waves can propagate in it. Most of the proposed ones in this thesis are Rayleigh wave seismic metamaterials, so there are deep substrates in the model and sound cone in the band structure to obtain the surface wave bands. [42,43,153-156,177-181] This thesis focuses on the study of the properties of seismic metamaterials using the finite element method. The results of the finite element method are also demonstrated by the analytical method of the transfer matrix to the simplified model. Therefore, this chapter presents the physical principles, finite element method and transfer matrix method involved in the calculation of the properties of seismic metamaterials.

2.1 Basic theory

The basic theory involved in the calculation of the properties of metamaterials have been described in detail in several works [141,153,169,179,182-185] and are only briefly described in this section.

2.1.1 Elastic wave equation and Rayleigh waves

In solid media that is continuous, linearly elastic with small deformation, homogeneous and isotropic, the elastic wave equation is: [184,185]

$$\rho\ddot{\boldsymbol{u}} = [\lambda + 2\mu]\nabla(\nabla \cdot \boldsymbol{u}) - \nabla \times [\mu\nabla \times \boldsymbol{u}], \tag{2-1}$$

where ρ is the mass density; $\boldsymbol{u}$ is the displacement vector; λ and μ are the Lamé constants; $\nabla = (\partial/\partial x, \partial/\partial y, \partial/\partial z)$ is the differential operator. The first term on the right-hand side of Eq. (2-1) corresponds to the longitudinal wave and the second term to the transverse wave. The Lamé constants are related to Young's modulus E and Poisson's ratio ν as follows:

$$\lambda = \frac{\nu E}{(1+\nu)(1-2\nu)}, \tag{2-2}$$

$$\mu = \frac{E}{2(1+\nu)}. \tag{2-3}$$

When the frequency of the displacement field of a wave is ω, the Eq. (2-1) can be written as

$$\omega^2 \boldsymbol{u} = \rho^{-1}\{[\lambda + 2\mu]\nabla(\nabla \cdot \boldsymbol{u}) - \nabla \times [\mu \nabla \times \boldsymbol{u}]\}. \tag{2-4}$$

Rayleigh waves are a type of wave that propagate along a surface. In a half-infinite homogeneous elastic medium, the wave speed v_R of Rayleigh waves is constant. It can be considered as a coupling of two inhomogeneous plane waves (P and SV waves). The Rayleigh wave velocity v_R is related to the longitudinal wave velocity v_P and the transverse wave velocity v_S by the following equation: [40,128,186-188]

$$0 = (2 - \frac{v_R^2}{v_S^2})^2 - 4\sqrt{1 - \frac{v_R^2}{v_P^2}}\sqrt{1 - \frac{v_R^2}{v_S^2}}, \tag{2-5}$$

when $k = v_R^2/v_S^2$ and $n = v_S^2/v_P^2$, Eq. (2-5) can be rewritten as the Rayleigh equation: [186,187,189]

$$k^3 - 8k^2 + (24 - 16n)k - 16(1-n) = 0. \tag{2-6}$$

The parameter k is obtained by solving Eq. (2-6). The v_R is obtained when the v_S and the v_P (or Poisson's ratio ν) of the substrate material are known. The equation has real roots in the interval $0 < k < 1$, meaning that the v_R is less than the v_S. In half-infinite homogeneous elastic media, the v_R is independent of frequency, i.e., the Rayleigh wave is a non-dispersive wave. If there is a cover layer of other media on the surface of the medium, the Rayleigh wave is a dispersive wave.

2.1.2 **Periodic condition and Bloch's theorem**

Seismic metamaterials are usually periodic structures, similar to crystals in solid state physics. The position vector of a unit cell of a periodic structure is $\{\boldsymbol{a}_1, \boldsymbol{a}_{2,}\boldsymbol{a}_3\}$. The linear overlap of these three basis vectors can form a periodic structure in space. The lattice vector is

$$\boldsymbol{R}_n = n_1\boldsymbol{a}_1 + n_2\boldsymbol{a}_2 + n_3\boldsymbol{a}_3 \tag{2-7}$$

where n_1, n_2 and n_3 are integers, all physical parameters $f(\boldsymbol{r})$ at any $\boldsymbol{r}$ also have periodicity: [184,185]

$$f(\boldsymbol{r}+\boldsymbol{R}_n)=f(\boldsymbol{r}). \tag{2-8}$$

The Fourier expansion of $f(\boldsymbol{r})$ is:

$$f(\boldsymbol{r})=\sum_h F(\boldsymbol{G_h})\mathrm{e}^{\mathrm{i}\boldsymbol{G}_h r}, \tag{2-9}$$

where $\boldsymbol{G}_h$ is the inverse lattice vector in the inverse space (Fourier space). $\boldsymbol{G}_h$ is related to $\boldsymbol{R}_n$ as follows:

$$\boldsymbol{G}_h\cdot\boldsymbol{R}_n=2m\pi, \tag{2-10}$$

where m is an integer. In the inverse space, the inverted lattice vector satisfies

$$\boldsymbol{G}_h=h_1\boldsymbol{b}_1+h_2\boldsymbol{b}_2+h_3\boldsymbol{b}_3, \tag{2-11}$$

where

$$\boldsymbol{b}_1=2\pi\frac{\boldsymbol{a}_2\times\boldsymbol{a}_3}{\boldsymbol{a}_1\cdot(\boldsymbol{a}_2\times\boldsymbol{a}_3)}, \tag{2-12}$$

$$\boldsymbol{b}_2=2\pi\frac{\boldsymbol{a}_3\times\boldsymbol{a}_1}{\boldsymbol{a}_1\cdot(\boldsymbol{a}_2\times\boldsymbol{a}_3)}, \tag{2-13}$$

$$\boldsymbol{b}_3=2\pi\frac{\boldsymbol{a}_1\times\boldsymbol{a}_2}{\boldsymbol{a}_1\cdot(\boldsymbol{a}_2\times\boldsymbol{a}_3)}. \tag{2-14}$$

When an elastic wave propagates in a periodic structure, the solution of the elastic wave equation can be written in the following form: [93]

$$\boldsymbol{u}(\boldsymbol{r},t)=\mathrm{e}^{-\mathrm{i}\omega t}\sum\boldsymbol{u}_{\boldsymbol{k}+\boldsymbol{G}_h}\mathrm{e}^{\mathrm{i}(\boldsymbol{k}+\boldsymbol{G}_h)\cdot\boldsymbol{r}}=\mathrm{e}^{\mathrm{i}(\boldsymbol{k}\cdot\boldsymbol{r}-\omega t)}\boldsymbol{u}_{\boldsymbol{k}}(\boldsymbol{r}), \tag{2-15}$$

where $\boldsymbol{k}$ is the wave vector; ω is the eigenfrequency. From Eq. (2-15), the result remains the same when the wave vector $\boldsymbol{k}$ adds an inverted lattice vector $\boldsymbol{G}_h$. Thus, the results within the whole periodic structure can be represented by calculating the eigenvalues corresponding to the wave vectors $\boldsymbol{k}$ in a small region. This small region is called the first Brillouin zone. The first Brillouin zone can be obtained as an irreducible Brillouin zone due to its symmetry.

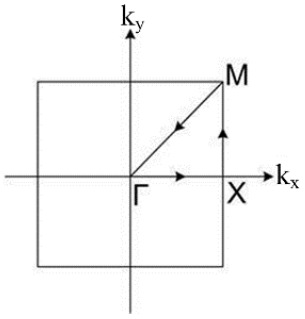

Figure 2-1 The first irreducible Brillouin zone

The first irreducible Brillouin zone for the seismic metamaterials with square lattice: M = (π/a, π/a), Γ = (0, 0), X = (π/a, 0)

For example, the irreducible Brillouin zone of a periodic structure with a two-dimensional square lattice arrangement and a high symmetry internal structure is the $\Gamma - X - M - \Gamma$ as shown in Fig. 2-1. [190] The band structure is obtained by scanning the wave vector $\boldsymbol{k}$ within this irreducible Brillouin zone.

2.1.3 Real band structures

The "band structure" in this thesis refers specifically to the "real band structure". In the band structure, the frequency range where the band exists is called the pass band, and the frequency range where the band does not exist is called the bandgap (or stop band). [191] In the frequency range of the pass band, the wave is able to pass through the periodic structure. Waves cannot pass through the periodic structure in the bandgap. [46,49,112,139,140] For example, in the band structure shown in Fig. 2-2(a), [160] there are dispersion curves (or bands) in the frequency range less than 8 Hz, so there are pass bands. In the range of 8-14 Hz there is no band, so it is a bandgap.

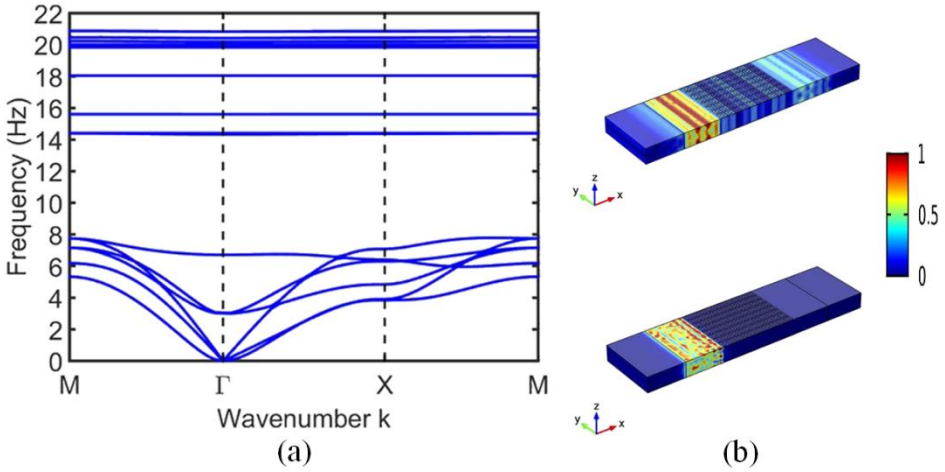

Figure 2-2 The band structure and the transmission[132]

(a) The band structure. (b) The transmission of waves in seismic metamaterials

The transmission spectrum of the elastic wave in the seismic metamaterial can clearly demonstrate the bandgap characteristics. As shown in Fig. 2-2(b), the source is

located on the left side of the seismic metamaterial, and the Perfectly Matched Layer (PML) is used to absorb the elastic waves on both sides to prevent wave reflection. The upper panel in Fig. 2-2(b) shows that the waves can easily reach the right side through the seismic metamaterial in the pass band. The lower panel in Fig. 2-2(b) shows that in the bandgap, the waves have difficulty passing through the seismic metamaterial. Therefore, based on the bandgap characteristics, the seismic metamaterial can isolate the seismic waves to protect the building.

2.2 The finite element method

2.2.1 **Solid mechanics module**

This subsection presents the calculations of the band structure and transmission spectrum of seismic metamaterials by the solid mechanics module of COMSOL Multiphysics 5.4. As shown in Fig. 2-3(a), [135] the seismic metamaterial generally consists of a deep substrate (gray part) and an artificial structure (blue part). The periodic boundary conditions are set on the four surfaces perpendicular to the ground according to Bloch's theorem. A fixed constraint is applied at the bottom of the substrate. It is worth noting that the results of low-frequency surface waves in band structures are more convergent when the thickness of the substrate is deep enough.

Substituting the displacement condition of the periodic boundary [112,139,154,155]

$$\boldsymbol{u}(\boldsymbol{r}+\mathbf{a}) = \mathrm{e}^{\mathrm{i}(\boldsymbol{k}\cdot\mathbf{a})}\boldsymbol{u}(\boldsymbol{r}), \tag{2-16}$$

into Eq. (2-1), the standard eigenvalue equation is obtained:

$$(\mathbf{K}+\omega^2\mathbf{M})\boldsymbol{u} = 0, \tag{2-17}$$

where $\mathbf{a}$ is the lattice constant vector; $\mathbf{K}$ and $\mathbf{M}$ are the stiffness and mass matrices of the unit cell, respectively. Solving the Eq. (2-17) and scanning the wave vector $\boldsymbol{k}$ in the irreducible Brillouin zone, the dispersion relation between the frequency ω and the wave vector $\boldsymbol{k}$ can be obtained, i.e., the band structure as shown in Fig. 2-3(b). Due to the deep substrate, it is easy to find sound cones in the band structure, i.e., outside the dark gray region in Fig. 2-3(b). It is often found in the study of Rayleigh wave metamaterials. [157,192,193] In all bands within the sound cone, the vibration modes of the seismic metamaterial are shown in Fig. 2-3(c), all of which are surface wave modes, i.e., the vibration exists only near the surface. So, the bandgaps for surface waves can

be found within the sound cone. Outside the sound cone, there are complex vibration modes, including bulk wave modes and pseudo-surface wave modes. [163,164,194]

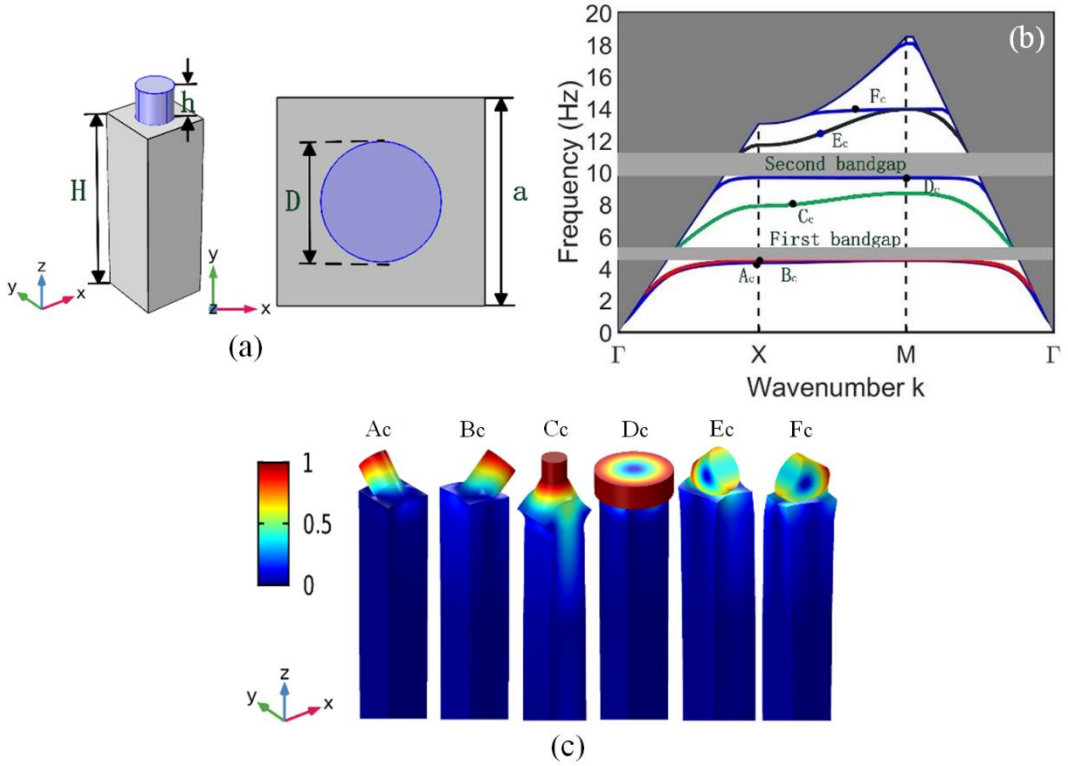

Figure 2-3 Calculation of band structure of the seismic metamaterial [135]

(a) The unit cell of the seismic metamaterial. (b) The band structure of the seismic metamaterials. (c) The vibration modes of the seismic metamaterials

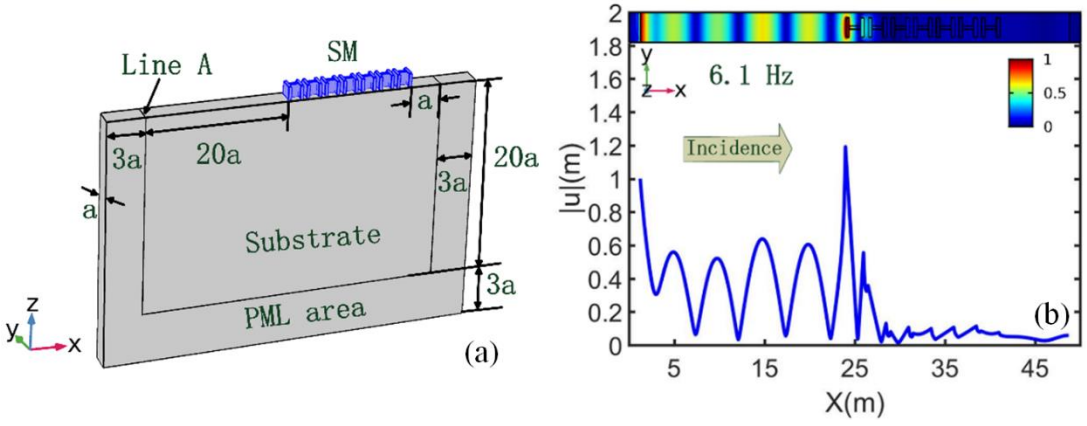

Figure 2-4 Calculation of transmission of surface waves [135]

(a) Schematic model of the finite system used for calculating transmission. (b) The transmission of surface waves in the seismic metamaterial

The calculation of the transmission spectrum of seismic Rayleigh waves is a

common method to study the bandgap properties of seismic metamaterials. [32,37,38,53,131,133] Figure 2-4(a) shows the seismic metamaterial with periodicity along the y direction. The bottom and sides of the substrate are set as PML to prevent the reflection of waves from the boundary. The wave source is excited farther to the left of the seismic metamaterial. As shown in Fig. 2-4(b), the attenuation effect of Rayleigh waves can be observed directly from the top of the seismic metamaterial. In this thesis, a part of the right surface of the seismic metamaterial is often selected point to obtain the amplitude (or acceleration) A_1, and then the amplitude (or acceleration) A_0 of the same point is measured after moving out the artificial structure. The transmission spectrum of the seismic metamaterial is [39,52,114,143,195-198]

$$T_s = 20\log_{10}(A_1/A_0). \tag{2-18}$$

2.2.2 **Multibody dynamics module**

This subsection presents the calculations of the band structure of seismic metamaterials with hinge joints by the multibody dynamics module of COMSOL Multiphysics 5.4.

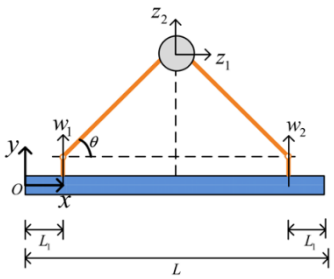

Figure 2-5 The unit cell of the beam metamaterial[199]

As shown in Fig. 2-5, a unit cell of an inertially amplified metamaterial is shown. According to Bloch's theorem, periodic boundary conditions are added to the boundary on both sides of the unit cell. It is worth noting that both boundary similarity and pointwise constraint are utilized to achieve the periodic boundary condition in the multibody dynamics module. Similarly, the band structure can be obtained by scanning the wave vector.

2.2.3 **Partial differential equation module**

This subsection presents the calculations of the complex band structure of seismic metamaterials by the partial differential equation (PDE) module of COMSOL Multiphysics 5.4.

The governing equation in the PDE module is [112,171,200,201]

$$\Lambda^2 e_a \boldsymbol{u} - \Lambda d_a \boldsymbol{u} + \nabla \cdot (-c\nabla \boldsymbol{u} - \alpha \boldsymbol{u} + \gamma) + \beta \cdot \nabla \boldsymbol{u} + b\boldsymbol{u} = f, \tag{2-19}$$

where Λ, e_a, d_a, c, α, γ, β, b and f are the eigenvalues, mass coefficients, damping or mass coefficients, diffusion coefficients, conservative flux convection coefficients, convection coefficients, conservative flux source term, absorption coefficients and source terms, respectively.

For seismic metamaterials, the non-zero coefficients in Eq. (2-19) are the mass coefficient e_a, the diffusion coefficient c, the conservative flux convection coefficients α, the conservative flux source term β, and the absorption coefficients b. They are

$$e_a = \begin{pmatrix} -(\lambda + 2\mu) & 0 \\ 0 & -\mu \end{pmatrix}, \tag{2-20}$$

$$c = \begin{pmatrix} \begin{bmatrix} (\lambda + 2\mu) & 0 \\ 0 & \mu \end{bmatrix} & \begin{bmatrix} 0 & \lambda \\ \mu & 0 \end{bmatrix} \\ \begin{bmatrix} 0 & \mu \\ \lambda & 0 \end{bmatrix} & \begin{bmatrix} \mu & 0 \\ 0 & (\lambda + 2\mu) \end{bmatrix} \end{pmatrix}, \tag{2-21}$$

$$\alpha = \begin{pmatrix} \begin{bmatrix} (\lambda + 2\mu)\Lambda \\ 0 \end{bmatrix} & \begin{bmatrix} 0 \\ \mu\Lambda \end{bmatrix} \\ \begin{bmatrix} 0 \\ \mu\Lambda \end{bmatrix} & \begin{bmatrix} \mu\Lambda \\ 0 \end{bmatrix} \end{pmatrix}, \tag{2-22}$$

$$\beta = \begin{pmatrix} \begin{bmatrix} -(\lambda + 2\mu)\Lambda \\ 0 \end{bmatrix} & \begin{bmatrix} 0 \\ -\lambda\Lambda \end{bmatrix} \\ \begin{bmatrix} 0 \\ -\lambda\Lambda \end{bmatrix} & \begin{bmatrix} -\lambda\Lambda \\ 0 \end{bmatrix} \end{pmatrix}, \tag{2-23}$$

$$b = \begin{pmatrix} -\rho\omega^2 & 0 \\ 0 & -\rho\omega^2 \end{pmatrix}. \tag{2-24}$$

2.3 Transfer matrix method

2.3.1 **Dispersion relations of Rayleigh waves**

Figure 2-6 shows a layered model which consists of a homogeneous isotropic layer

of thickness h overlying a homogeneous half space. For the two-layered structure, the dispersion relation of the Rayleigh wave can be calculated using the transfer matrix method. [189,202]

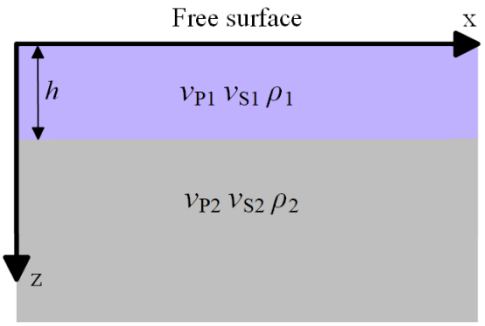

Figure 2-6 Layered media structure

In the transfer matrix method, five scalars are passed from the bottom layer to the surface layer, which are x_1, x_2, x_3, x_4 and x_5: [189,202]

$$x_1 = 1 + \Upsilon_{P2}\Upsilon_{S2} \tag{2-25}$$

$$x_2 = \Upsilon_2 + \Upsilon_{P2}\Upsilon_{S2} \tag{2-26}$$

$$x_3 = \mathrm{i}\Upsilon_{S2}g_2 \tag{2-27}$$

$$x_4 = -\mathrm{i}\Upsilon_{S2}g_2 \tag{2-28}$$

$$x_5 = -\Upsilon_2{}^2 - \Upsilon_{P2}\Upsilon_{S2} \tag{2-29}$$

where $\Upsilon_2 = v_R^2/(2v_{S2})^2$, $\Upsilon_{P2} = \sqrt{-1 + v_R^2/v_{P2}^2}$, $\Upsilon_{S2} = \sqrt{-1 + v_R^2/v_{S2}^2}$ and $g_2 = 1 - \Upsilon_2$; where v_{S2} and v_{P2} are the transverse and longitudinal wave velocities of the bottom medium, respectively. When these five scalars are transferred from bottom medium to surface layer, they change sequentially as follows:

$$\begin{cases} x_1 = x_1/l \\ x_5 = lx_5 \end{cases}, \tag{2-30}$$

where $l = \rho_2 v_{S2}^2/\rho_1 v_{S1}^2$,

$$\begin{cases} p_1 = -\Upsilon_1 x_1 + (1 + \Upsilon_1)x_2 + x_5 \\ p_2 = x_1 - 2x_2 - x_5 \\ p_3 = g_1 x_3 \\ p_4 = -g_1 x_4 \\ p_5 = -\Upsilon_1^2 x_1 + 2\Upsilon_1 x_2 + x_3 \end{cases}, \tag{2-31}$$

where $\Upsilon_1 = v_R^2/(2v_{S1})^2$ and $g_1 = 1 - \Upsilon_1$,

$$\begin{cases} q_1 = abp_2 + cdp_5 - adp_3 - bcp_4 \\ q_2 = adsp_2 - bcp_5 + abp_3 - cdsp_5 \\ q_3 = bcrp_2 - adp_5 - cdrp_3 + abp_4 \\ q_4 = cdrsp_2 + abp_5 + bcrp_3 + adsp_4 \end{cases}, \tag{2-32}$$

where $a = \cos(hk\Upsilon_{P1})$, $b = \cos(hk\Upsilon_{S1})$, $c = \sin(hk\Upsilon_{P1})/\Upsilon_{P1}$, $d = \sin(hk\Upsilon_{S1})/\Upsilon_{S1}$, $r = \Upsilon_{P1}^2$ and $s = \Upsilon_{s1}^2$; where $k = \omega/v_R$ is the is the number of waves in the Rayleigh wave on the free surface,

$$x_5 = -q_1\Upsilon_1{}^2 + q_4 - 2p_1\Upsilon_1. \tag{2-33}$$

When $x_5 = 0$, the dispersion equation is obtained. [189,202] The relationship between Rayleigh wave velocity and frequency in a two-layered structure can be obtained by solving this dispersion equation.

2.3.2 **Dispersion relations of flexural waves**

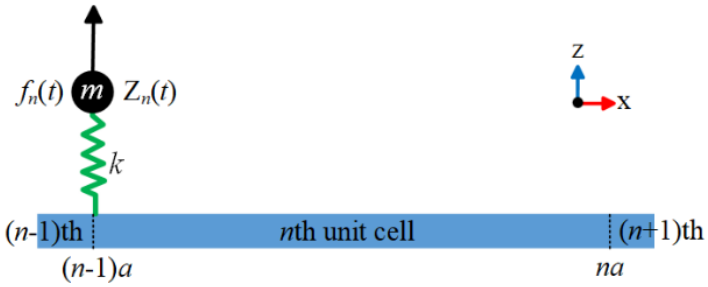

Figure 2-7 Metamaterial beam consisting of a beam and spring oscillators

As shown in Fig. 2-7, in the metamaterial beam consisting of a beam and spring oscillators, the governing equation for the flexural waves in the beam is [203,204]

$$EI\frac{\partial^4 z(x,t)}{\partial x^4} + \rho A\frac{\partial^2 z(x,t)}{\partial t^2} = 0, \tag{2-34}$$

where E, I, ρ and A are Young's modulus, section moment of inertia, density and section area of the beam, respectively. $z(x,t)$ is the out-plane displacement of the beam. The physical quantities of the beam can be expressed in the following forms [203]

$$z(x,t) = \left(Ae^{-i\lambda x} + Be^{i\lambda x} + Ce^{-\lambda x} + De^{\lambda x}\right)e^{-i\omega t}, \tag{2-35}$$

$$\theta(x,t) = \frac{\partial z(x,t)}{\partial x}, \tag{2-36}$$

$$M(x,t) = EI\frac{\partial^2 z(x,t)}{\partial x^2}, \tag{2-37}$$

$$Q(x,t) = -EI\frac{\partial^3 z(x,t)}{\partial x^3}, \tag{2-38}$$

where A, B, C and D are complex coefficients; $\lambda = \sqrt[4]{\rho A\omega^2/EI}$ with $\omega = 2\pi f$ being the circular frequency is the flexural wavenumber; and θ, M and Q are the slope, bending moment and shear force, respectively. The out-plane displacement of the nth unit cell is [203]

$$z_n(x_1,t) = \left(A_n e^{-i\lambda x_1} + B_n e^{i\lambda x_1} + C_n e^{-\lambda x_1} + D_n e^{\lambda x_1}\right)e^{-i\omega t}, \tag{2-39}$$

where $x_1 = x - (n-1)a$ and $(n-1)a \le x \le na$. So, from the left side to the right side of the nth unit cell, we obtain the transfer matrix in this field by following:

$$\mathbf{\Psi}_n(0,t) = \mathbf{H}_{1\alpha}[A_n B_n C_n D_n]^T e^{-i\omega t}, \tag{2-40}$$

$$\mathbf{\Psi}_n(a,t) = \mathbf{H}_{1\beta}[A_n B_n C_n D_n]^T e^{-i\omega t}, \tag{2-41}$$

where $\mathbf{\Psi}(x,t) = [z(x,t)\ \theta(x,t)\ M(x,t)\ Q(x,t)]^T$ is the state vector; and $\left[A_{n,1}\ B_{n,1}\ C_{n,1}\ D_{n,1}\right]^T$ is the coefficient vector. Substituting Eq. (2-41) into Eq. (2-40), we obtain

$$\mathbf{\Psi}_n(a,t) = \mathbf{H}_{1\beta}\mathbf{H}_{1\alpha}^{-1}\mathbf{\Psi}_n(0,t) \triangleq \mathbf{H}_1\mathbf{\Psi}_n(0,t), \tag{2-42}$$

where $\mathbf{H}_1$ is the transfer matrix. As for the nth spring oscillators on the beam, the dynamic equilibrium equation is

$$f_n(t) + m\frac{\partial^2 Z_n(t)}{\partial t^2} = 0, \tag{2-43}$$

where $f_n(t)$ is the force of the nth spring and $f_n(t) = F_n e^{-i\omega t}$, $Z_n(t)$ is the displacement of the nth mass; where $Z_n(t) = V_n e^{-i\omega t}$ and $\partial^2 Z_n(t)/\partial t^2 = -\omega^2 V_n e^{-i\omega t}$; where V_n is the amplitude of the nth mass. Due to the Hooke's Law, we obtain

$$f_n(t) = k[Z_n(t) - z_n(0,t)], \tag{2-44}$$

where k is the spring stiffness. Substituting Eq. (2-44) into Eq. (2-43), we obtain

$$Z_n(t) = \frac{k}{k - m\omega^2}z_n(0,t), \tag{2-45}$$

$$f_n(t) = \frac{m\omega^2 k}{k - m\omega^2} z_n(0,t), \tag{2-46}$$

Due to the continuities at the interface between $(n-1)$th and nth unit cells, we obtain

$$z_{n-1}(a,t) = z_n(0,t), \tag{2-47A}$$

$$\theta_{n-1}(a,t) = \theta_n(0,t), \tag{2-47B}$$

$$M_{n-1}(a,t) = M_n(0,t), \tag{2-47C}$$

$$Q_{n-1}(a,t) = Q_n(0,t) - f_n(t). \tag{2-47D}$$

Substituting Eq. (2-46) into Eq. (2-47), we obtain

$$\mathbf{\Psi}_{n-1}(a,t) = \mathbf{H}_2 \mathbf{\Psi}_n(0,t). \tag{2-48}$$

Substituting Eqs. (2-42) and (2-48), the transfer equation of the flexural waves from the right interface of the $(n-1)$th unit cell to the right interface of the nth unit cell is obtain

$$\mathbf{\Psi}_n(a,t) = \mathbf{T}_{unit} \mathbf{\Psi}_{n-1}(a,t), \tag{2-49}$$

where $\mathbf{T}_{unit} = \mathbf{H}_1 \mathbf{H}_2^{-1}$ is the transfer matrix. Considering the Bloch-Floquet theory, there is

$$\mathbf{\Psi}_n(a,t) = \mathrm{e}^{\mathrm{i}\lambda a} \mathbf{\Psi}_{n-1}(a,t). \tag{2-50}$$

Substituting Eq. (2-50) into Eq. (2-49), we obtain

$$\left| \mathbf{T}_{unit} - \mathrm{e}^{\mathrm{i}\lambda a} \mathbf{I}_{\mathrm{A}} \right| = 0, \tag{2-51}$$

where $\mathbf{I}_{\mathrm{A}}$ is an identity matrix. By solving the eigenvalue equation, the band structure can be obtained.

2.4 Conclusions

In this chapter, the important methods used in this thesis are presented. This chapter first introduces the basic theory in the study of seismic metamaterials, including elastic wave equation, Rayleigh waves, periodic condition, Bloch's theorem and band structure. Then the finite element method study based on the solid mechanics module, multibody dynamics module and PDE module of the software COMSOL Multiphysics is presented. Finally, the analytical calculations of dispersion relation of Rayleigh

waves in a two-layered half-space, and dispersion relation of flexural waves in a metamaterial beam are given based on the transfer matrix method.

Chapter 3 Inverse-dispersion properties and wide bandgap design of three-component seismic metamaterials

A subwavelength SM consisting of three-component seismic metamaterial plate (SMP) on a half-space is proposed to attenuate ultra-low frequency seismic surface waves in a variety of geological situations in this chapter. We first review the surface wave transmission experiments of the two-component SM composed of two-component SMP on a half-space.[160] This is the experimental basis of the three-component SMs in this paper. Then we calculate the band structures of the one-dimensional (1D) and two-dimensional (2D) SMs, check their attenuation ability to Rayleigh waves, and specifically discuss the propagation of Rayleigh waves in the SM in the range of the ultra-low frequency BG. The subwavelength SM does not need bedrock or fixed boundary condition to clamp the bottom of the pillars in metamaterials. This explains that the ultra-low frequency BG and the wide BG can be more universally implemented theoretically than the previous works.[50,168] The subwavelength SM uses traditional building materials, making it a very practical design.

For the one-dimensional periodic SM, the reduced wave vector from 0 to π/a (a is the period of the SM) is used to obtain the eigenvalues.[163] For the two-dimensional periodic SM, which is highly symmetrical, the wave vector along $\Gamma - X$ direction [190] is used to calculate the band structures.

3.1 Two-component seismic metamaterials

3.1.1 Model and experimental setup

Figure 3-1(a) shows that the unit cell of the two-component SMP consists of a steel core wrapped with a flexible foam plate. Figure 3-1(b) shows the unit cell of the two-component SM consisting of the two-component SMP and half space. The band structures of two-component SMP and SM are calculated along $\Gamma - X$ direction, which are shown in Figs. 3-1(c) and 3-1(d) respectively.

In the experiment, the sample comprising foam-steel composite is zoomed in the upper right corner of Fig. 3-1(e). The size of the steel core is 140 mm x 40 mm x 40 mm, and the thickness of the flexible foam plate is 5 mm. The size of the glass box is 1.2 m x 0.5 m x 0.5 m, and the material of the substrate is sand. In order to reduce the

reflection of the elastic wave by the glass wall, pebbles are placed around the wall.[152]

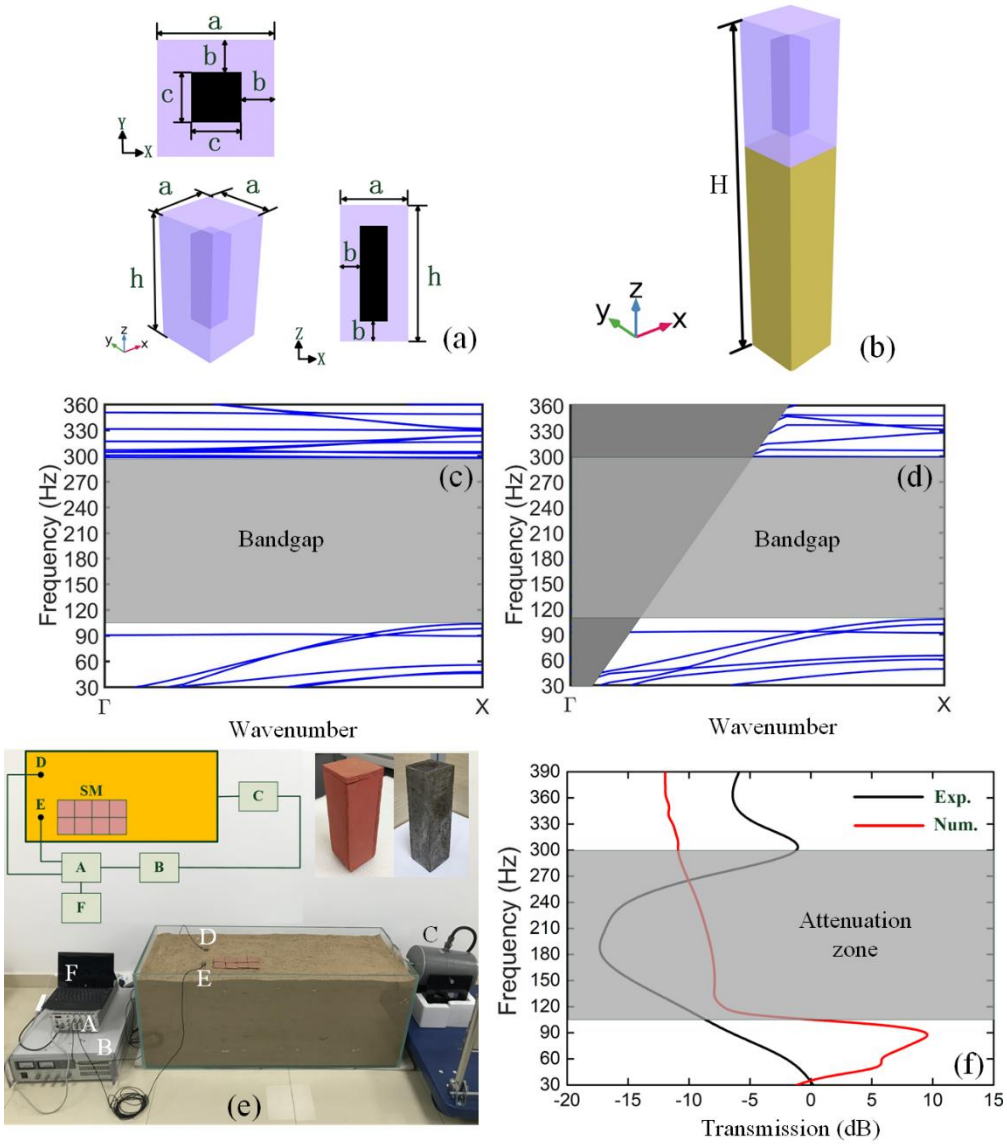

Figure 3-1 The two-component seismic metamaterial

(a) The unit cell of two-component seismic metamaterial plate (SMP). (b) The unit cell of two-component seismic metamaterial (SM) consisting of two-component SMP and half space. Band structures of (c) two-component SMP and (d) two-component SM. (e) Experimental setup and the design of unit cell. (f) Experimental and numerical transmission spectrums for supercell of eight unit cells (four rows) of two-component SM

The schematic of the setup is in the upper left corner of Fig. 3-1(e). Among them, A is the signal generator and signal collector, B is a signal amplifier, C is a vibration

exciter, D and E are two accelerometers, and F is a PC. The details of the experimental instruments used in the present work are consistent with this reference [160]. A thick layer of high-damping plastic foam is placed under the glass box to achieve a similar effect to the vibration isolation platform.

The accelerations are carried out by using two accelerometers placed on two symmetrical points (labels D and E in Fig. 3-1(e)). One (label D) is placed in the free zone where there is no interaction between the SM and the seismic wave, and the other ((label E)) is located behind the SM. Suppose that the acceleration values of points D and E are A_D and A_E, respectively. Then the attenuation spectrum of SM on the surface wave is $20 \times \log_{10}(A_E/A_D)$ shown in Fig. 3-1(f).

Table 3-1 Material parameters of the unit cell

Material	Density (kg/m^3)	Young's modulus (Pa)	Poisson's ratio
Rubber	1300	1.2×10^5	0.47
Concrete	2500	4×10^{10}	0.3
Steel	7784	2.07×10^{11}	0.3
foamed plate	1053	1.6×10^5	0.39
Soil	1800	2×10^7	0.3

3.1.2 **Results and Discussion**

In order to verify if the new design of SMs can attenuate seismic surface waves, we have performed lab-scale experiment for a supercell of eight unit cells (four rows) of two-component SM to measure the transmission spectrum. The geometric parameters are: a = 5 cm, b = 1 cm, c = 4 cm, h = 15 cm and H = 20a. The material parameters [160] are illustrated in Table 3-1. All parameters used in the simulation are consistent with those in the lab-scale experiment.

Comparing the two band structures, we can find that when the SMP is placed on the half space, the original band is basically unchanged, but the sound cone (dark gray area in Fig. 3-1(d)) is added due to the existence of the half space. So, we can not only keep the BG of the SMP itself in Fig. 3-1(d). It is found that the addition of the substrate

does not affect the original band structure of SMP. That is to say, the band structure of the SM composed of the two-component SMP and a half space is almost equal to band structure of the two-component SMP plus the sound cone. The sound cone, the boundary of which is formed by the slowest bulk wave propagating in the substrate, can be used to immediately identify real propagating surface waves, bulk modes as well as leaky surface modes and spurious PML modes. Therefore, the wide BG of the SMP itself is preserved. At 110 Hz – 300 Hz, we can verify that the SM can attenuate the surface waves well by lab-scale experiments and simulated calculations of the supercell, which corresponds to the BG in Fig. 3-1(d). The geometric model, material parameters, and position of the supercell and substrate used in the simulation calculations are consistent with the lab-scale experiments. In addition, the boundary formed by the glass wall is replaced by a low reflection boundary to reduce reflected waves.

This lab-scale experiment demonstrates that the two-component SM can attenuate the surface waves in the frequency range of the BG well, but this SM is powerless for the lower frequency surface waves. However, our previous work [160] shows that this SM composed of SMP and substrate can strongly attenuate surface waves in numerical simulation and lab-scale experiments. In addition, this kind of SM only needs to be laid on the base layer, which reduces costs and simplifies construction. The functional shortcomings of the two-component SM prompt us to further improve the SM to possess the above-mentioned advantages and also attenuate surface waves at ultra-low frequencies. In the following, the effect of SM composed of the three-component SMP and substrate is systematically investigated on the attenuation of surface waves in the ultra-low frequency range.

3.2 Three-component seismic metamaterials

From the above simulations and lab-scale experiment of the SM consisting of the two-component SMP and half space, it can be seen that the band structure of the SM is almost equal to the band structure of the SMP plus the sound cone. This SM can effectively attenuate the seismic surface waves to protect the buildings. Next, we will use FEM calculations to discuss the band structure and attenuation effect of the subwavelength SM consisting of the three-component SMP and a half space on the seismic surface waves. The ultra-low frequency BG of the subwavelength SM is discussed under the one-dimensional (1D) and two-dimensional (2D) periodic models.

3.2.1 **Models of 1D seismic metamaterials**

Figure 3-2(a) shows a unit cell of 1D three-component SMP, which is set to a Bloch periodic boundary condition in the x direction and a free boundary condition in the z direction. Figure 3-2(b) shows a unit cell of the 1D SM consists of a unit cell of 1D three-component SMP and a half space. It is set to the Bloch period boundary condition in the x direction, the upper boundary is a free boundary, and the lower boundary is a fixed boundary. The geometric parameters are: a = 1.5 m, $a_1 = 0.6a$, $a_2 = 0.5a$, $H = 20a$. The material parameters are illustrated in Table 3-1. [132]

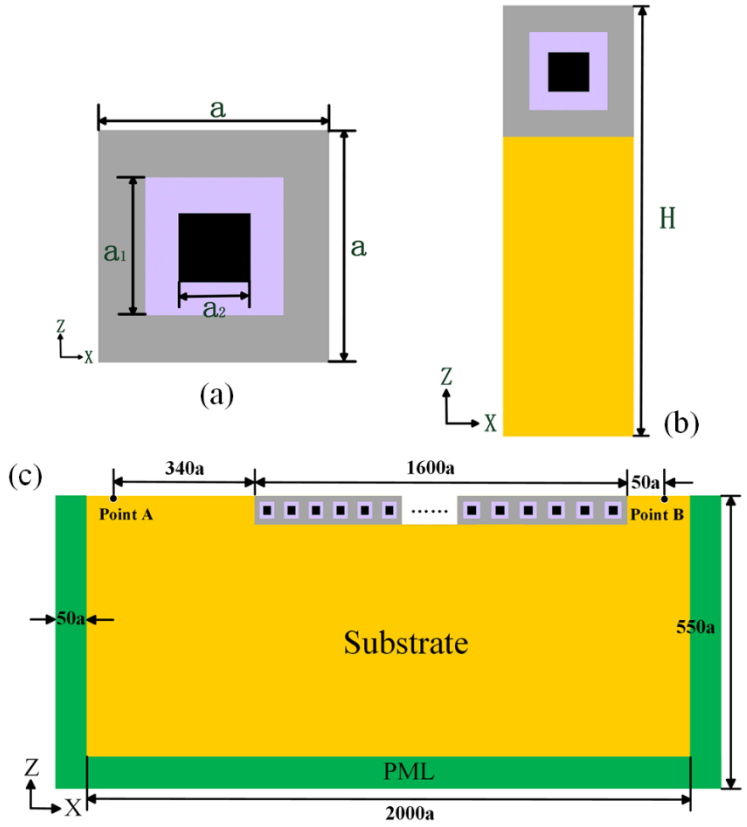

Figure 3-2 The three-component seismic metamaterial

(a) The unit cell of the 1D three-component SMP. (b) The unit cell of 1D SM. (c) A schematic diagram of a system for calculating transmission spectra

Figure 3-2(c) shows a schematic diagram of the system used to calculate the transmission spectrum. Since the ultra-low frequency BG of the subwavelength SM is mainly studied and discussed in this paper, and the wavelength of the seismic surface wave is large in the range of the ultra-low frequency BG, the values of the geometric parameters involved here are all large, especially the depth (500a) of the substrate, the

distance (340a) from the source (point A in Fig. 3-2(c)) to the SM and the number (1600) of the unit cells of the subwavelength SM. Point B (Fig. 3-2(c)) is the signal collection point. Suppose that the acceleration at point B located after the SMP is A_1, and the acceleration at point B without the SMP is A_0. Then the transmission function is defined as $20 \times \log_{10}(A_1/A_0)$. To prevent unwanted reflections, we add a perfectly matched layer (PML) with a thickness of 50a which is about the same as the incoming wavelength at low frequencies, as shown in Fig. 3-2(c). Among them, the PML scaling factor and the PML scaling curvature parameter are 1. Some works [198,205] also use low reflection boundaries to achieve similar results.

3.2.2 **Results and Discussion**

For a 1D three-component SMP based on local resonance, a BG can easily occur. As shown in Fig. 3-3(a), a narrow BG appears in the range of 10.0 – 14.0 Hz. Even if the unit cells in Fig. 3-2(a) are periodically arranged in two dimensions, the BG is very narrow. [197] It is conceivable that such a narrow BG cannot meet our needs. However, when we place this SMP on a half space (i.e. the SM), we are surprised to find two wide BGs (0 – 9.0 Hz and 9.4 – 22.0 Hz) for surface waves. And one of them is an ultra-low frequency BG. By comparing the band structures in Figs. 3-3(a) and 3-3(b), we can easily find that the band structure of the 1D SM consisting of the 1D three-component SMP and a half space is almost equal to the band structure of the 1D three-component SMP plus the sound cone. Therefore, the ultra-low frequency BG and the wide BG are generated shown in Fig. 3-3(b). It is worth noting that there are still bulk modes in the frequency range of the ultra-low frequency BG without any surface mode. This result proves that this work is completely different from the previous ones [50,168] which do not have modes in the ultra-low frequency BG. In Fig. 3-3(d), the effective density, shear modulus and bulk modulus of the SMP are obtained by using numerical methods. [200] We can see that the BG of SMP is due to the appearance of its negative effective mass density.

Through the transmission spectrum of the subwavelength SM, we can also see the existence of these two wide BGs. In the range of the ultra-low frequency BG, we see that the seismic surface waves are well attenuated in the range of 0.5 – 9.0 Hz. However, for the seismic surface waves close to zero frequency, the attenuation effect needs to be improved. Because the number of unit cells in the proposed subwavelength SM is

infinite because of the periodic boundary condition when calculating the band structure, while the number of the unit cells in the subwavelength SM is finite (1600 unit cells) when calculating the transmission spectrum. Therefore, we hypothesize that the number of the unit cells of the SM and the lower limit of the attenuation zone in the transmission spectrum are closely related.

To discover the relationship between the number of the unit cells of the subwavelength SM and the lower limit of the attenuation zone in the transmission spectrum, we simulate and plot the displacements of surface waves of the system varying with the frequency by calculating the transmission spectrum. As shown in Fig. 3-4(a), we use the subwavelength SM of 1600 unit cells placed from 0 m to 2400 m for calculation. The transmission distance of the Rayleigh waves increases in the subwavelength SM exponentially with the decrease of frequencies from 5.0 Hz to around 0.5 Hz. It is found that in a higher frequency range between 3 Hz to 5 Hz, we can also attenuate seismic surface waves with very few seismic metamaterial units.

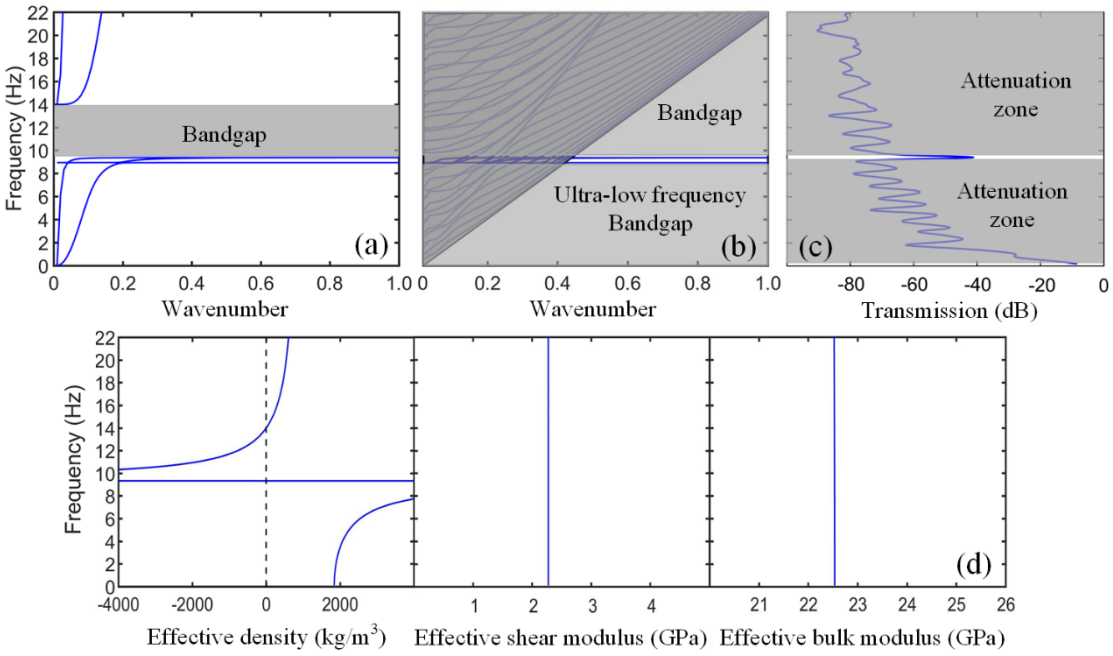

Figure 3-3 The results of three-component seismic metamaterial

(a) Band structure of the 1D three-component SMP. (b) Band structure of the 1D SM. (c) Transmission spectrum of the system in Fig. 3-2(c). (d) The effective parameters of the 1D three-component SMP

When the frequency is less than 0.5 Hz, Rayleigh waves pass through the 1600 unit cells of subwavelength SM. We can speculate that if the number of unit cells in the subwavelength SM increases, the propagation of the lower-frequency Rayleigh waves can be attenuated. Physically speaking, this subwavelength SM is a novel SM with the ultra-low frequency BG. For practical applications, it is also very convenient to select the number of unit cells according to the frequency range that we consider. We have studied the transmission of Rayleigh waves in the subwavelength SM at 2.2 Hz to demonstrate the mechanism of the subwavelength SM. As shown in Fig. 3-4(c), when the Rayleigh waves enter the subwavelength SM, they are deflected at a certain angle and converted into bulk waves.

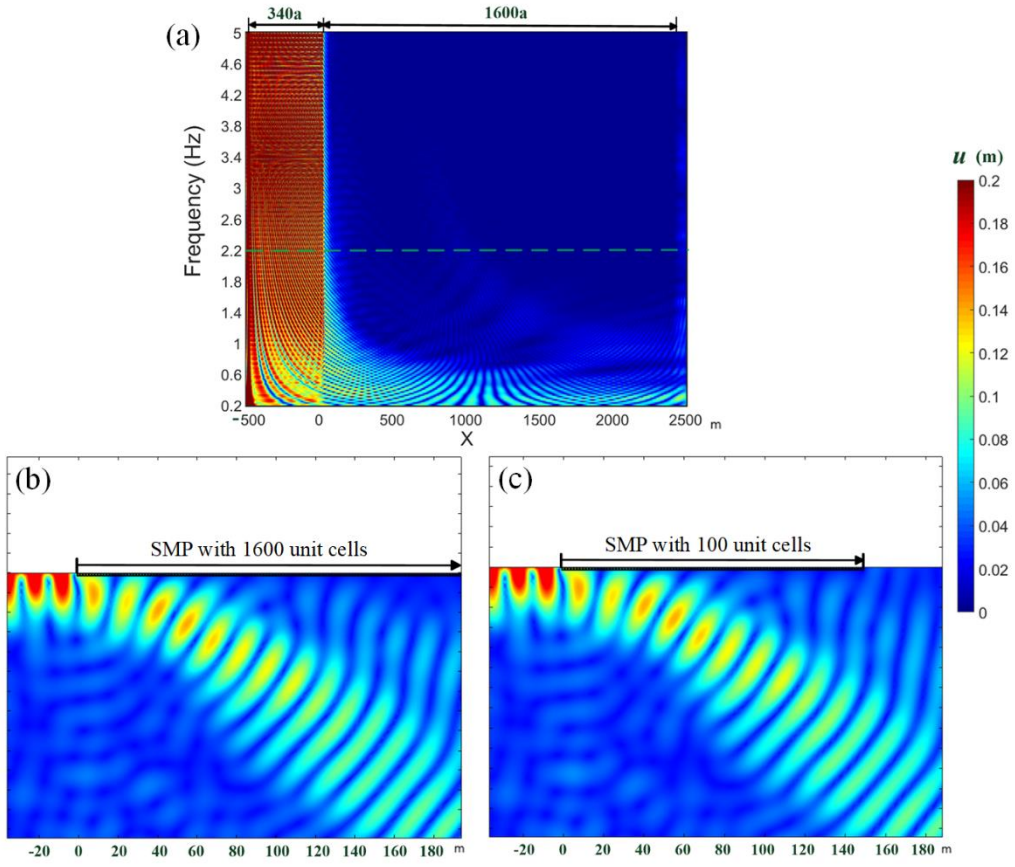

Figure 3-4 Transmission of the surface waves in the seismic metamaterial

(a) The displacements of surface waves of the system varying with the frequency by calculating the transmission spectrum. (b) The propagation of Rayleigh waves in subwavelength SM with 1600 unit cells at 2.2 Hz. (c) The propagation of Rayleigh waves in subwavelength SM with 100 unit cells at 2.2 Hz. The colors indicate the total displacement (u) ranging from 0 to maximum

As shown in Figs 3-4(c) and 3-4(d), the waves at the left end of the SM are Rayleigh waves. The energy of Rayleigh waves is mainly concentrated in the depth of two wavelengths below the surface. The Rayleigh waves are converted into bulk waves in the SM, because there is no surface wave mode in the SM at the frequency of the ultra-low frequency BG, but the bulk wave modes exist.

To explain this phenomenon, we draw a dotted line with the frequency of 2.2 Hz on the band structure of the subwavelength SM shown in Fig. 3-4(b). At 2.2 Hz, there is no surface wave mode in the subwavelength SM. However, there are a large number of bulk wave modes outside the sound cone. That is to say, at 2.2 Hz, only the bulk wave modes exist in the subwavelength SM. Therefore, Rayleigh waves will be deflected and converted into bulk waves as shown in Fig. 3-4(c). Results show that the seismic Rayleigh waves are transformed into bulk waves after entering the three-component seismic metamaterial. It is caused by the Inverse-dispersion effect of the two-layer layered medium composed of the half-space substrate and the three-component seismic metamaterial (see details of Inverse-dispersion effect in appendix of this chapter).

We also use the subwavelength SM of 100 unit cells placed from 0 m to 150 m with for the calculation of the transmission spectrum in Fig. 3-4(d). We find that the deflection of Rayleigh waves is almost the same as the subwavelength SM with 1600 unit cells. When the Rayleigh waves propagate to the position of $X = 60$ m (presumably at the position of the 40th unit cell), most of the energy has turned from the surface to the bulk below the surface. This also shows that when the number of the unit cells of the subwavelength SM is sufficient, the transmission distance and deflection angle of the Rayleigh waves in the subwavelength SM are constant at the same frequency. In practical applications, the method of arranging the number of the unit cells of the subwavelength SM according to the specified frequency range is effective.

In order to investigate the influence of the material parameters of the substrate on the ultra-low frequency BG, we consider the effect of the Young's modulus and mass density of the substrate on the upper frequency bounds of the ultra-low frequency BG for the 1D subwavelength SM. The material parameters of the substrate are selected within the actual soil parameters [134]. However, when the Young's modulus of the substrate increases from 10 MPa to 100 MPa, and the mass density of the substrate is

between 1600 kg/m^3 and 2200 kg/m^3, the upper boundary (9.0 Hz) of the ultra-low frequency BG does not change. In this range of the Young's modulus and the mass density, the upper boundary of the ultra-low frequency BG is determined by the band of the local resonance of the SMP, which is invariable. From the effect of the Young's modulus and mass density of the substrate on the upper frequency bounds of the ultra-low frequency BG for the 1D SM, we can find that the subwavelength SM is suitable for different soils in different regions. This also shows that the subwavelength SM is universal.

The values for material parameters of the substrate are swept and are intended for qualitative comparison only [200]. Through the simulation calculation and discussion, we find this important universal equation: the band structure of the SM composed of the SMP and a half space is almost identical to band structure of the SMP plus the sound cone. It is noteworthy that this conclusion is incorrect when the heavy core of the unit cell of the SMP connects the substrate. [34,132]

The above 1D SWSM can be modelled as a two-layered medium as shown in Fig. 3-5(a). The green part is the effective medium of the SMP. Its upper boundary is the free boundary, and the thickness is a = 1.5 m. In the low frequency region (0 - 5 Hz) away from local resonance, as shown in Fig. 3-3(d), the effective mass density of the SMP is about 2000 kg/m^3. And the effective Young's modulus E_e = 27.12 GPa, Poisson's ratio υ_e = 0.3. The substrate shown in Fig. 3-5(a) is a half-space of soil.

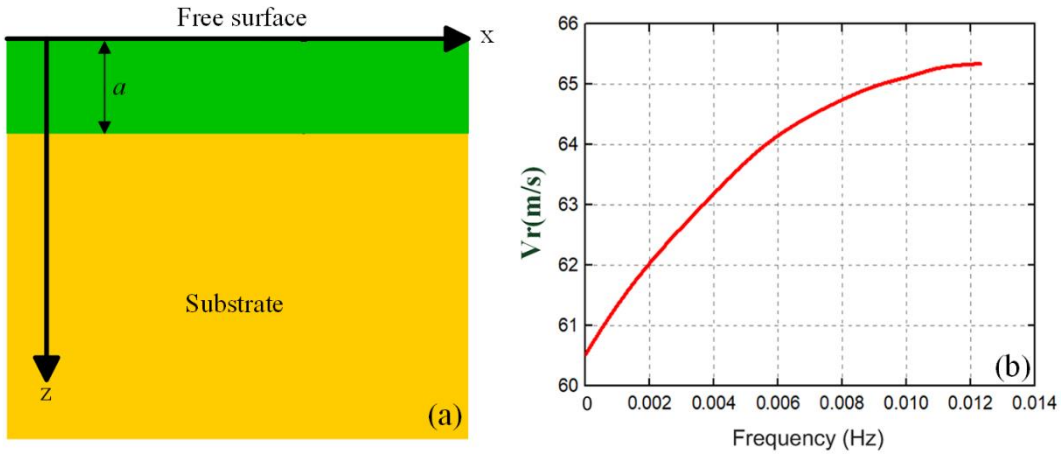

Figure 3-5 Effective two-layered medium

(a) Effective two-layered medium of 1D SM, (b) Rayleigh waves dispersion curve of the two-

layered media

For the layered medium shown in Fig. 3-5(a), the dispersion curve of the Rayleigh wave can be calculated by the fast scalar method. [202] As shown in Fig. 3-5(b), the dispersion curve of the layered medium only supports a single waveguide mode and exhibits a typical inverse dispersion. [206] The wave velocity of Rayleigh waves increases with the frequency increasing in the two-layered medium in the range of 0 - 0.0125 Hz. And there is a cut-off frequency (0.0125 Hz). It means that, when the frequency is greater than the 0.0125 Hz, Rayleigh waves will not exist in the effective two-layered medium. This also verifies the correctness of the ultra-low frequency BG because 0.0125 Hz is close to zero.

3.2.3 Models of 2D seismic metamaterials

In order to verify that the above the subwavelength SM still has an ultra-low frequency BG in the three-dimensional space, we have studied the 2D SM as shown in Fig. 3-6(b). Similarly, we also calculate the band structure of the unit cell of the 2D three-component SMP shown in Fig. 3-6 (a).

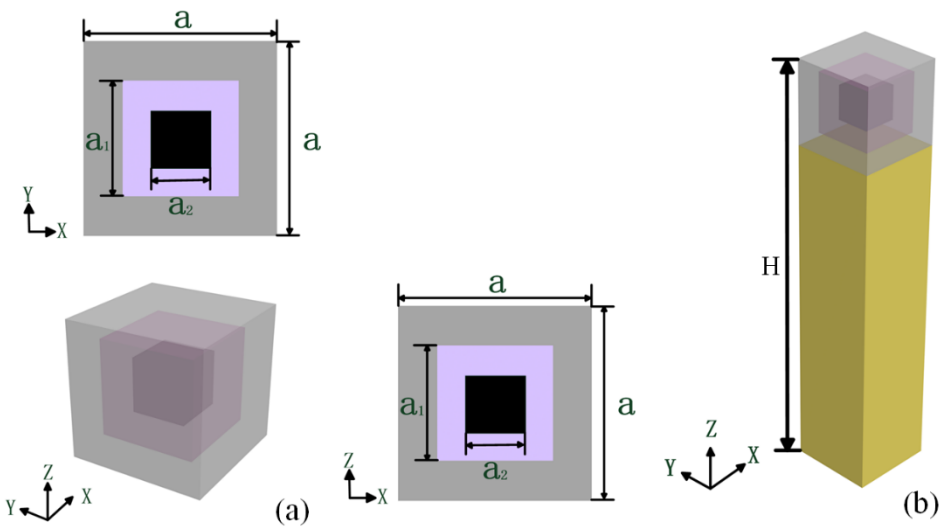

Figure 3-6 The 2D three-component seismic metamaterial

(a) The unit cell of the 2D three-component SMP. (b) The unit cell of 2D SM

The unit cell of the 2D SM consists of a unit cell of the 2D three-component SMP and a half space. The geometric parameters (a, a_1, a_2 and H) and the material parameters of the four materials (concrete, rubber, steel and soil) are consistent with those of the

1D SM. We set the Bloch period boundary conditions on the four vertical boundaries of the 2D SMP; and the upper and lower boundaries are free. The Bloch period boundary condition is set on the four vertical boundaries of the 2D SM; the lower boundary is set as the fixed boundary condition, and the upper boundary is set as the free boundary condition. The system used for transmission spectrum calculation is similar to Fig. 3-2(c), so it is not illustrated here.[135]

3.2.4 **Results and Discussion**

Metamaterials based on the local resonance is a subject of debate and discussion. Although they can obtain BGs at low frequencies, the width of the BGs needs to be expanded.[96] As shown in Fig. 3-7(a), the BG of the 2D three-component SMP is very narrow and only exists around 10.0 – 12.0 Hz. Even if the unit cells of such three-component SMP are three-dimensionally periodically arranged, the width of the BG is also narrow. [147] However, the 2D SM has two wide BG for surface waves, and one of them is an ultra-low BG. By comparing the band structures in Figs. 3-7(a) and (b), we can easily find that the band structure of the subwavelength SM consisting of the 2D three-component SMP and a half space is almost equal to the band structure of the 2D three-component SMP plus the sound cone. This is also the reason for the wide ultra-low BG.

We calculate the transmission spectrums of Rayleigh waves in the 1D and 2D SMs (along ΓX direction) with 100 unit cells at 0.5 – 5.0 Hz which is within the ultra-low frequency BG. The attenuation effect of the two kinds of subwavelength SM is almost the same, and the 2D SM is slightly better than the 1D SM at low frequencies (0.5 – 4.0 Hz). This shows that the 2D SM can also attenuate ultra-low frequency surface waves in the three-dimensional space.

As shown in Fig. 3-8, by comparing the propagations of Rayleigh waves in the 1D and 2D SMs (xz section diagram) with 100 unit cells at 4.0 Hz, the Rayleigh waves in the 2D SM also convert from surface waves to bulk waves, and the deflection angle of the Rayleigh wave is almost the same as that of the 1D SM. This shows that the 2D SM can attenuate surface waves in the frequency range of its ultra-low frequency BG to protect the target building. Its mechanism is consistent with that of the 1D SM.

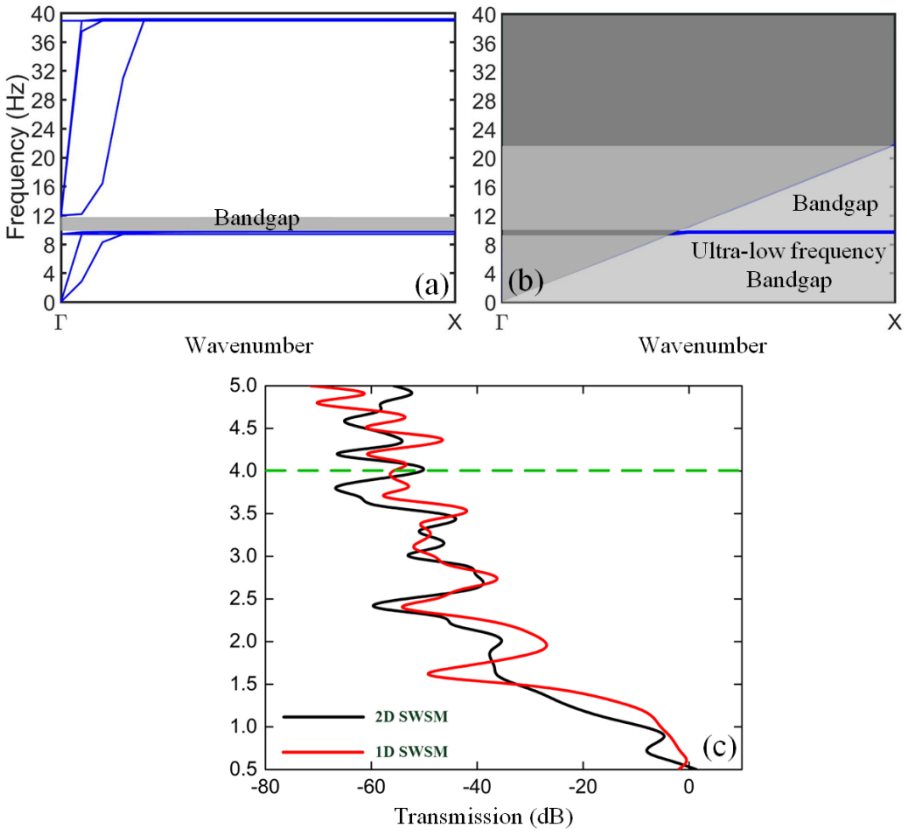

Figure 3-7 Transmission of the surface waves

(a) Band structure of the 2D three-component SMP. (b) Band structure of the 2D SM. (c) Transmission spectrums of 1D and 2D subwavelength SMs (SWSMs) with 100 unit cells in the frequency range of 0.5 Hz - 5.0 Hz

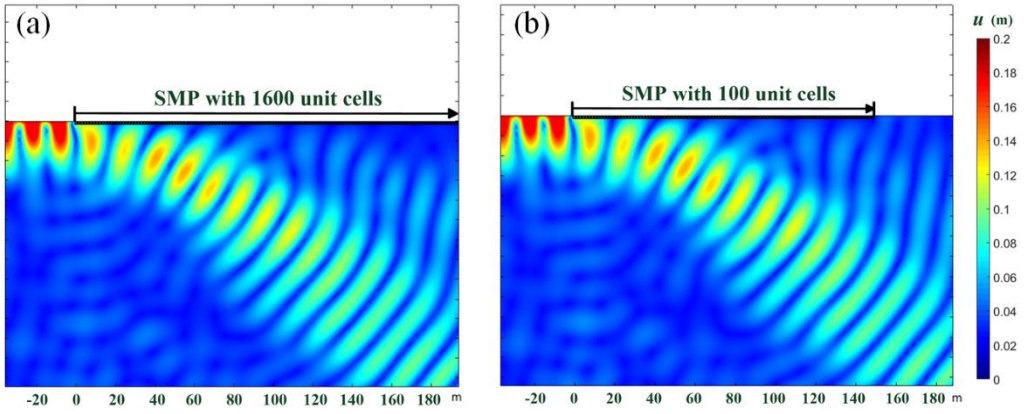

Figure 3-8 Propagations of the Rayleigh waves

The propagations of Rayleigh waves in (a) 1D SM and (b) 2D SM (*xz* section diagram) with 100 unit cells at 4.0 Hz. The colors indicate the total displacement (u) ranging from 0 to maximum

3.3 Conclusion

In summary, through the lab-scale experiments and numerical simulation of the SM consisting of the two-component SMP and a half space, we demonstrate this new design methodology to create SMs to attenuate seismic surface waves. In addition, lab-scale experiments are also the important basis for the application of three-component subwavelength SM. Then we propose a three-component subwavelength SM consisting of the three-component SMP and a half space. By investigating the influence of the material parameters of the substrate on the 1D SM, we find that the band structure of the SM composed of the SMP and a half space is almost equal to the band structure of the SMP plus the sound cone. By analyzing the propagation of Rayleigh waves in the 1D and 2D SMs in the frequency range of the ultra-low frequency BG, we find that Rayleigh waves are deflected at a certain angle and converted into bulk waves. When the number of the unit cells of the subwavelength SM is sufficient, the transmission distance and deflection angle of the Rayleigh waves in the subwavelength SM are constant at the same frequency. In summary, the SM consisting of only one layer of the SMP buried underground and substrate has an ultra-low frequency BG and can convert Rayleigh waves into bulk waves in the frequency range of the BG. Meanwhile, the simple design of this SM is conducive to its manufacturing and practical application and the efficiency of the SM to attenuate Rayleigh waves is also very significant. All the phenomena demonstrate that the subwavelength SM can attenuate surface waves in the frequency range of its ultra-low frequency BG to protect the target building. This subwavelength SM is expected to protect large nuclear power plants, ancient buildings and metropolises from damage by seismic waves. This paper not only demonstrates the application prospects of subwavelength SM, but also provides design guidance for surface wave researchers.

3.4 Appendix: Inverse-dispersion effect and a simple example

Figure 3-9 shows a layered model which consists of a homogeneous isotropic layer of thickness h overlying a homogeneous half space. For the two-layered structure, the dispersion relation of the Rayleigh wave can be calculated using the transfer matrix method.[189,207] When the material parameters of the two-layered structure are identical, i.e., the homogeneous half-space structure, the velocity of the Rayleigh waves is

constant.[151] When the material parameters of the two-layered structure are different, situations are complicated, and only two representative cases are discussed here: I ($Vs_2 > Vr_2 > Vs_1 > Vr_1$) and II ($Vs_1 > Vr_1 > Vs_2 > Vr_2$). The assumed parameters are shown in Tables 3-2 and 3-3. Where Vp_1, Vs_1, Vr_1, and ρ_1 (Vp_2, Vs_2, Vr_2, and ρ_2) are the longitudinal wave velocity, shear wave velocity, Rayleigh wave velocity and density of the cover layer (substrate), respectively. The thickness of the cover layer is fixed at h = 6 m.

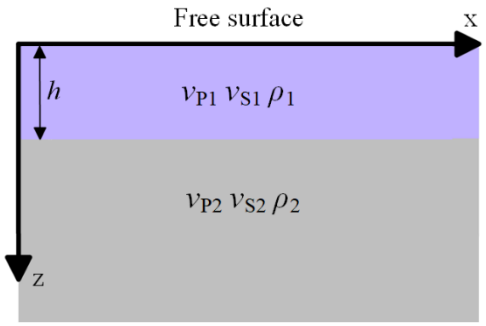

Figure 3-9 Layered media structure

Table 3-2 The assumed material parameters when $V_{S2} > V_{R2} > V_{S1} > V_{R1}$

	V_P	V_S	V_R	ρ
Cover layer	1500	1000	893.1	1800
Substrate	2000	1400	1229.0	2300

Table 3-3 The assumed material parameters when $V_{S1} > V_{R1} > V_{S2} > V_{R2}$

	V_P	V_S	V_R	ρ
Cover layer	2000	1400	1229.0	2300
Substrate	1000	800	636.7	1800

For case I, the dispersion curves of the Rayleigh waves of this two-layered layer structure are shown in Figure 3-10(a). This is a very common dispersion curves in earth science. [208] There are multiple guided waves in the layered structure, and the maximum Rayleigh wave velocity (phase velocity) is equal to the shear wave velocity of the substrate (Vs_2), and the minimum Rayleigh wave velocity (phase velocity) is equal to the Rayleigh wave velocity of the cover layer (Vr_1). Vs_2 and Vr_1 are underlined in Table 3-2. For any one of these guided waves, the velocity of the Rayleigh waves gradually

decreases with increasing frequency and finally becomes flat.

For case II, the dispersion curves of the Rayleigh waves of this two-layered layer structure are shown in Fig. 3-10(b). We can find the inverse-dispersion effect, [209] that is, the wave velocity (phase velocity) of the Rayleigh waves increases with increasing frequency. This layered structure has only a unique Rayleigh guided wave: the minimum Rayleigh wave velocity (phase velocity) is equal to the Rayleigh wave velocity of the substrate (Vr_2), and the maximum Rayleigh wave velocity (phase velocity) is equal to the shear wave velocity of the substrate (Vs_2). Also, Vr_2 and Vs_2 are underlined in Table 3-3. And the most interesting thing is that this Rayleigh guided wave has a cutoff frequency. When the frequency is higher than this cutoff frequency, about 25 Hz as shown in Fig. 3-10(b), there is no Rayleigh wave in such two-layered structure.

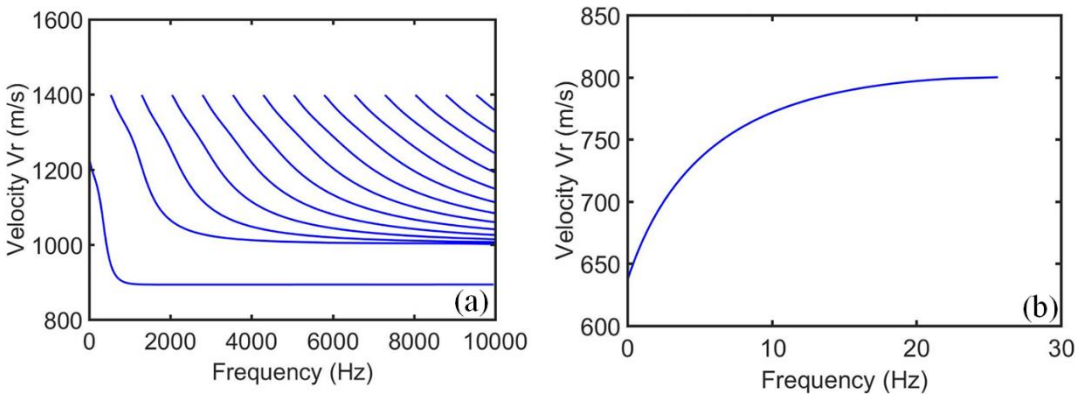

Figure 3-10 The dispersion curves of the Rayleigh waves

The dispersion curves of the Rayleigh waves of the two-layered layer structure when (a) $Vs_2>Vr_2>Vs_1>Vr_1$ and (b) $Vs_1>Vr_1>Vs_2>Vr_2$

Figure 3-11(a) shows the unit cell of the T-shaped SM (TSM) composed of T-shaped steel and substrate, and the substrate is the soil. The boundaries identified by the red lines in the Fig. 3-11(a) are all set to the periodic boundary conditions. In this way, we connect the tops of all the pillars to form a simple layered structure: the T-shaped steel on substrate form a cover layer. The geometric parameters are: a = 1.5 m, $h = 6a$, $d = 0.2a$, $H = 500a$ and $D = 0.25a$. The bottom boundaries identified by the green lines are all set to the fixed boundary conditions.

Figure 3-11(b) shows the complex band structures of the surface modes of the

TSM. Because the wavelength of Rayleigh waves at the ultra-low frequency (below 0.1 Hz) is too difficult to calculate, only the complex band structures in the range of 0.1 to 8.0 Hz is drawn. *This is the first characteristic of the BG based on inverse-dispersion effect: there is no surface mode in the range of the BG.*

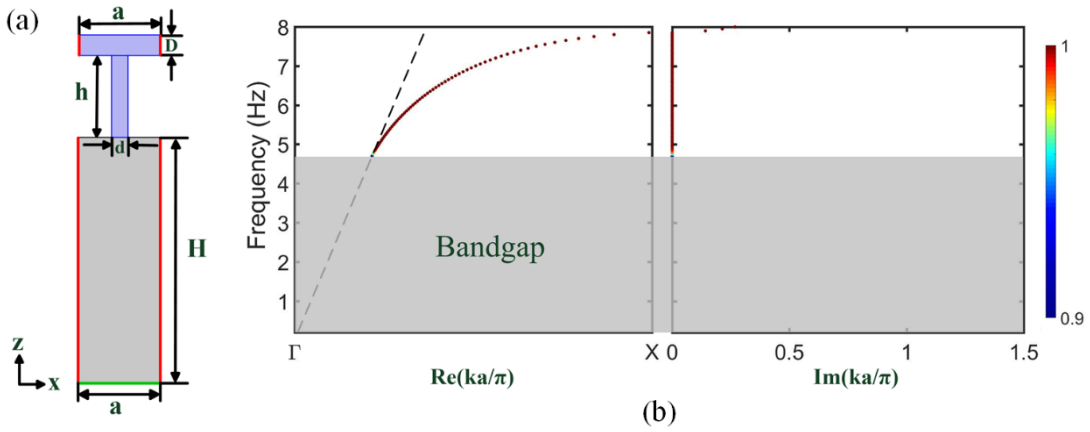

Figure 3-11 The T-shaped seismic metamaterial

(a) The unit cell and (b) complex band structure of the T-shaped seismic metamaterial

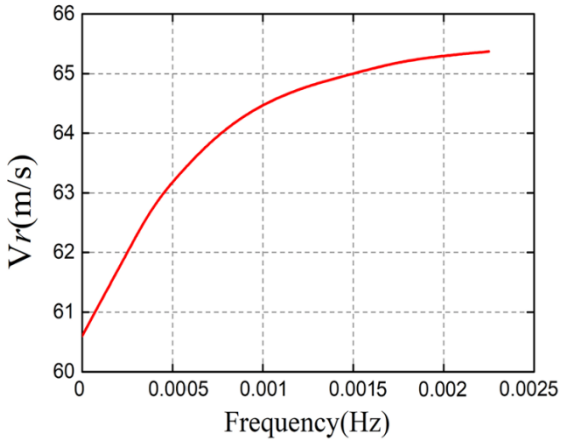

Figure 3-12 The dispersion curves of Rayleigh waves

The TSM can be roughly equivalent to a layered medium composed of two materials as shown in Fig. 3-9. Considering that the cover layer is a steel structure composed of pillars and a plate, we calculate the effective Young's modulus and effective density of this cover layer at a low frequency (0.1 Hz) through effective medium theory: Young's modulus E = 207 GPa, density ρ=4000 kg/m^3. Considering that the materials of the plates and pillar are all steel, the effective Poisson's ratio of this

cover layer is still 0.3. And the thickness of the cover layer is $h_1 = 6.25a$, i.e. the height of pillar h plus thickness of steel plate D. This layered medium has only a single guided wave mode and there is a cutoff frequency of about 0.0023 Hz in Fig. 3-12. In this layered medium, when the frequency is higher than 0.0023 Hz, there is no longer any Rayleigh wave. This is the reason for the BG shown in Fig. 3-11(b). This phenomenon has also been found in the SM with a similar structure.[52] *This is the second characteristic of the BG based on inverse-dispersion effect: SM can be equivalent to a two-layered medium, and it satisfies* $Vs_1 > Vr_1 > Vs_2 > Vr_2$.

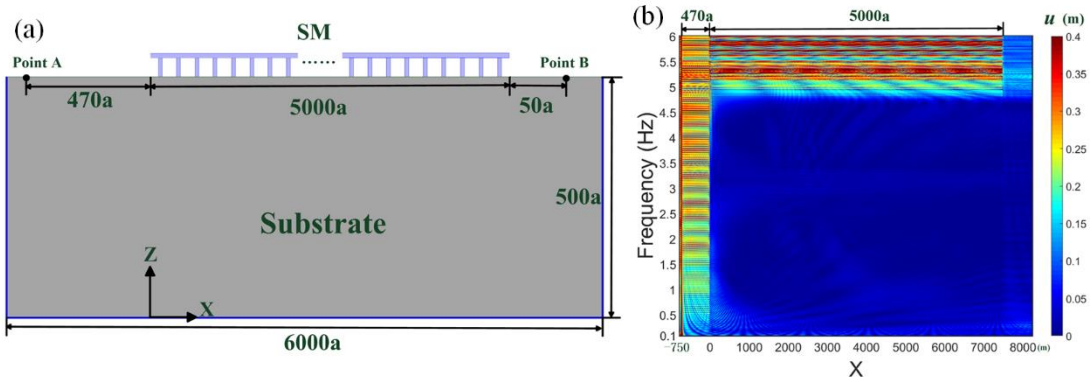

Figure 3-13 The transmission results

(a) A schematic diagram of the finite system for calculating transmission spectra. (b) Distribution of displacement amplitude of the finite system varying with the frequency

The frequency domain analysis of the TSM is conducted to verify the existence of the BG, according to the model of the finite system shown in Fig. 3-13(a). Because the ultra-low frequency Rayleigh waves has a longer wavelength, the parameters we set are larger when designing the finite system to ensure the accuracy of the simulation results. Here, the number of unit cells of the TSM is set to 5000, mainly for lower frequency Rayleigh waves, such as below 0.1 Hz. The problem of the number of unit cells of TSM will be discussed in detail later. As shown in Fig. 3-13(b), we plot the displacement of the surface of this finite system at different frequencies. The TSM is placed at $0 < X < 7500$ m. From Fig. 3-13(b), we can find that the TSM can attenuate Rayleigh waves well in the wide frequency range of 0.1 - 4.8 Hz.

In order to discuss the effect of the number of unit cells of the TSM on the attenuated Rayleigh waves, the attenuation of the Rayleigh waves by the TSM with 200

unit cells is calculated. For a slightly lower frequency, such as 1.3 Hz, the TSM with 200 unit cells can convert a portion of the Rayleigh waves into a bulk waves, but the rest of the Rayleigh wave also passes through the TSM in Fig. 3-14(a). Obviously, the attenuation effect of the TSM with 200 unit cells is limited. As shown in Fig. 3-14(b), the TSM with 5000 unit cells are used can well convert most of the Rayleigh waves into bulk waves. At a slightly higher frequency, such as 3.5 Hz in Fig. 3-14(c-d), the attenuation effect of the Rayleigh waves by the TSM of 200 and 5000 unit cells is almost the same. Rayleigh waves are almost converted into bulk waves by the TSMs. *This is the third characteristic of the BG based on inverse-dispersion effect: the SM with enough unit cells can convert most of surface waves to bulk waves.*

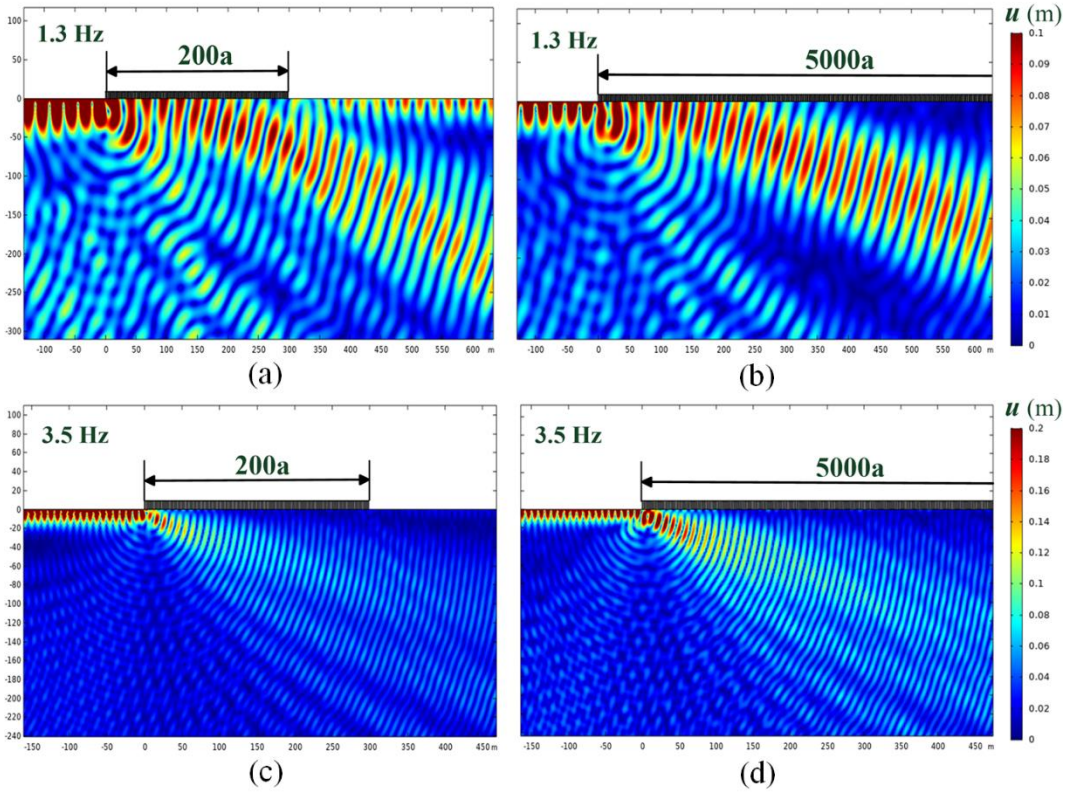

Figure 3-14 The propagations of the surface waves

Distribution of displacement amplitude at 1.3 Hz for TSM with (a) 200 and (b) 5000 unit cells and at 3.5 Hz for (c) 200 and (d) 5000 unit cells.

Chapter 4 Design of the inverted T-shaped seismic metamaterials and implementation of the ultra-wide first bandgap

The subwavelength SMs are usually composed of periodic pillar-like structure and substrate, which can be called the pillar-like SM (PSM). A major characteristic of the PSM is that it mainly attenuates the propagation of seismic surface waves, [35,133,135,136] especially in the low-frequency range of the first BG (FBG), and even if the PSM only has three rows.[133,135] The PSM is found because seismic surface waves in a part of the frequency range cannot pass through forest.[133] When the seismic waves interact with a forest, some frequencies are strongly attenuated due to the resonance of trees. When trees are considered as steel pillars or pillars with different shapes, the attenuation of surface waves in the SMs still exists, and better results can be obtained. So, I-shaped,[135] fractal structure [134] and Matrayoshka-like [137] PSMs are proposed to obtain a wider complete BG in the sound cone. However, the relative bandwidth of the FBG is currently too small to meet the needs of practical applications.

A one-dimensional inverted T-shaped SM (1D ITSM) composed of pillars and plates with ultra-wide FBG is proposed in this chapter. The ITSM is just a simple modification based on the PSM: a plate is added at the bottom of each pillar. The FBGs of the two different SMs are compared. The effects of the ITSM's geometric and material parameters on the FBG are discussed. The complex band structure of the ITSM for surface waves is calculated and compared with that of the PSM. The propagation properties of seismic surface waves in the ITSM are also given. Finally, we propose a kind of the two-dimensional (2D) ITSM with the ultra-wide FBG.

4.1 1D Inverted T-shaped seismic metamaterials

4.1.1 **Models**

In this section, the classical PSM and the proposed 1D ITSM are compared. As shown in Fig. 4-1, the PSM and the ITSM have the same steel pillar, i.e., $l_2 = l$, $w_2 = w$. But the bottom of every pillar in the ITSM is clamped by a steel plate marked as gray part in Fig. 4-1(b). The geometric and material parameters of the unit cells are given in Tables 4-1 and 4-2, respectively. In numerical simulation, the left and right boundaries of the substrate of the unit cell are set as Bloch periodic boundaries, and the bottom of

the substrate is set as a fixed boundary condition to avoid surface modes on the bottom.[137,194,198] It is worth noting that the calculation results will converge well at ultra-low frequency when the geometric parameter *H* is enough large. In this paper, the COMSOL Multiphysics is used to calculate the band structures and the propagation of Rayleigh waves in the SMs.

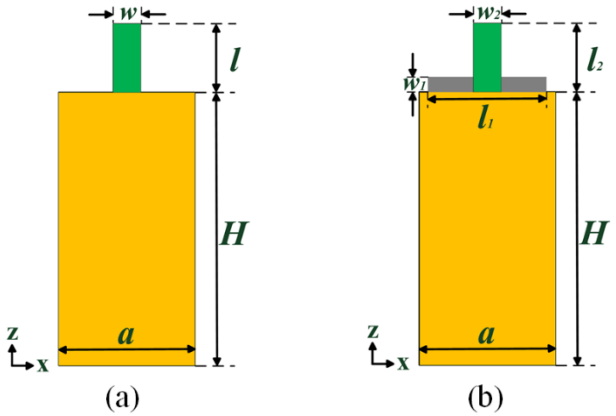

Figure 4-1 The unit cells of the seismic metamaterials

The unit cells of (a) the pillar-like seismic metamaterial and (b) the inverted T-shaped SM

Table 4-1 The geometric parameter of the SMs

a	H	l_1	w_1	$l_2(l)$	$w_2(w)$
1.5m	300a	0.95a	0.05a	1.4285a	0.07a

Table 4-2 The material parameters [34,152,160]

Material	Density (kg/m^3)	Young's modulus (Pa)	Poisson's ratio
Steel	7784	2.07×10^{11}	0.3
Soil	1800	2×10^{7}	0.3

4.1.2 **Classical band structures**

Figures 4-2 (a - b) show the classical band structures of the PSM and the ITSM, respectively. The classical band structures are calculated by using the Solid Mechanics module of COMSOL. The sound cones are clearly surrounded by the light gray areas. There are only surface waves inside the sound cone. Therefore, surface waves cannot

exist in the SMs in the frequency range where no band appears, i.e., the bandgap for surface waves. Moreover, the bandgaps at the lowest frequency, i.e., the FBGs, are marked by the dark gray areas in Figs. 4-2 (a - b). In this work, the frequency range of the FBG is from 0.72 Hz to 0.80 Hz for the PSM, and from 6.7 Hz to 17.2 Hz for the ITSM. Although the FBG of the PSM is very low, it is extremely narrow (relative bandwidth is about 0.1) and thus unsuitable for seismic shielding. In contrast, although the minimum value of the FBG of the ITSM is 6.7 Hz, its relative bandwidth can reach an astonishing value as 0.88. We believe that this way of abandoning the BG with ultra-low frequency in exchange for the ultra-wide BG is desirable in the practical application of SMs.

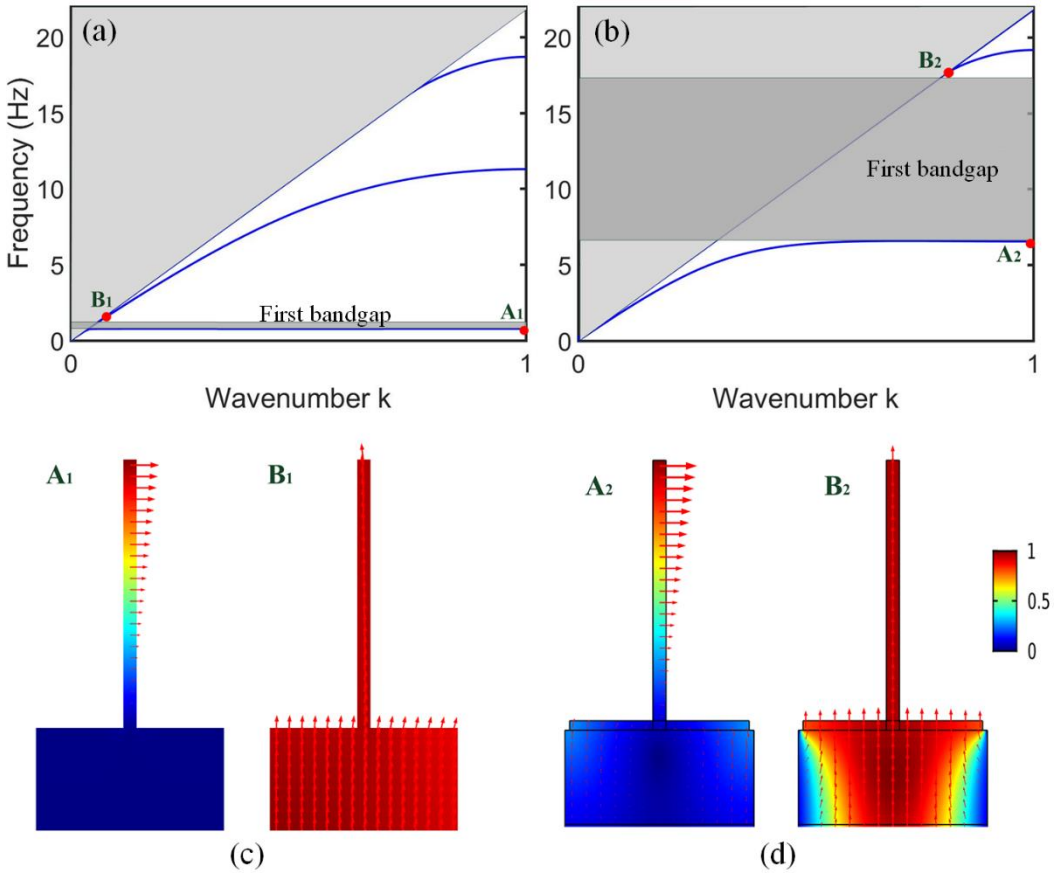

Figure 4-2 The band structures and vibration modes

The classical band structures of (a) the PSM and (b) the 1D ITSM, the vibration modes of (c) the PSM and (d) the 1D ITSM at the points marked the classical band structures.

The vibration modes of the PSM and the ITSM at marked points are illustrated in

Figs. 4-2 (c - d). The marked points A_1 and B_1 (A_2 and B_2) are the lower and upper boundaries of the FBG of the PSM (ITSM), respectively. The direction of the arrows represents the direction of the particle movement, and the color indicates the normalized total displacement. It is easy to find that the vibration modes of the lower, upper boundaries of the two FBGs (points A_1 and A_2, points B_1 and B_2) are similar. This indicates that the generation mechanism of these two FBGs is also similar. On the first bands of two SMs, i.e., at points A_1 and A_2, the maximum displacement appears on the top of the steel structure. On the second bands of two SMs, i.e., at points B_1 and B_2, the displacement is on the entire steel structure and on the surface of substrate. The energy is evenly distributed on the entire structure. The pillar or the inverted T-shaped structure (ITS) can be considered as a whole this time. This shows that the structure of the ITS leads to a qualitative leap of the FBG. It is worth noting that although the second bandgap in Fig. 4-2(a) is similar to the FBG in Fig. 4-2(b), these two bandgaps have different generation physical mechanisms, which have been identified by many experiments and numerical simulations.[135,137,155]

4.1.3 **Effects of geometric parameters**

After comparing the band structures of the PSM and the ITSM, it is obvious that the appearance of the plate at the bottom of the pillar makes a huge change in the frequency range and relative bandwidth of the FBG. In this section, the effects of geometric parameters of the plate on the FBG are calculated, when the pillar is unchanged. In addition, the effect of the height of the pillar on the FBG is calculated to obtain the optimal geometric parameters of the ITSM, when the total volume of the pillar (i.e., $l_2 \times w_2$) is constant.

Figures 4-3(a - b) show that the variation of geometric parameters of the plate with the position and relative bandwidth of the FBG. As shown in Fig. 4-3(a), when the length l_1 of the plate increases from 0.5a to 0.99a, the lower boundary of the FBG slowly increases from 4.4 Hz to 7.0 Hz, and the upper boundary increases rapidly from 5.7 Hz to 20.7 Hz. Therefore, the relative bandwidth of the FBG increases from 0.27 to 0.99. As shown in Fig. 4-3(b), when the width of the plate increases from 0.02a to 0.18a, the lower boundary of the FBG first grows slowly from 5.5 Hz to 6.7 Hz, and then slowly drops to 6.4 Hz. However, the upper boundary of the FBG increases rapidly from 9.0 Hz to 17.2 Hz, and then slowly decreases to 13.7 Hz. Therefore, the relative

bandwidth of the FBG increases rapidly from 0.47 to 0.88, and then slowly drops to 0.73.

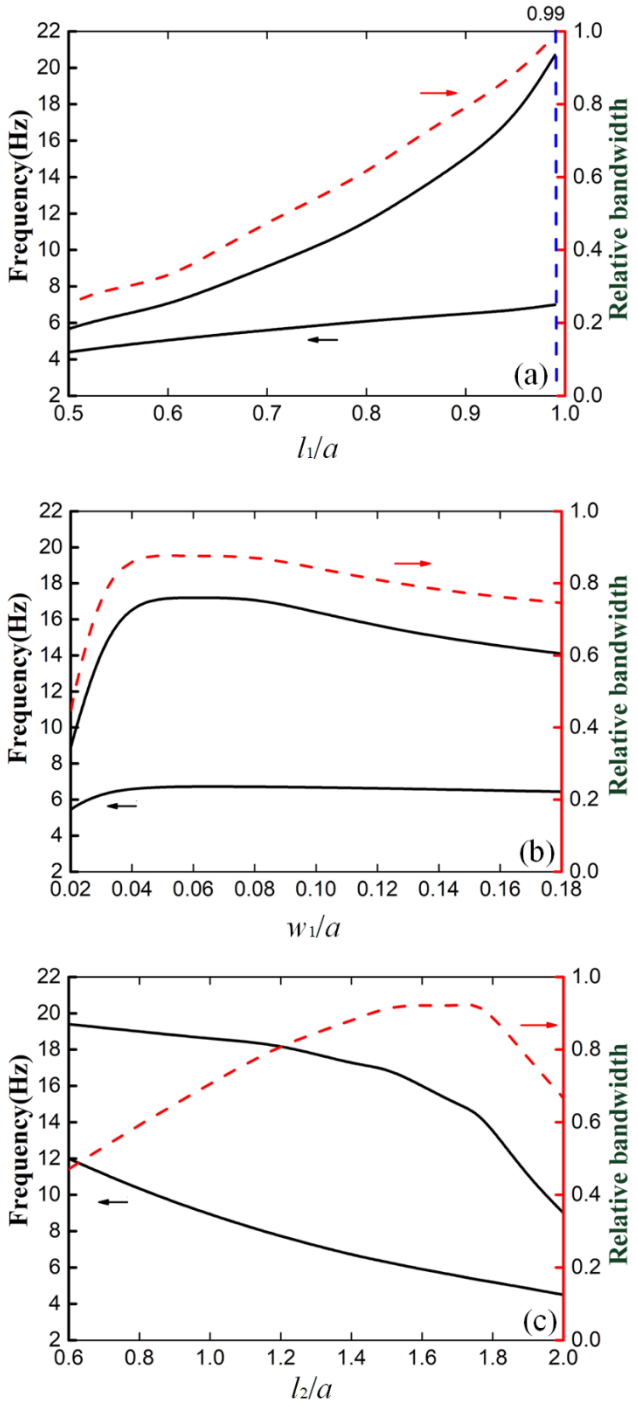

Figure 4-3 Effects of geometric parameters on first bandgap

Variation of the upper and lower frequency boundaries, and the relative bandwidth of the first bandgap with the ratio of the geometric parameters (a) l_1, (b) w_1 and (c) l_2 to lattice constant a

Figure 4-3(c) shows the effect of the pillar height on the FBG. When the pillar height continues to increase from 0.6a to 1.7a, the upper and lower boundaries of the FBG continue to decline, and its relative bandwidth continues to increase. But when the pillar height is greater than 1.8a, the upper boundary of the FBG drops rapidly, leading to the decrease of the relative bandwidth. Therefore, when the pillar height is about 1.7a, the relative bandwidth of the FBG of the ITSM is the largest, about 0.93.

The results show that the geometric parameters of the plate and pillar in the ITS have an obvious effect on the relative bandwidth of the FBG. With the appearance of the plate and the increase in its length, although the center frequency of the FBG of the ITSM continues to increase, its relative bandwidth increases linearly. However, there is an optimal value for the thickness of the steel plate, about 0.05a. When the height of the pillar continues to increase within a certain range, the center frequency of the FBG continues to decrease, but the relative bandwidth continues to increase. However, when the pillar is too high and its width is too small ($l_2 \times w_2$ is constant), the decrease in the flexural resonance frequency of the pillar causes the relative bandwidth to decrease continuously.

4.1.4 **Effects of material parameters**

In this section, the influence of material parameters of the ITS on the FBG is analyzed. Material parameters of the ITS are swept only for qualitative comparison.[200] Only one parameter is changed at a time, and other parameters are consistent with those in Fig. 4-1(b).

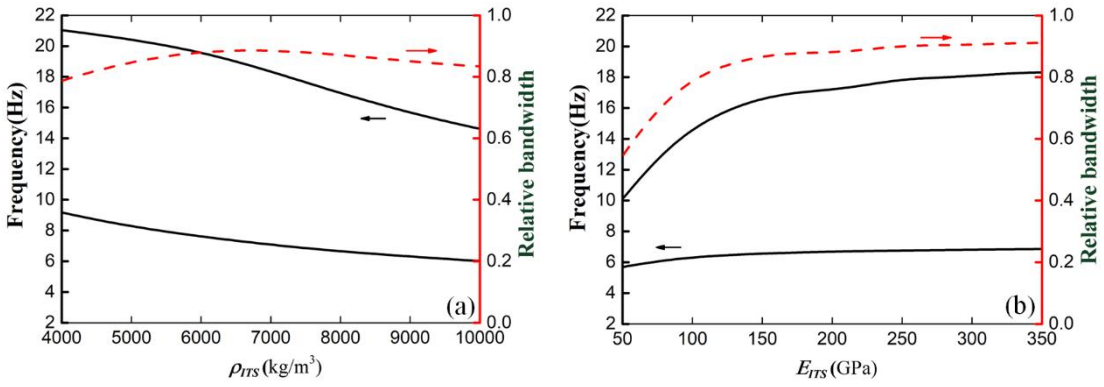

Figure 4-4 Effects of material parameters on first bandgap

Variation of the upper and lower frequency boundaries, and the relative bandwidth of the FBG (a) the mass density ρ_{ITS} and (b) the Young's modulus E_{ITS}. The black solid line is the upper and lower boundaries of the FBG, and the red dashed line is the relative bandwidth

The effect of mass density of the ITS (ρ_{ITS}) on the FBG is shown in Fig. 4-4(a). When ρ_{ITS} increases from 4000 kg/m^3 to 10000 kg/m^3, the lower boundary of the FBG decreases from 9.1 Hz to 6.0 Hz; and the upper boundary reduces from 21.0 Hz to 14.5 Hz. The center frequency of the FBG keeps dropping. However, the relative bandwidth first increases and then decreases, and its maximum value is about 0.9 when ρ_{ITS} is about 7000 kg/m^3. The effect of Young's modulus of the ITS (E_{ITS}) on the FBG is shown in Fig. 4-4(b). When E_{ITS} increases from 50 GPa to 350 GPa, the lower boundary increases slightly. When E_{ITS} increases from 50 GPa to 180 GPa, the upper boundary rapidly increases from 10.0 Hz to 17.0 Hz. Finally, the frequency slowly increases to 18.2 Hz, when E_{ITS} increases from 180 GPa to 350 GPa. Therefore, the relative bandwidth rapidly increases from 0.54 to 0.88, and it has just little change when E_{ITS} is larger than 180 GPa. These results show the ITSM has the FBG with largest relative bandwidth when ρ_{ITS} is about 7000 kg/m^3 and E_{ITS} is larger than 180 GPa. In reality, steel is the best choice for the ITS.

4.1.5 **Complex band structures**

In order to deeply explore the wide FBG of the ITSM, the complex band structures shown in Fig. 4-5(a), are calculated by using the PDE module of the COMSOL. The complex band structures of seismic metamaterials are considered when the wave vector is complex. The negative wave vector means that the amplitude of elastic wave is attenuated in the space, i.e., there is a surface evanescent wave.[164,200] In order to draw only the surface modes in the complex band structure, the following parameter ξ is introduced,[163,198]

$$\xi = \int_{S(2\lambda)} |\boldsymbol{u}| ds \,/\, \int_{S(H)} |\boldsymbol{u}| ds \ , \tag{4-1}$$

that is, in the displacement fields of the ITSM, the ratio of the integral of the displacement ($\boldsymbol{u}$) in the range of depth of twice the Rayleigh wave wavelength (2λ) below the surface to the integral of the displacement over the entire depth (H) of the substrate. The parameter ξ can be used to filter all surface modes from the complex band structure by using the displacement fields calculated with the finite element method (COMSOL Multiphysics). In this paper, the surface mode is defined as $\xi > 0.9$. This is because when the parameter $\xi > 0.9$ in one mode, i.e., more than 90% of the energy in a unit cell all exists near the surface, this mode can be deemed as a surface

mode. In Fig. 4-5(a), the color bar on the far right represents the value of ξ. The black dotted line is the boundary of the sound cone.

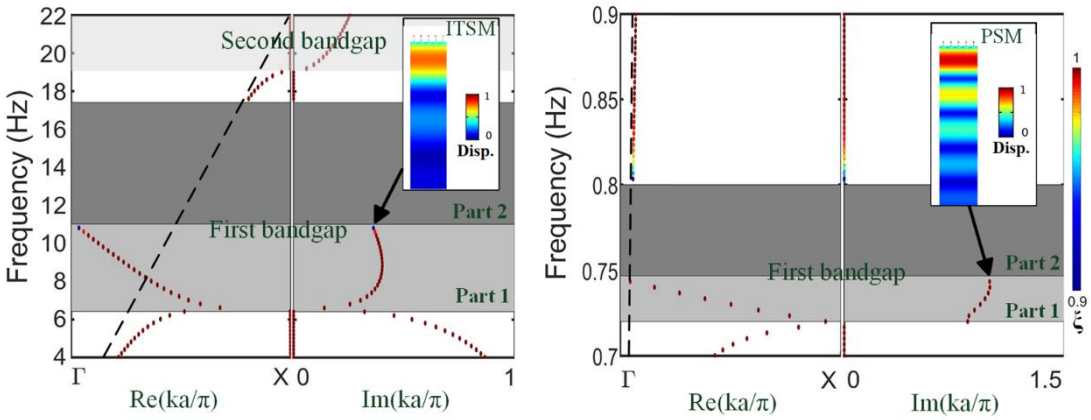

Figure 4-5 The complex band structures

The complex band structures of (a) the 1D ITSM and (b) the PSM.

In the complex band structure of the ITSM, the FBG can be divided into two completely different parts: part 1 with surface evanescent waves (light gray); part 2 with no surface mode (heavy gray). From the real part of the complex band structure of the ITSM, there is a surface band in the FBG in part 1, with a frequency range from 6.7 Hz to 11.0 Hz. This band partially overlaps with the first band at about 6.7 Hz. In the imaginary part of the surface band in part 1 are all greater than zero. They are surface evanescent waves in this frequency range and cannot be displayed in the classical band structure. The vibration mode at the end of the band is plotted. It can be found that most of the vibration exists in the substrate and decreases with increasing depth. We speculate that as the frequency increases, most of the vibration is transferred to the substrate thus the surface mode disappears. In part 2 with the frequency range of 11.0 Hz to 17.2 Hz, there is no surface band in the complex band structure of ITSM. Similar phenomenon is currently only found in the inverse-dispersion SMs. We speculate that in this frequency range, the steel structure can be equivalent to a layer of uniform medium on the substrate due to its longitudinal resonance (vibration perpendicular to the surface of the substrate). The layered media structure composed of this medium and the substrate has an inverse dispersion BG. In this frequency range of the BG, the surface waves will be converted into bulk waves.

Similarly, as shown in Fig. 4-5(b), as a comparison, the complex band structure of the FBG of the PSM shown in Fig. 4-1(a) is calculated. It is easy to find that the situation in these two FBGs is almost identical. So, we believe that the formation mechanism of these two FBGs is almost the same.

4.1.6 **Frequency domain analysis**

The transmission spectrum is calculated in this section. The finite model used for calculation is shown in Fig. 4-6(a), and consisting of two parts: the substrate represented by the yellow part, and the periodic ITSs represented by the gray part and the green part. The material and geometric parameters of the ITS are consistent with those in Fig. 4-1(b). The boundaries of the left, right, and bottom of the substrate are set as low reflection boundary condition to eliminate the reflection of elastic waves.[194,198] The number of rows of the ITSM is 10. Point A is set as the source to generate Rayleigh waves. The polarization direction of the source is the *xz* direction.[51,52,128] Accordingly, the data is collected at point B from the right side of the ITSM. Similarly, in order to obtain an accurate transmission spectrum at a sufficiently low-frequency range, the height of the substrate is set as $H = 300a$. The acceleration at point B is collected with and without the ITSM. When there is the ITSM, the acceleration at point B is A_1. When there is no ITSM, the acceleration at point B is A_0. The transmission is defined as $T = 20 \times \log_{10}(A_1 / A_0)$.

As shown in Fig. 4-6(b), the ITSM has a very significant attenuation effect on the Rayleigh waves in the frequency range of the FBG. There is a huge attenuation zone from 6.7 Hz to 17.2 Hz, consistent with the range of the FBG in Fig. 4-2(b). This result shows that the ITSM can drastically attenuate the Rayleigh waves at a sufficiently low frequency and in a wide range. In addition, it is easy to find that in the FBG's two different parts identified in complex band structure (Fig. 4-5(a)), the attenuation effects of the ITSM on Rayleigh waves are completely different. Because there are evanescent surface waves in part 1, the attenuation effect in part 1 is more pronounced than that in part 2. In part 1, the larger the value of the imaginary part is, the stronger the attenuation effect of the ITSM on Rayleigh waves is. Moreover, there is a strong attenuation of the surface waves from 19.1 to 22.0 Hz shown in Fig. 4-6(b). This is because that, in the second bandgap of the ITSM, there are evanescent waves shown in Fig. 4-5(a), and the surface waves are converted into bulk waves [137].

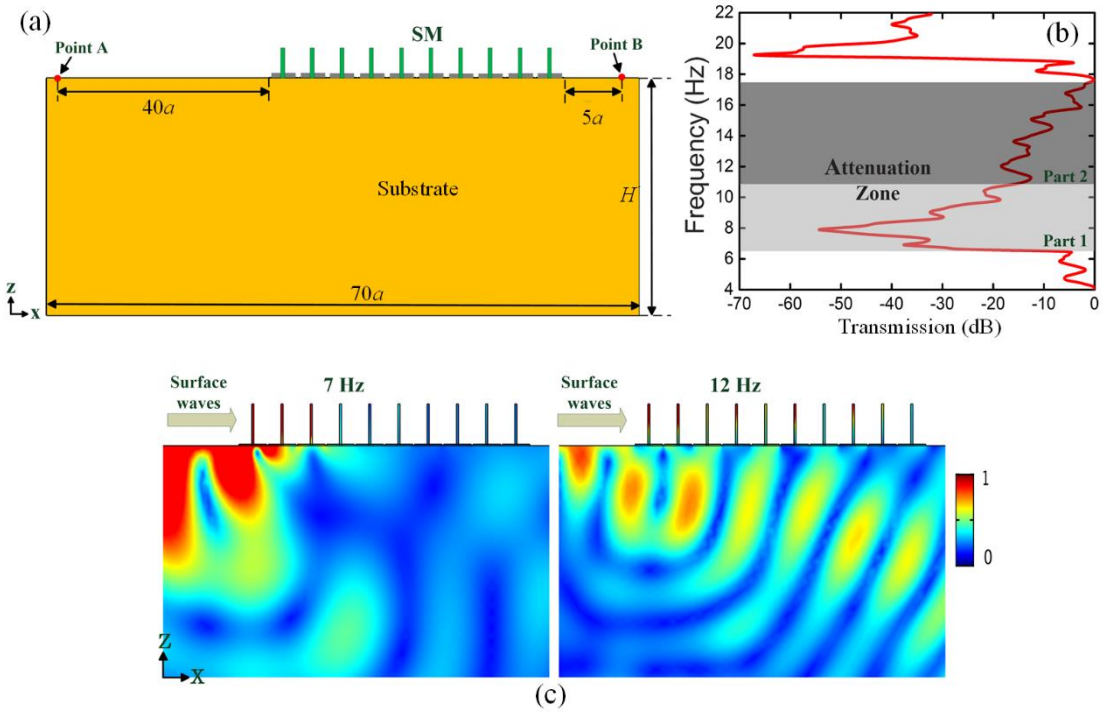

Figure 4-6 The transmission of Rayleigh waves in the ITSM

(a) Schematic model of the 1D ITSM with 10 unit cells for transmission calculations. (b) Transmission spectrum of the ITSM at the frequency range from 4 Hz to 22 Hz. (c) Distribution of displacement amplitude in the ITSM at 7 Hz and 12 Hz

As shown in Fig. 4-6(c), the distribution of displacement amplitude in the ITSM is given at two different but representative frequencies in the FBG: 7.0 Hz and 12.0 Hz. In the frequency range of part 1, for example, at 7.0 Hz, the violent resonance of the ITSM causes the surface waves to be significantly attenuated and almost unable to propagate to the third unit cell. In the frequency range of part 2, for example, at 12.0 Hz, after the surface waves enter the ITSM, we can observe that the surface waves are converted into bulk waves. These two results are easily reminiscent of the literature, [35] where surface waves are incident from two ends of the metawedge. When the surface wave is incident from the short edge, the surface waves first encounter part 1 of the FBG of the shorter PSM. So, the surface wave is quickly attenuated because of the evanescent waves. When the surface wave is incident from the taller end, the surface waves first encounter part 2 of the FBG of the taller PSM. So, the surface waves are converted into bulk waves because of the inverse-dispersion effect. This also indirectly proves that the formation mechanism of the FBG of the PSM and the ITSM is almost the same. So, in this work, the bandgap from 6.7 to 11 Hz is used to stop the propagation

of the Rayleigh waves. And the bandgap from 11 to 17.2 Hz is used to convert Rayleigh waves into bulk waves. In conclusion, the ultra-wide bandgap from 6.7 to 17.2 Hz is useful to attenuate Rayleigh waves to protect the aimed buildings.

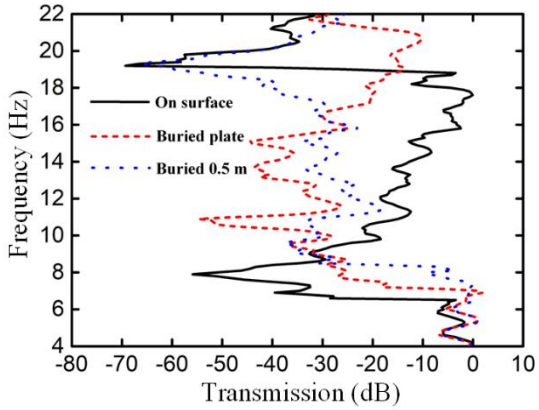

Figure 4-7 Transmission of Rayleigh waves in different ITSMs

Moreover, the propagation of the Rayleigh waves is studied when the bottoms of the steel structures are buried in the substrate. Figure 4-7 shows the transmission of the Rayleigh waves in the 1D ITSM with different burying depths. When the steel structures are buried in the substrate, the coupling of the structures of the substrate is improved to strongly attenuate more energy of Rayleigh waves at higher frequencies than the original ITSM. However, when the steel structure is buried deeper into the substrate, the lower boundary of the attenuation area is also rising.

4.2 The 2D ITSM and large-scale field experiments

For the SM, a 1D periodic model is a general choice for exploring mechanism of the BGs.[52,163,194] This is because it is a common method to study the SMs for surface waves, especially for Rayleigh waves, whose displacement components on the surface only exist in the *x* and *z* directions.[128] These two directions are both considered in the 1D simulations. Therefore, the 1D simulation is the basic study of the elastic metamaterials for surface waves. We can easily investigate the bandgap characteristic and the mechanism of bandgaps to easily design the 2D elastic metamaterials. However, in practical applications, the design of the 2D periodic SM is more important and necessary.[34,137,168] In addition, due to some uncontrollable factors in actual situations,

such as the difficulty of achieving perfect continuity between different materials, large-scale field experiments are still needed to verify the SMs with ultra-wide and low-frequency bandgaps for surface waves. Therefore, based on the design concept and the mechanism of the above-mentioned 1D ITSM, a kind of 2D ITSM and large-scale field experiments are designed for isolating Rayleigh waves in this section. It is worth noting that due to the experimental equipment and test site, the 2D ITSM with smaller dimensions than the 1D ITSM are chosen. However, the operating frequency and frequency range of the 2D ITSM are lower and much wider than the SMs that has been experimentally verified.[33,133]

4.2.1 The 2D ITSM and experimental setup

Fig. 4-8(a) shows the unit cell of the 2D ITSM designed according to the structure of the 1D ITSM. In order to facilitate field experiments and attenuate seismic surface waves in the lower frequency range, the lattice constant a_1 of the unit cell is set as 0.25m. And the unit cell is composed of a thumbtack-shaped structure (purple part) and a soil substrate (gray part). Among them, the thumbtack-shaped structure (TS) is composed of a steel tube and a steel plate. The geometric parameters of the unit cell are shown in Table 4-3. As shown in Fig. 4-8(b), the central garden of the Department of Mechanics on the Beiyangyuan Campus of Tianjin University (China) was selected for large-scale field experiments in August 2020. The geometric parameters of the TS used in large-scale filed experiments are consistent with those in Fig. 4-8(a). Among them, the steel tube and steel plate are rigidly connected by high-strength bolts. 25 identical TSs are customized and periodically arranged on the substrate.

Table 4-3 The geometric parameters

a_1	b	t	h	D	d
0.25 m	0.2375 m	0.012 m	0.75 m	0.051 m	0.041 m

Considering the viscoelasticity and non-uniformity of the soil, we use the controlled variable method: using two sensors (uT, A21D100) with the same distance to the source to measure the acceleration of the two points (points A and B shown in Fig. 4-8(b)). The vibration source is generated by the rammer (Mingtu Mechanics, C90t)

with an exciting force of 20kN. The data of two sensors is collected by the signal collector (uT, uT3604FS-ICP), and processed by the computer to obtain the response results at the two points. When the TSs are not placed in the field, the responses of the two points are almost the same when the rammer works. Therefore, this experiment can almost eliminate most uncontrollable factors, and only focus on the influence of the presence of artificial structures on the propagation of Rayleigh waves. The transmission of Rayleigh waves by the TSM is defined as $20*\log_{10}(A_A/A_B)$ [194], where A_A and A_B are the accelerations in the vertical direction of points A and B, respectively. The material parameters of the tests is referenced in these literatures [152,160], which is same as in Tables 4-2. It is worth noting that in the tests, the TS is simply placed on the substrate. But in the simulation mentioned above, the TSs and soil are perfectly continuous.

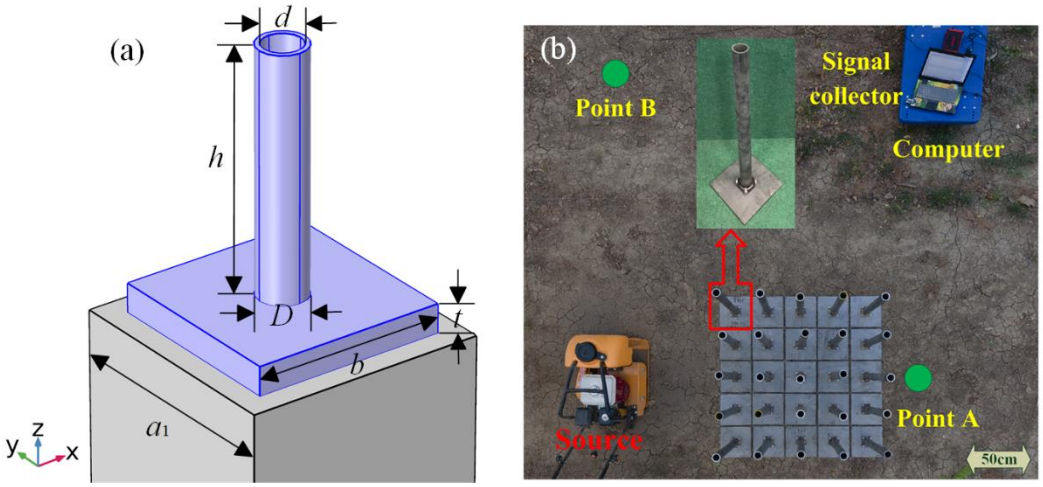

Figure 4-8 The experimental setup

(a) Schematic of the unit cell and (b) top view of the experimental setup

4.2.2 **Results of the 2D ITSM**

The band structure of the 2D ITSM only in the ΓX direction is calculated to facilitate comparison with the experiments, as shown in Fig. 4-9(a).[34,137,156] The sound cone is clearly surrounded by the light gray areas. The vibrating mode of the highest point of the first band is given in the insert of Fig. 4-9(a). The displacement is in *x* direction and mainly concentrated on the top of the steel tube. The vibrating mode of the second band exhibits also a displacement distribution mainly concentrated on the

top of the steel tube but in *y* direction. The surface waves considered in this work are Rayleigh waves, whose displacement components on the surface only exist in the *x* and *z* directions.[128] The Rayleigh waves can excite the ITSM to vibrate in the frequency range of the first band, but not the second band, i.e., they can propagate in the ITSM in the frequency range of the first band, but not the second band.[134,154] Therefore, the bandgap starts from the highest point of the first band. The bandgap of the ITSM for Rayleigh waves is in the range of 34-130 Hz, which is marked by the light gray part in Fig. 4-9(a).

In Fig. 4-9(b), the black line is the simulation results when there is perfect continuity (PC) between the man-made structures and substrate. The red dash line is the simulation results when there is imperfect continuity (IPC) between the man-made structures and substrate. And blue dot line experimental results. The model used in the simulation is the same as the experimental site. Moreover, the influence of the continuity between the man-made structures and the substrate on the attenuation of Rayleigh waves is analyzed. A very thin (t = 0.02a) low-density material (Young's modulus is 20 GPa, density is 1.8 kg/m^3 and Poisson's ratio is 0.3) is added underneath all man-made structures to simulate the IPC between soil and the structures. It is worth noting that the inexistent low-density material is used just to qualitatively investigate the effect of the IPC on the attenuation of Rayleigh waves. In the range of 34-130 Hz, Rayleigh waves are attenuated significantly. It can be found that the attenuation effect in the simulated results with the PC is generally stronger than the results of the field test. However, the simulated results with the IPC are closer to the experimental results, especially in the range from 40 to 60 Hz. This is because the simple connection between the TSs and the soil in the field test is weaker than the perfect connection in the simulation. In addition, it is worth noting that in the bandgap, experimental and simulated results all show that the attenuation of Rayleigh waves is stronger at the band of 34-70 Hz than the one of 70-130 Hz.

In the cross-sectional and top views of simulation results with PC, it is easy to find that the propagation of Rayleigh waves in the ITSM is completely different at 44 and 100 Hz, respectively. Figure 4-10 shows the simulated results of propagation of Rayleigh waves without the 2D ITSM at 44 and 100 Hz, respectively. The boundary conditions of the system in the simulation are all low-reflection boundary condition, except the free boundary condition for the upper surface.

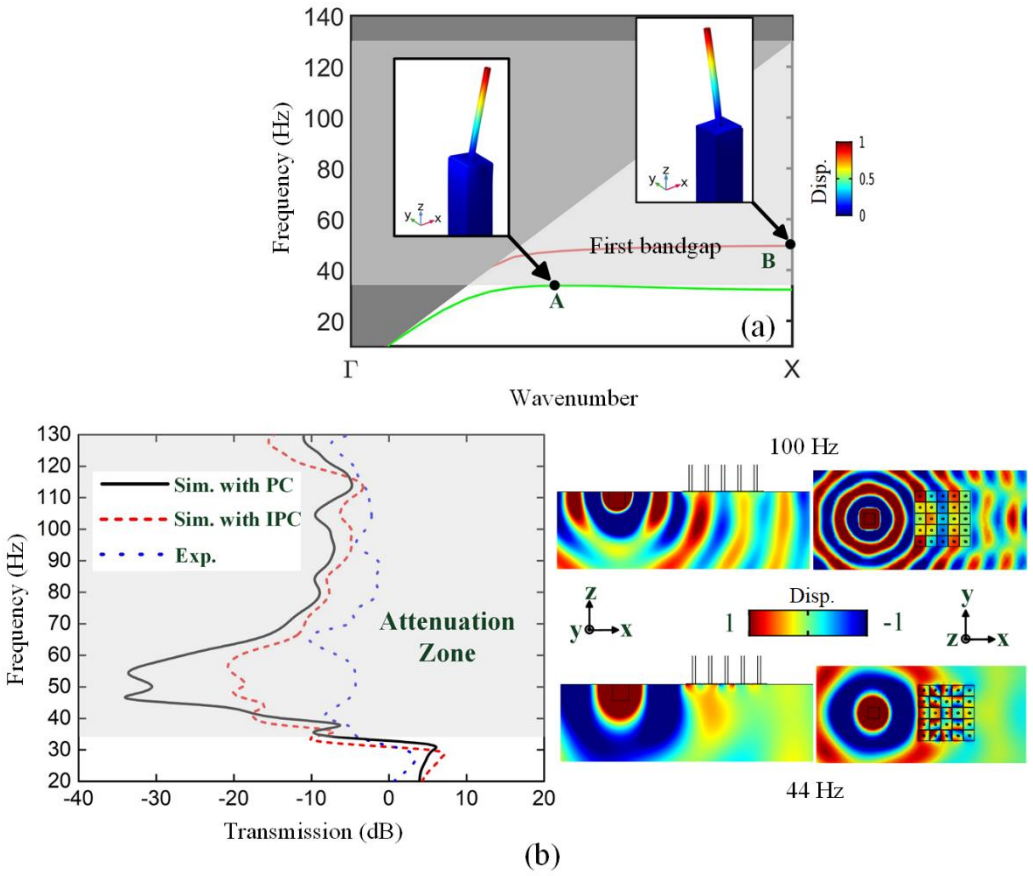

Figure 4-9 The results of the 2D ITSM

(a) the band structure in the ΓX direction of the first irreducible Brillouin zone of the 2D ITSM. (b) The transmission spectrum of the simulated and experimental results along ΓX direction through the 2D ITSM.

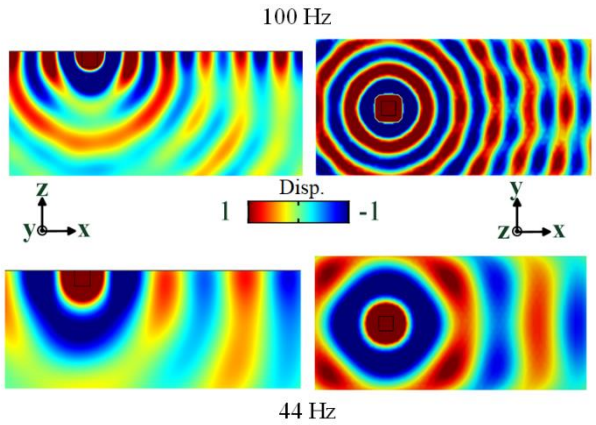

Figure 4-10 The simulated results of propagation

Same as the PML, the low-reflection boundary condition is usually used to reduce the unnecessary reflection in simulations. All the boundaries and physical fields are same as that in Fig. 4-9(b), but without the man-made structures. This is consistent with the results in Fig. 4-6(c): the attenuation in the bandgap generated by the local resonance is stronger than that by inverse-dispersion characteristics when the rows of the unit cell are fewer (5 rows in this work). Regarding the application, the ITSM is proposed for a metropolis with different buildings. The ITSM with an ultra-wide bandgap can be used around the metropolis to strongly attenuate seismic surface waves to protect almost all the buildings in the metropolis. If the number of the rows of the ITSM is large, for example, the ITSM with 30 rows can theoretically attenuate the energy of seismic waves hundreds of times. Also, the ITSM can be used to protect critical infrastructures, like nuclear power station.

4.3 Conclusion

In this chapter, an 1D ITSM with an ultra-wide FBG has been proposed by improving the pillar-like SM. The effects of the geometrical and material parameters of the ITSM on the FBG have been also discussed. It is found that the appearance of the plate obviously increases the center frequency and relative bandwidth of the FBG of the ITSM. The complex band structure of the ITSM has been calculated to analyze the attenuation mechanism of surface waves. It can be found that the FBG of the ITSM is composed of two parts. It was found that the propagation modes of surface waves in the ITSM are completely different in different parts of the FBG. In the frequency range of part 1, the seismic surface waves are significantly attenuated and almost unable to propagate to the third unit cell in the ITSM. In the frequency range of part 2, the surface waves are converted into bulk waves. Finally, we have proposed a kind of the 2D ITSM with 25 unit cells in large-scale field experiments, which can attenuate Rayleigh waves in a ultra-wide frequency range. This work not only provides new options for controlling seismic surface waves at ultra-low frequency, but also provides new design ideas for steering surface wave.

Chapter 5 Rainbow trapping effect of gradient seismic metamaterials with ultra-wide frequency isolation design

In the past two decades, in the fields of applied physics, mechanics and civil engineering, the use of metamaterials to control wave propagation has attracted great attention.[138,146,151,154,161,163,169,176,179,182,203,210,211] Regarding surface waves, the lowest-frequency attenuation zone (LFAZ) of the elastic metamaterials composed of an array of artificial structures on a substrate is the most appealing and interesting, since their working wavelengths are well above their characteristic size.[135,152,155,156,163] In the LFAZ, a number of experiments [155,181] and numerical studies [135,154,156,163] have demonstrated that surface waves can be strongly attenuated because of the local resonance of the artificial structures on the substrate. It is worth mentioning that this conclusion is always valid whether the materials of the substrate and the artificial structures are the same or not.[135,155,156,163] However, the width of the LFAZ is usually narrow. Therefore, the second attenuation zone (SAZ) whose frequency is slightly higher than the LFAZ attracted our attention.

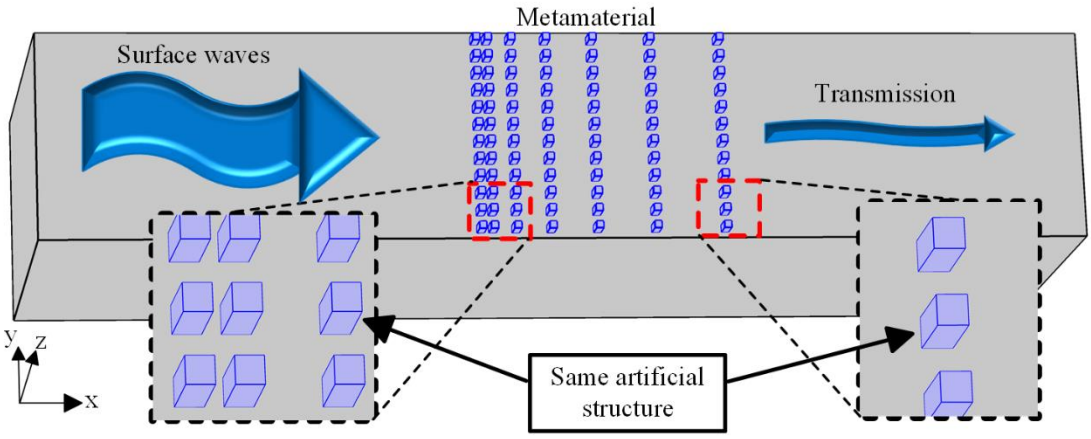

Figure 5-1 The schematic diagram of a kind of the elastic metamaterial

In this chapter, we propose alternative approaches to overcome these challenges. We report the properties of the LFAZ of a pillar-shaped elastic metamaterial. Then, we experimentally demonstrate the “rainbow trapping effect” of the SAZ of an elastic metamaterial composed of one kind of pillars with various lattice constants on a

substrate. These two features of these two attenuation zones allow us to connect lower bound of the SAZ and the upper bound of the LFAZ, and design elastic metamaterials using one kind of artificial structures to attenuate surface waves over a wide low-frequency range. Figure 5-1 shows the schematic diagram of the elastic metamaterial. We consider the seismic Rayleigh waves as an example, and design a seismic metamaterial (SMS) just using one kind of artificial structure on a half-space, which can attenuate Rayleigh waves in the frequency range from 5 Hz to 22 Hz.

5.1 First attenuation zone

An elastic metamaterial composed of steel pillars (width w = 0.3 m, height l = 0.75 m) periodically arranged with a lattice constant of 1.5 m on a soil substrate is taken as an example to investigate the properties of the LFAZ. The depth of the substrate is H = 500a, which is much larger than two times of the wavelength (2λ) of the surface waves. The bottom surface of the unit cell is set as fixed boundary condition. The considered material parameters of steel are 207 GPa, 7784 kg/m^3 and 0.3 for the Young's modulus, the density and the Poisson's ratio, respectively. For the soil substrate, the material parameters are 20 MPa, 1800 kg/m^3 and 0.3 for the Young's modulus, the density and the Poisson's ratio, respectively.[34,52]

Figure 5-2(a) shows the complex band structures of the elastic metamaterial for surface waves from 4.5 to 6.0 Hz calculated by the PDE module of the COMSOL Multiphysics software. The dotted line of c_s is the shear wave speed of the substrate material, i.e., the boundary of the sound cone.[137,156] All the modes at the right side of the dotted line are surface waves, but there are also some other surface modes, i.e., pseudo surface waves, at the left side of the dotted line.[163,164] To draw all the surface modes in the band structure, the parameter ξ is introduced, i.e.

$$\xi = \int_{S(2\lambda)} |\boldsymbol{u}| ds \,/\, \int_{S(H)} |\boldsymbol{u}| ds, \tag{5-1}$$

which is the ratio of the displacement ($\boldsymbol{u}$) in a depth of twice (2λ) of the Rayleigh wave wavelength to the entire depth (H) of the substrate.[163,193] The full complex band structure ($1 > \xi > 0$) is shown on the left of the Fig. 5-2(a). Surface mode is defined as having parameter $\xi > 0.9$. The complex band structure for surface modes ($\xi > 0.9$) is shown on the right of the Fig. 5-2(a). The first bandgap is found from 5.0 to 5.4 Hz. Although there is a band of surface modes from 5.0 to 5.2 Hz, the surface waves are

continuously attenuated as the distance traveled increases in this frequency range. Because the imaginary part of the wave vector of this band is positive, i.e., the wave mode of this band is evanescent [200,201] with strong attenuation. The surface vibration mode, which falls before the c_s line on this band, is shown in the far-right of Fig. 5-2(a). Most of the vibration exist in the substrate and decrease with increasing depth. The vibration mode of the pillars on substrate is similar as the one on the first band below 5.0 Hz.[163] It is worth noting that the curve of the imaginary part should start from the end of the real part at the high symmetry Brillouin points from 5 to 5.15 Hz. However, the ideal results are difficult to calculate because the results are extremely dense at the junction.

The most interesting feature of the first bandgap is its immobility nature. The system composed of the substrate and an artificial structure is regarded as a spring-mass model. The resonance frequency of the spring-mass model is fixed if the substrate and the artificial structure are both not changed. So, the first bandgap due to the resonance of the spring-mass models is unchanged, even if the distribution of the artificial structures in the elastic metamaterial varies. Figure 5-2(b) shows the upper and lower frequency bounds of the first bandgap when only the lattice constant of the elastic metamaterial is changed. It is found that the first bandgap is absolutely unchanged due to the immobility of the lower frequency bound at 5.0 Hz, although the upper one decreases from 5.5 Hz to 5.2 Hz.

Figures 5-2(c) shows a part of the elastic metamaterials composed by 30 steel pillars periodically arranged with a lattice constant of 1.5 m, 3 m, and randomly arranged within 75 m on soil substrate, respectively. The geometric parameters of the steel pillars are consistent with those in Figs. 5-2(a). A perfectly matched layer (PML) with a thickness of 50a is added around the substrate to prevent reflections. The transmission of Rayleigh waves in these three elastic metamaterials are shown in Fig. 5-2(d). It is clearly found that these three different arrangements have the same LFAZ around 5.0 Hz. This shows that the LFAZ is immobile with the changed distances between the pillars. The spring-mass model consisting of the pillar and substrate has not been changed. Therefore, the resonance frequency of the spring-mass model remains the same. Even if the same material is used for the pillars and the substrate, this phenomenon still exists, which has been experimentally demonstrated.[181] It is worth

noting that the strong attenuation of the surface waves in the SMS with the lattice constant of 3 m from 9 to 11 Hz is due to the existence of the second and third bandgaps.

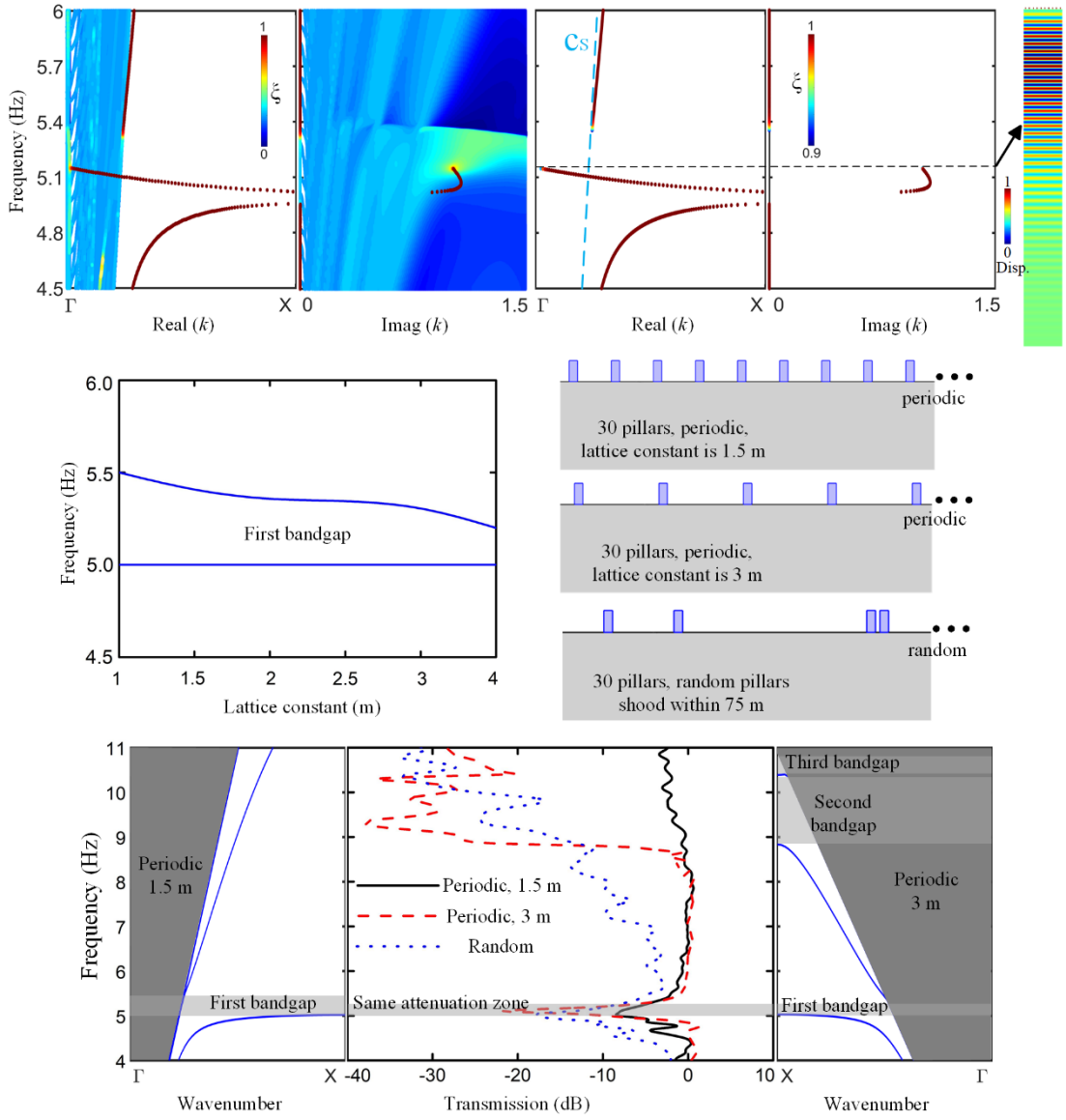

Figure 5-2 Study of the first bandgap

(a) The complex band structures of the elastic metamaterial around the first bandgap. (b) The upper and lower frequency bounds of the first bandgap with various lattice constants of the elastic metamaterial. (c) Partial illustrations of two periodic arrangements of steel pillars with the lattice constants of 1.5 m, 3 m on a soil substrate and random arrangement of steel pillars on a soil substrate within 75 m. (d) The transmission of Rayleigh waves in the three elastic metamaterial

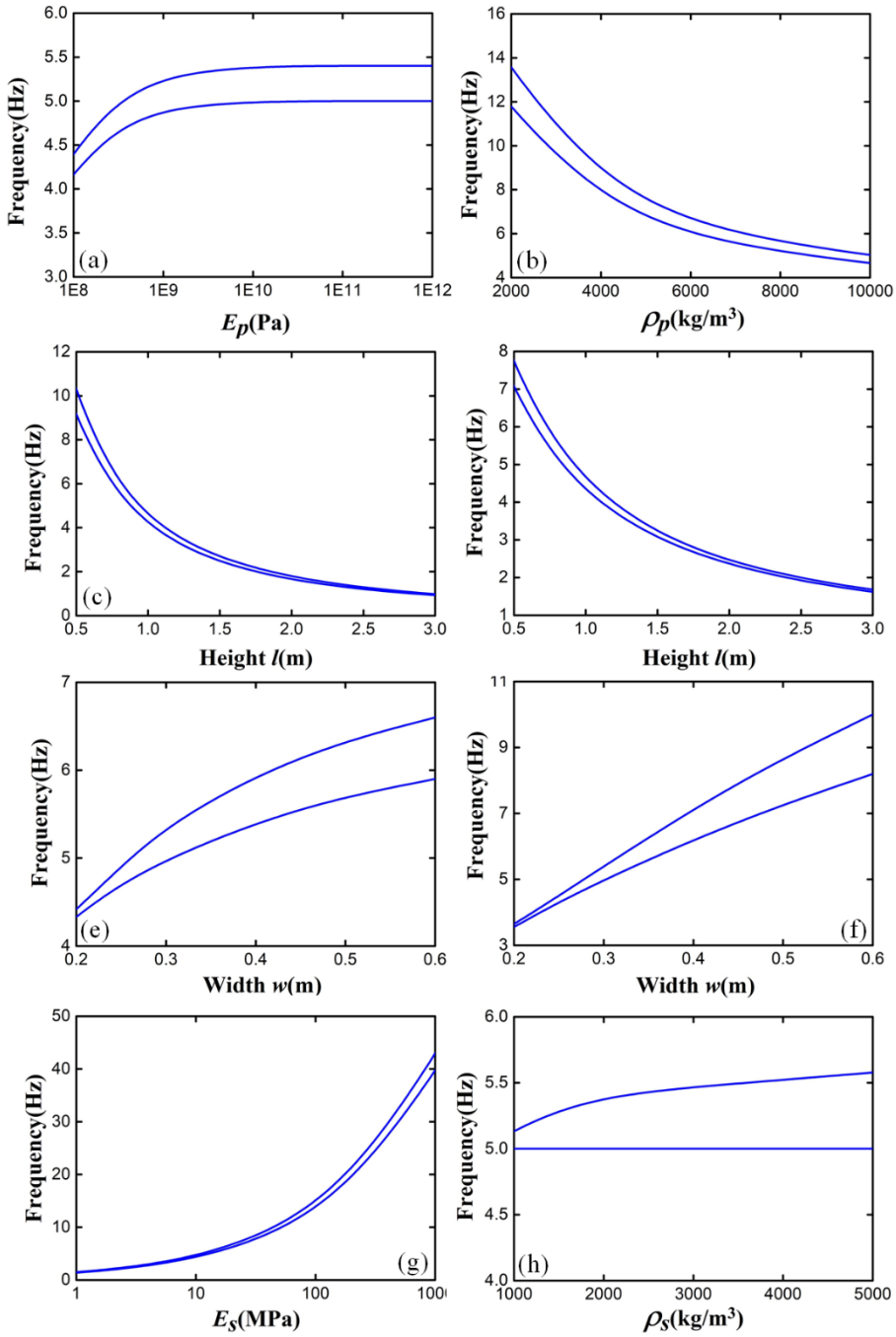

Figure 5-3 The effects of the parameters on the first bandgap

The effects of the (a) Young's modulus of the pillars, (b) density of the pillars, (c) height of the pillars when the density of the pillars is 7784 kg/m^3, (d) height of the pillars when the mass of the pillars is 0.3×0.75×7784 kg, (e) width of the pillars when the density of the pillars is 7784 kg/m^3, (f) width of the pillars when the mass of the pillars is 0.3×0.75×7784 kg, (g) Young's modulus of the substrate, (h) density of the substrate on upper and lower bounds of the first bandgap

The effects of the parameters of the pillars and the substrate on the upper and lower

bounds of the first bandgap are shown in Fig. 5-3. These parameters are swept only for qualitative comparison. Figure 5-3(a) shows that the center frequency of the first bandgap increases when the Young's modulus of the pillars increases from 0.1 GPa to 10 GPa. And when the Young's modulus of the pillars is larger than 10 GPa, the first bandgap is hardly changed. The position the first bandgap decreases continuously as the density of the pillar increases in Fig. 5-3(b). Figures 5-3(c - f) show the height and width of the pillar all play an important role in the position of the first bandgap whenever the density or the mass of the pillar is immobile. It is easy to find that the mass of the pillar on the substrate affects a lot on the first bandgap from Figs. 5-3(b - f). Figure 5-3(g) shows that the center frequency of the first bandgap increases rapidly when the Young's modulus of the substrate increases from 1 MPa to 1000 MPa. However, the density of the substrate is hardly to change the position of the first bandgap shown in Fig. 5-3(h). We find that except the density of the substrate, all these parameters can significantly move the position of the first bandgap.

5.2 Second attenuation zone

The LFAZ generated by the elastic metamaterials composed of an array of pillars on substrate is usually narrow.[43,96,153,163] Therefore, to obtain a wider attenuation zone in the low frequency range, the SAZ with a higher frequency than the LFAZ is investigated and discussed by using numerical simulations and experiments. Figure 5-4(a) shows the unit cell of the elastic metamaterial whose band structure can be numerically simulated by using the solid module of COMSOL Multiphysics. In this work, the bandgaps only in the ΓX direction of the first irreducible Brillouin zone are investigated. The numerical computations are described in Refs. [[137,156]]. The material of the unit cell is PLA (its Young's modulus is 3.4398 GPa, density is 1086.3 kg/m^3, Poisson's ratio is 0.35)[212] and the geometric parameters are shown in Table 1. The characteristics of the first and second bandgaps are always valid and do not change, whether the materials of the substrate and the artificial structures are the same or not.[135,155,156,163] Therefore, the proposed PLA models can accurately explore the basic properties of the bandgaps.

The effect of lattice constant *a* on the upper and lower frequency bounds of the first and second bandgaps is shown in Fig. 5-4(b). The first bandgap is quite stable with various lattice constants, which is consistent with the previous results. However, the

central frequency of the second bandgap keeps decreasing as the lattice constant increases. Therefore, this feature of the second bandgap is suitable to be used to obtain a wide attenuation zone at frequencies higher than the LFAZ through the "rainbow trapping effect"[35,152,213,214].

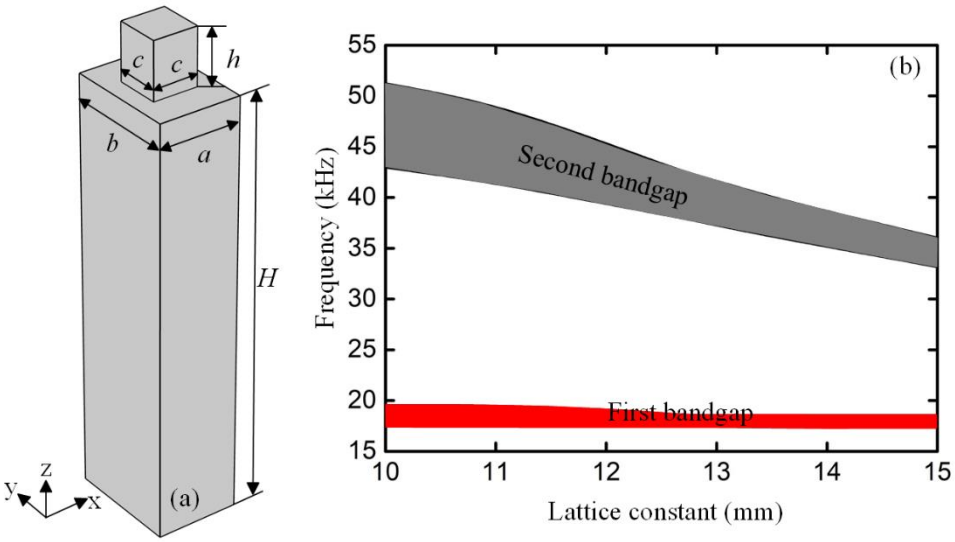

Figure 5-4 Study of the second bandgap

(a) The unit cell of the elastic metamaterial for surface waves, (b) the effect of the lattice constant *a* on the first and second bandgaps in the ΓX direction of the elastic metamaterial

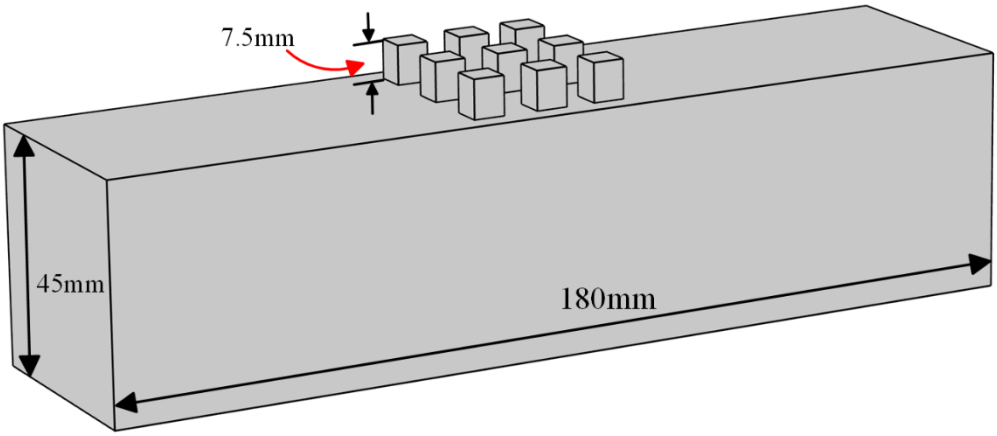

Figure 5-5 Geometric model for simulation calculations

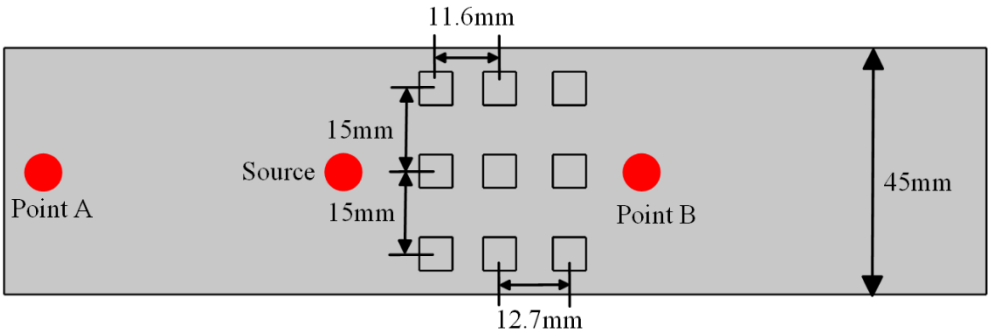

Figure 5-6 The top view of the geometric model for simulation calculations

Table 5-1 The geometric parameters of the metamaterial

a	*b*	*c*	*h*	*H*
Lattice constant	15 mm	6 mm	7.5 mm	300*a*

Metamaterial samples composed of three rows of PLA pillars with different lattice constants of 13.2 mm, 12.2 mm and 11 mm on a PLA substrate have been considered for simulations and fabricated for experiments. From Fig. 5-4(b), it can be found that the SAZ of the considered sample extends from 37 kHz to 50 kHz due to the "rainbow trapping effect" of the second bandgap. The data of two points on the samples is selected in the simulations and experiments to measure the attenuation effect of the elastic metamaterial for surface waves.

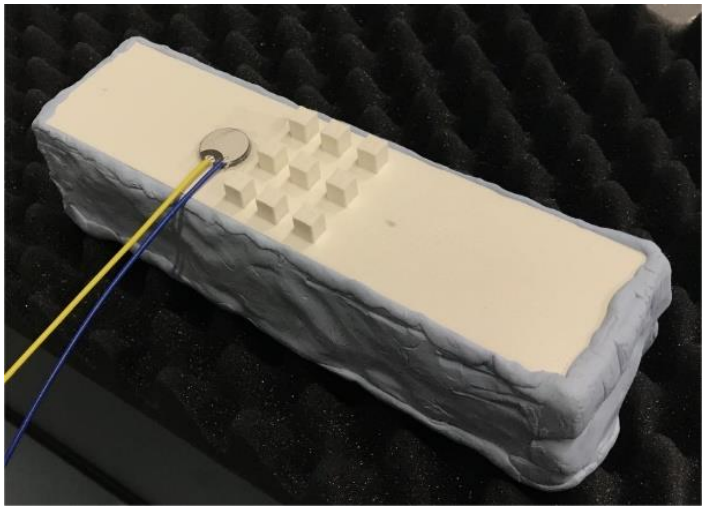

Figure 5-7 The sample for experiments

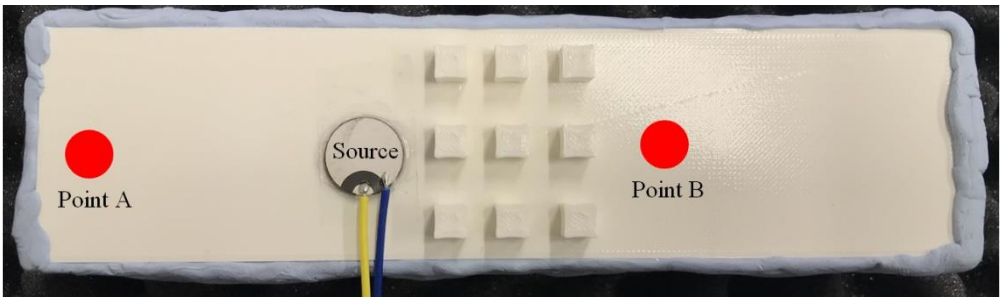

Figure 5-8 The top view of the sample for experiments

Figure 5-9 The experimental layout

Figures 5-5 and 5-6 are the geometric models used in the simulation calculations. In simulation calculations, the low reflection boundaries are set on the four vertical boundaries and the bottom boundary to simulate the half-space and reduce the influence of the reflected waves. Excite z-direction excitation at the source point, and measure z-direction accelerations (A_A and A_B) at two points A and B which have the same distance from the source. Then the transmission spectrum (TS) of the elastic metamaterial is about TS = $20\log(A_B/A_A)$. Figures 5-7 and 5-8 show the experimental sample. Its geometric dimensions are the same as those in Figs. 5-5 and 5-6. Strong damping material is attached to the side and bottom to reduce the reflection of elastic waves. The piezoelectric sensor is used at the source point to provide vibration in the z-direction. The propagation of elastic waves is measured on both sides of the elastic metamaterial by using the laser vibrometer (Polytec PSV-500). Then the accelerations of two points A and B are extracted. The method is the same as that in simulation calculations. Figure

5-9 shows the experimental layout. Label A is a computer, which is used to set the output signal of the piezoelectric sensor on sample B and process the input signal from the laser vibrometer C.

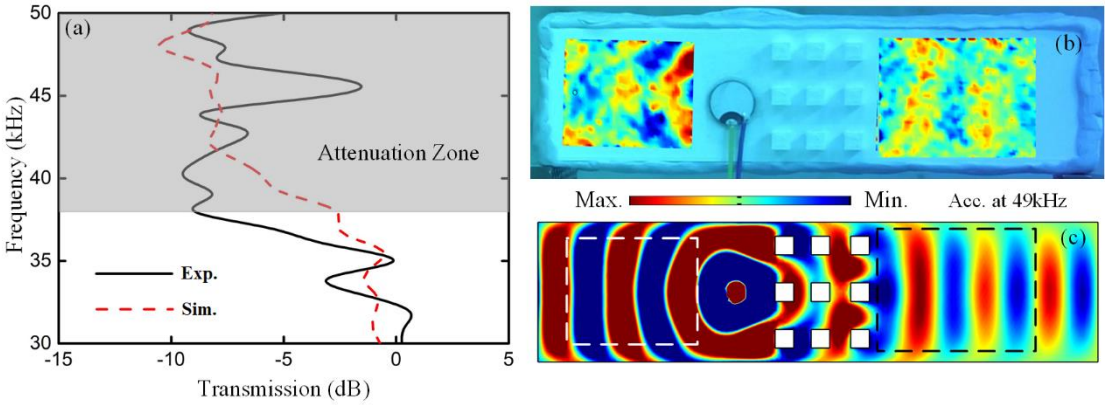

Figure 5-10 The transmissions of surface waves in the sample

(a) The transmissions of surface waves on the prepared samples in simulations and experiments. Propagations of surface waves on the sample (b) in the experiment and (c) in the simulation at 49 kHz. The color indicates the acceleration field on the surface of samples

Figure 5-10(a) illustrates the simulation and experimental measurements of the transmission of the surface waves through the considered metamaterial sample. One can observe that in the range of 37k - 50 kHz, the elastic metamaterial can significantly attenuate surface waves. We observe that there is a transmission peak at around 45 kHz. We do believe that the experimental transmission peak at around 45 kHz is due to the imperfect absorption of the damping material covered the substrate for elastic waves. Figures 5-10(b - c) show the out-of-plane acceleration fields on the surface of the samples in the experiment and simulation at 49 kHz, respectively. Limited to the number of rows of the pillars that compose the elastic metamaterial, the attenuation effects do not seem obvious in these fields. However, when the number of rows of the pillars increases and more suitable lattice constants are chosen, better attenuation ability and a wider SAZ can be obtained. Therefore, the elastic metamaterial constituted of pillars with different distances on a substrate presents a wide SAZ to attenuate surface waves. It is worth noting that these pillars are all the same.

5.3 Broadband seismic metamaterials

When an artificial structure on the substrate is determined, the LFAZ is immobile even if the distances between the structures are changed. However, the SAZ whose frequency is higher than the LFAZ becomes wider when choosing the suitable distances between the structures due to the "rainbow trapping effect". Therefore, for a properly designed elastic metamaterial, there is an opportunity to connect lower bound of the SAZ and the upper bound of the LFAZ. It is possible to propose an elastic metamaterial with a wide attenuation zone from an ultra-low frequency for surface waves just using one kind of artificial structures on a substrate.

Table 5-2 The geometric parameters of the ITSM

l_1	w_1	l_2	w_2
1.35 m	0.075 m	2.25 m	0.15 m

For instance, in this work, a kind of SMS with a wide attenuation zone for seismic Rayleigh waves is designed. Considering the wide range of the evanescent waves in the LFAZ of the seismic metamaterial, the inverted T-shaped structure is chosen.[215] As shown in Fig. 5-11(a), 15 identical inverted T-shaped steel structures are used. The geometric parameters are given in Table 5-2. In the numerical simulation, the ideally perfect continuity is assumed between the inverted T-shaped structure and the substrate. The 15 steel structures are placed with appropriate distances. The distances between the symmetry axes of each steel structure in this research are 4.9, 4.7, 4.5, 4.3, 4.1, 3.9, 3.7, 3.5, 3.3, 3.1, 2.8, 2.4, 2, 1.65m. Of course, other suitable artificial structures, number of the structures and distances can also be selected. This paper only gives one possibility.

As shown in Fig. 5-11(b), when Rayleigh waves are incident from left to right (LTR) or from right to left (RTL), the SMS can all attenuate the energy well in the range from 5.0 to 22.0 Hz. The attenuation of the Rayleigh waves in the SMSs is complex because the attenuation zone includes the frequency ranges of the first and second bandgaps. There are two mechanisms of the attenuation of the Rayleigh waves in the seismic metamaterial.

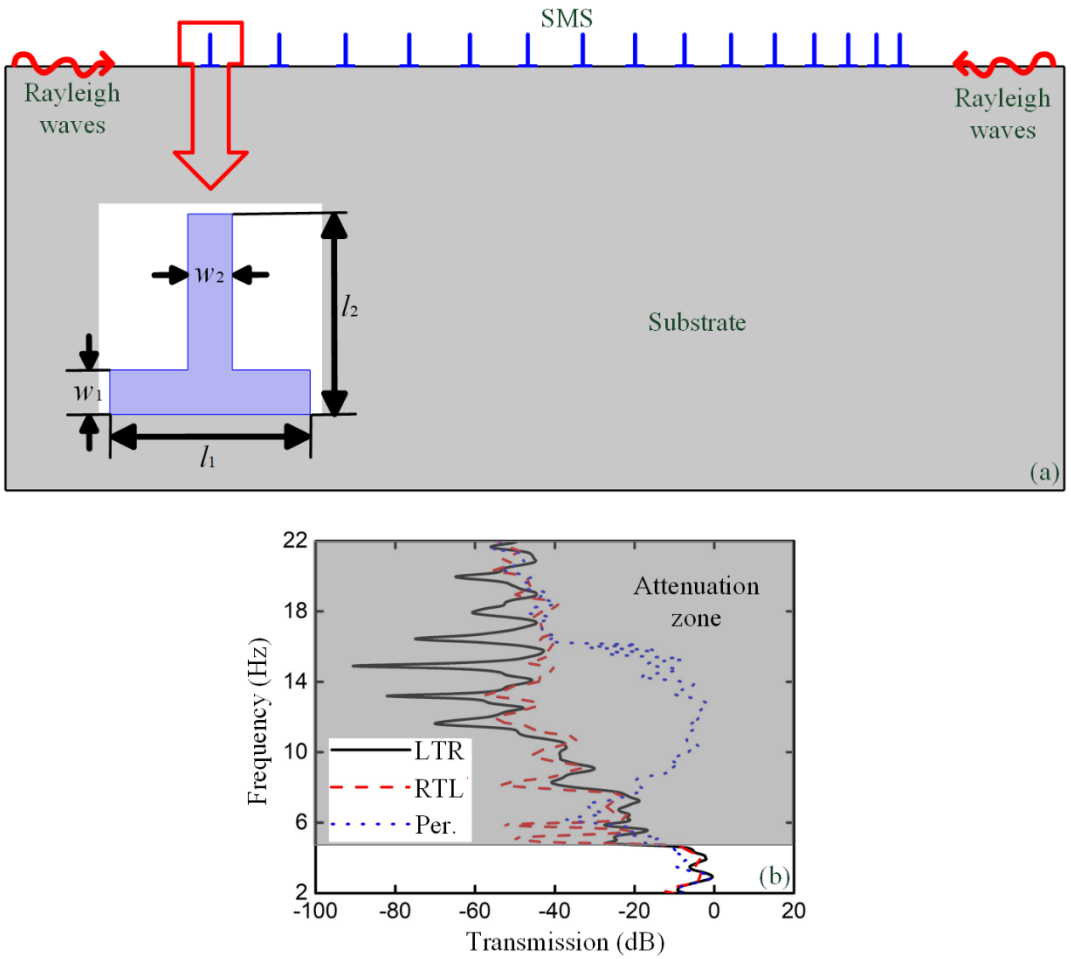

Figure 5-11 The transmissions of surface waves in the ITSM

(a) Schematic picture of the finite system used for transmission calculations of the seismic metamaterial, (b) the transmission of Rayleigh waves propagating in the seismic metamaterial from different directions, and the transmission of Rayleigh waves propagating in a periodic arrangement of the 15 inverted T-shaped structures with a lattice constant of 1.5 m. The gray area is the attenuation zone of the seismic metamaterial. The LTR, RTL and Per. mean "from left to right", "from right to left" and "periodic", respectively

The first one is the attenuation due to the local resonance of the artificial structures, while the second one is due to the conversion of the Rayleigh waves to bulk waves in the SMS. These two mechanisms of the attenuation of the Rayleigh waves in the SMS are shown in Figure 5-12. The Rayleigh waves are attenuated due to the local resonance of the artificial structures at 6.5 Hz; while are conversed to bulk waves at 20.4 Hz. Comparing with the SMS consisted of a periodic arrangement of inverted T-shaped steel structures with a lattice constant of 1.5 m on soil substrate, the "rainbow trapping effect"

of the SMS works well to block the passband from 8.0 Hz to 16.0 Hz. It is worth noting that there are many kinds of three-dimensional configurations coming from the two-dimensional one as shown in Fig. 5-11(a).

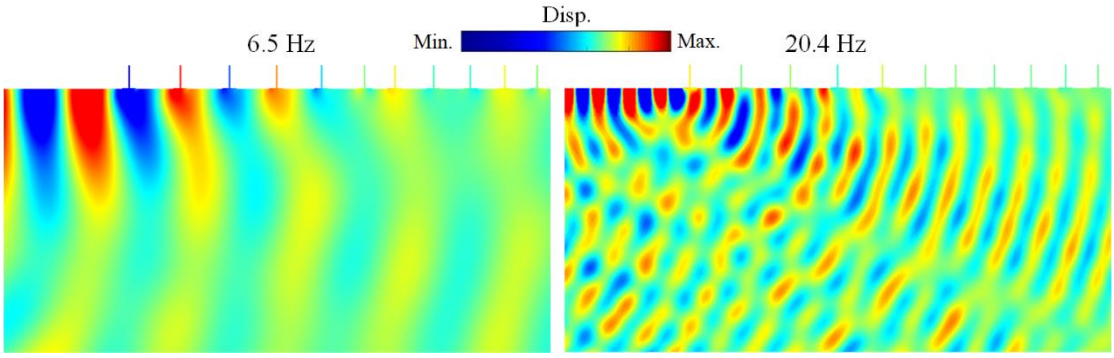

Figure 5-12 The propagations of the Rayleigh waves in the ITSM

Here, a 30 m deep surface layer of the Shanghai coastal plain consisting of a fill layer, a clayey silt layer, two sandy silt layers, a silty clay layer and a silty clay layer is introduced to verify the attenuation effect of the seismic metamaterials designed in this section on seismic surface waves. The various soil layer material parameters and thicknesses are shown in Table 5-3, and the simplified model and transmission spectrum results used to calculate transmission are shown in Figure 5-13. It is found that the inverted T-shaped seismic metamaterial located on a multilayer substrate still attenuates seismic surface waves over a very wide frequency range.

Table 5-3: The parameters of the layered soil substrate[49,216]

Layers	Depth（m）	Density（kg/m^3）	Young's modulus（MPa）	Poisson's ratio
Fill	0-1.6	1830	37	0.4
Clayey silt	1.6-2.5	1939	44	0.4
Sandy silt 1	2.5-9.0	1888	53	0.4
Silt	9.0-15.5	1898	141	0.45
Sandy silt 2	15.5-25.5	1837	90	0.45
Silty clay	25.5-30	1847	155	0.45

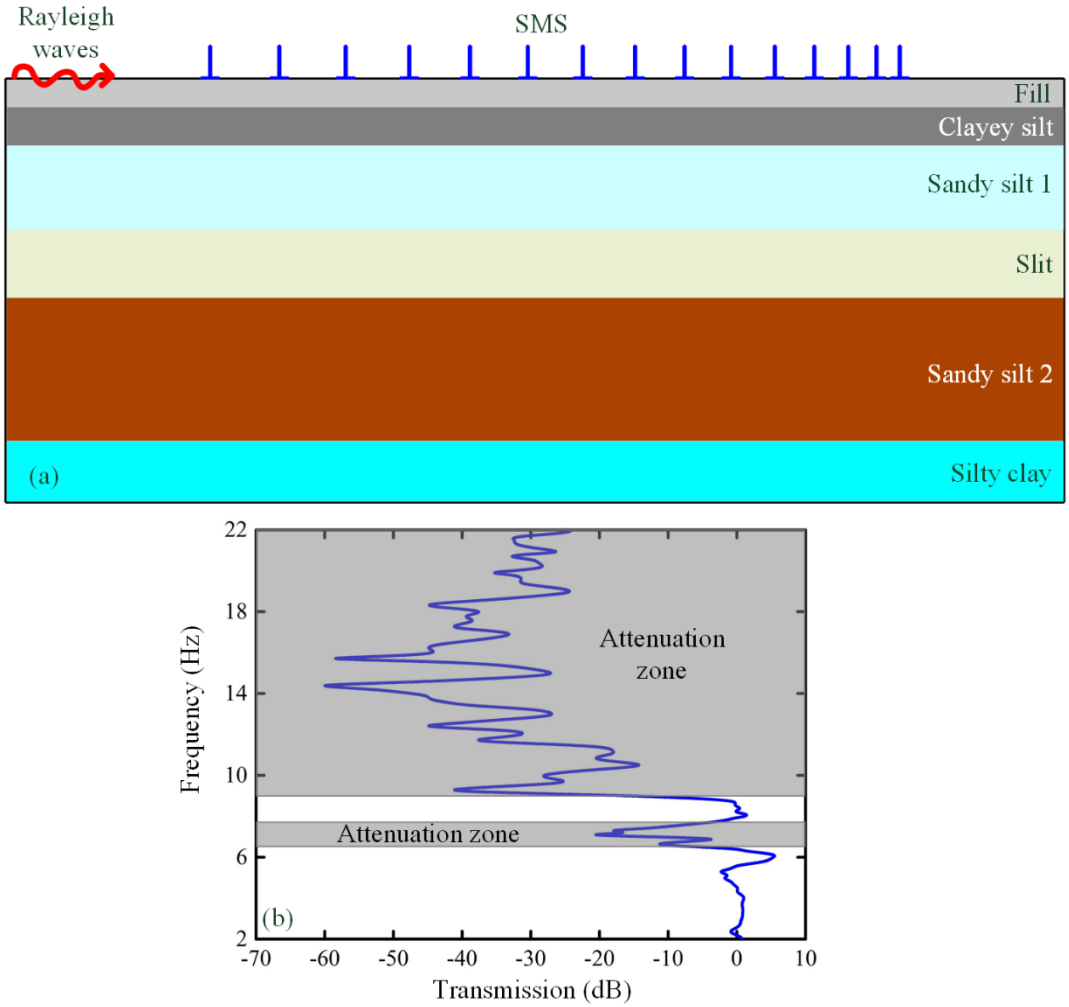

Figure 5-13 The transmissions of surface waves on the ITSM with layered substrate (a) Schematic picture of the finite system. (b) The transmission of Rayleigh waves propagating in the seismic metamaterials

5.4 Conclusion

In summary, the mechanical property of the LFAZ of the elastic metamaterial made of pillars on a substrate has been investigated numerically. We found that the LFAZ is immobile with the changed distances between pillars. The “rainbow trapping effect” in the SAZ has then been demonstrated by numerical simulation and experiments. We have observed that the SAZ becomes wider when suitable distances between pillars are selected. Therefore, for a properly designed elastic metamaterial, there is an opportunity to connect lower bound of the SAZ and the upper bound of the LFAZ. We then can obtain a wide attenuation zone from an ultra-low frequency for surface waves by just using one kind of artificial structures on a substrate. In the case of the seismic Rayleigh

waves, these two characteristics of the LFAZ and the SAZ are used to design a kind of seismic metamaterial by just using one kind of artificial steel structure on a soil substrate. The proposed seismic metamaterial can attenuation the Rayleigh waves from 5 to 22 Hz. Different with the interplay of the local resonance and Bragg bandgaps[48,204], the LFAZ and the SAZ of the SMS hardly interfere with each other and together create a common attenuation zone.

Chapter 6 Design of the inertially amplified lever-type seismic metamaterials with a low-frequency bandgap

Seismic Rayleigh waves at the frequencies below 20 Hz are the greatest threat to the man-made buildings located in the mid and far fields of the seismic source when earthquakes happen. [31,217] Seismic metamaterials (SMs) [31-35,50,52,133,148,160] have been proposed by researchers to isolate the seismic Rayleigh waves before they arrive the critical infrastructures and buildings. This is due to the bandgap characteristics of the SMs composed of the periodic arrangement of artificial unit cells. The seismic waves will be attenuated significantly by the SMs in the frequency range of the bandgap. [41,42,96,113,141,166,218-220] To obtain wider bandgaps, the pillars with different kinds of structures,[49,114,134-137,168] and the "rainbow trapping effects" [35,38,138,152,195,213,214,221] were utilized. However, the ultra-low-frequency (< 2 Hz) bandgaps are hard to obtain by using small-size structures.

Fortunately, the inertial amplification proposed by Yilmaz et al. [183,222,223], which induces low-frequency bandgaps by using a small mass, was utilized to design metamaterials. The lever-type structures were introduced to amplify the motion of the resonate small mass, which in turn effectively reduces the resonance frequency. Based on the similar structures, Li et al. [199] proposed a phononic beam to isolate transverse waves utilizing inertial amplification resonators. A wide bandgap induced by inertial amplification in a continuous elastic rod was obtained and a general 2D realization of the inertially amplified system in a plate was proposed in Ref. [224]. In addition, Acar et al. [225] experimentally and numerically proposed a periodic solid structure which exists wide and deep bandgaps induced by embedded inertial amplification mechanisms. The 3D structures was experimentally demonstrated by using embedded inertial amplification mechanisms, which can isolate elastic waves in a wide frequency range. [226] Recently, a 2D solid structure with embedded inertial amplification mechanisms was designed by using topology optimization to obtain an ultrawide bandgap at low frequencies. [227] However, there is almost no research of the SMs with inertial amplification to achieve the low-frequency bandgaps for surface waves.

In this chapter, we propose a kind of the SM with a low-frequency bandgap induced by inertial amplification to attenuate seismic surface waves. We first experimentally demonstrate the bandgap characteristics of inertial amplification effects

in a metamaterial plate (MMP) sample formed by 5×5 periodic unit cells. The band structure of the simplified model of the MMP is also analytically calculated by using the transfer-matrix method. Then, to achieve the broadband attenuation, two kinds of unit cells with different positions of hinge joints are chosen to construct a new complex metamaterial plate (CMP). Finally, the inertial amplification mechanisms are introduced to design the SMs which are capable of isolating seismic surface waves at low frequencies. It is very known that inertial amplification mechanisms with small mass can achieve strong vibration attenuation at low frequencies, which property the SMs most need. This work demonstrates that the inertial amplification mechanisms can also induce the bandgap for seismic surface waves at ultra-low frequencies even with using the simple structures.

6.1 Models and experimental setup

Figure 6-1(a) illustrates the unit cell of the MMP based on inertial amplification in the experiments and utilized in the simulation calculations. The simplified model of the structure is also given in Fig. 6-1(b). The unit cell is constituted of the lever, the support bar, mass, spring, hinge joint and the base plate. In the MMP, the lattice constant a is 3 cm. The thickness t of the plate is 1 mm. The other geometric parameters of the structure are shown in Fig. 6-1(c). The resonant frequency of the resonator in the model is [222]

$$f = \frac{1}{2\pi}\sqrt{\frac{k}{(\mu-1)^2 m}}\ , \tag{6-1}$$

where $\mu = l_1/\ l_2$ is the lever ratio with l_1 being the length of the lever and l_2 being the distance between the spring and support bar; k is the stiffness of the spring; and m is the mass. The inertial mass will be amplified $(\mu\text{-}1)^2$ times and the resonance frequency will be reduced $(\mu\text{-}1)$ times when the lever is rigid and has no mass. A low resonance frequency f can be achieved in the following cases. First, when the stiffness of the spring k is small, which means the soft material is used. Second, when the lever ratio μ is large, which means the long lever (i.e., l_1 is large) is used or the position of the support bar is near the spring (i.e., l_2 is small). Third, when large mass (i.e., m is large) is used. Therefore, there are a lot of options to design elastic metamaterials with low-frequency bandgaps, including SMs which we will mention later.

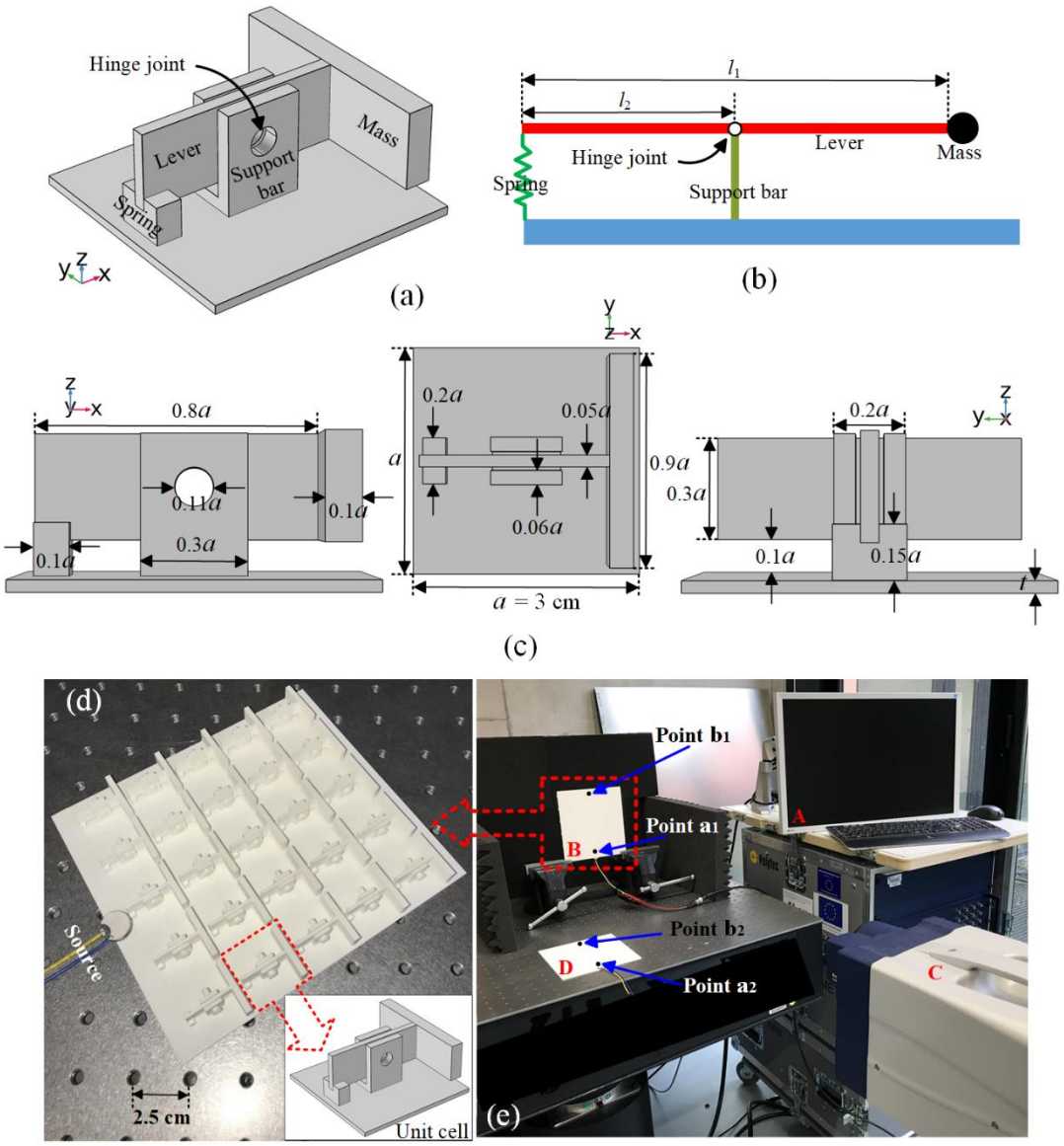

Figure 6-1 The metamaterial plate and experimental setup

(a) The unit cell of the metamaterial plate (MMP) considered in the numerical simulation and experiment. (b) The simplified model of the (a). (c) The geometric parameters of the unit cell. (d) The experimental sample of the MMP and (e) the experimental layout with a computer (Label A), the MMP (Label B), the laser vibrometer (Label C) and the same plate (Label D) as in the MMP

Figure 6-1(d) illustrates the experimental sample of the MMP. The sample is formed by 5×5 periodic unit cells. In this sample, all parts are printed using 3D printer. The PLA rod is fabricated and the lever and the support bar are assembled with PLA rod horizontally installed through the holes to form the hinged part. More enlarged photograph of the hinged part can be found in Figure 6-2. The source vibrating in z direction is excited at one end of the MMP. Figure 6-1(e) shows the experimental layout.

Label A is a computer, which is utilized to set the output signal of the source on sample B and processes the input signal from the laser vibrometer C. In order to obtain clear and perfect propagation effects of flexural waves in the MMP, the laser vibrometer (Polytec PSV-500) is used to measure on the back of the MMP. In addition, a bare plate D, which is the same plate as in the MMP, is also measured to provide the control results.

In order to facilitate the realization of the 3D printing of the MMP, the material of the whole structure is chosen as PLA whose Young's modulus is 3.4398 GPa, density is 1086.3 kg/m^3, and Poisson's ratio is 0.35 in the both simulation and experiment. [212] The connections between the support bar and the base plate, the base plate and the spring, the lever and the mass are perfect continuous. The spring and the lever are perfectly glued together. It is worth noting that the material of the spring part is PLA. Of course, according to the Eq. (6-1), the spring part can be replaced by a softer material to obtain a less k and a lower-frequency bandgap. The connection between the lever and the support bar is hinge joint. The thickness of the lever along z axis is set as $0.3a$ to enhance the bending stiffness of the lever along z axis. At low frequencies, the lever can be regarded as a rigid part to achieve the inertial amplification.

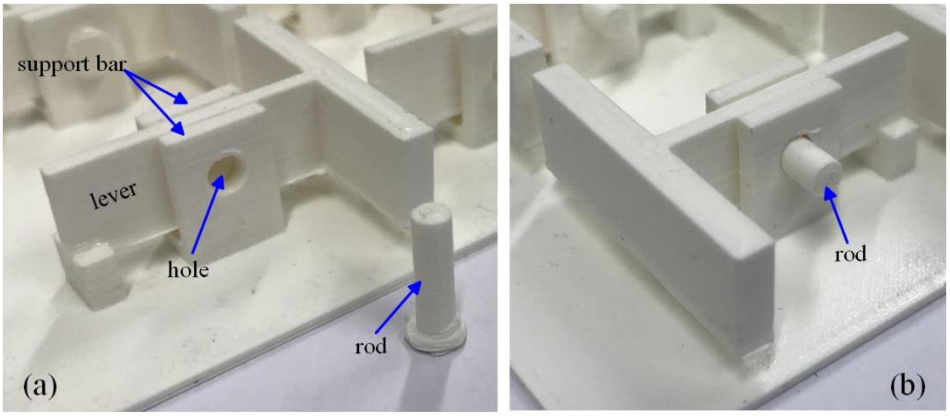

Figure 6-2 The enlarged photograph of the hinged part

(a) The PLA rod, lever and support bar used at hinged part. (b) The assembled hinged part by using lever, the support bar and PLA rod

The simulation results in this work are all calculated by using the multibody dynamics module of COMSOL 5.4. The periodic boundary conditions are set on the plate of the unit cell along x and y directions. It is worth noting that both boundary

similarity and pointwise constraint are utilized to achieve the periodic boundary condition in the multibody dynamics module. The hinge joint between the lever and the support bar shown in Fig. 6-1 is set as hinge-connection condition.

The same structure as the experimental sample shown in Fig. 6-1(d) is used in simulation of the flexural wave propagation in the MMP. The transmission spectrums in the experiments and simulations are all defined as

$$TS = 20 \times \log_{10}(R_1/R_0), \tag{6-2}$$

where R_0 and R_1 are the root mean square (RMS) of the out-of-plane velocities at the two points a_1 (a_2) and b_1 (b_2) shown in Fig. 6-1(d), respectively.

6.2 Analytical solutions of the simplified model

The transfer-matrix method can be used to analytically calculate the band structure of the one-dimensional periodic simplified model. As shown in Fig. 6-3(a), the simplified model used for analytical solution can be assumed as the Euler-Bernoulli beam with inertial amplified resonators. So, the governing equation for the flexural waves in the beam is[203,204]

$$EI\frac{\partial^4 z(x,t)}{\partial x^4} + \rho A\frac{\partial^2 z(x,t)}{\partial t^2} = 0, \tag{6-3}$$

where E, I, ρ and A are Young's modulus, section moment of inertia, density and section area of the beam, respectively. $z(x,t)$ is the out-plane displacement of the beam. The physical quantities of the beam can be expressed in the following forms: [115]

$$z(x,t) = \left(Ae^{-i\lambda x} + Be^{i\lambda x} + Ce^{-\lambda x} + De^{\lambda x}\right)e^{i\omega t}, \tag{6-4}$$

$$\theta(x,t) = y(x,t)', \tag{6-5}$$

$$M(x,t) = EIy(x,t)'', \tag{6-6}$$

$$Q(x,t) = -EIy(x,t)''', \tag{6-7}$$

where A, B, C and D are complex coefficients; $\lambda = \sqrt[4]{\rho A\omega^2/EI}$ with $\omega = 2\pi f$ being the circular frequency is the flexural wavenumber; and θ, M and Q are the slope, bending moment and shear force, respectively.

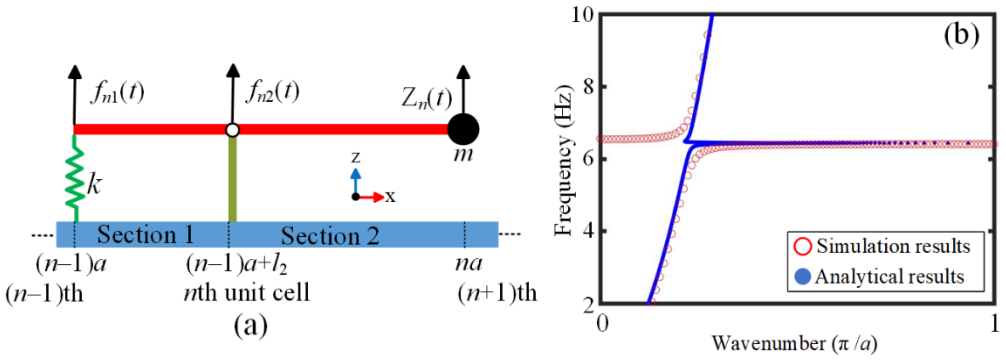

Figure 6-3 The analytical results of the simplified model

(a) The simplified model used for analytical solution. (b) the numerical simulation results (COMSOL) and analytical results of the band structure of the simplified model

In the nth unit cell, the out-plane displacement of section 1 is

$$z_{n,1}(x_1,t) = \left(A_{n,1}e^{-i\lambda x_1} + B_{n,1}e^{i\lambda x_1} + C_{n,1}e^{-\lambda x_1} + D_{n,1}e^{\lambda x_1}\right)e^{i\omega t}, \quad (6\text{-}8)$$

where $x_1 = x-(n-1)a$ and $(n-1)a \le x \le (n-1)a + l_2$. So, from the left side to the right side of section 1 of the nth unit cell, we obtain the transfer matrix in this field by following:

$$\mathbf{\Psi}_{n,1}(0,t) = \mathbf{H}_{1\alpha}\left[A_{n,1}\ B_{n,1}\ C_{n,1}\ D_{n,1}\right]^T e^{i\omega t}, \quad (6\text{-}9)$$

$$\mathbf{\Psi}_{n,1}(l_2,t) = \mathbf{H}_{1\beta}\left[A_{n,1}\ B_{n,1}\ C_{n,1}\ D_{n,1}\right]^T e^{i\omega t}, \quad (6\text{-}10)$$

where $\mathbf{\Psi}(x,t) = [z(x,t)\ \theta(x,t)\ M(x,t)\ Q(x,t)]^T$ is the state vector; and $\left[A_{n,1}\ B_{n,1}\ C_{n,1}\ D_{n,1}\right]^T$ is the coefficient vector. Substituting Eq. (6-10) into Eq. (6-9), we obtain

$$\mathbf{\Psi}_{n,1}(l_2,t) = \mathbf{H}_{1\beta}\mathbf{H}_{1\alpha}^{-1}\mathbf{\Psi}_{n,1}(0,t) \triangleq \mathbf{H}_1\mathbf{\Psi}_{n,1}(0,t), \quad (6\text{-}11)$$

where $\mathbf{H}_1$ is the transfer matrix. It is shown in Appendix of this chapter.

Similarly, the out-plane displacement of section 2 is

$$z_{n,2}(x_2,t) = \left(A_{n,2}e^{-i\lambda x_2} + B_{n,2}e^{i\lambda x_2} + C_{n,2}e^{-\lambda x_2} + D_{n,2}e^{\lambda x_2}\right)e^{i\omega t}, \quad (6\text{-}12)$$

where $x_2 = x-(n-1)a$ and $(n-1)a + l_2 \le x \le na$. So, from the left interface to the right one of section 2 of the nth unit cell, we obtain

$$\mathbf{\Psi}_{n,2}(a,t) = \mathbf{H}_{2\beta}\mathbf{H}_{2\alpha}^{-1}\mathbf{\Psi}_{n,2}(l_2,t) \triangleq \mathbf{H}_2\mathbf{\Psi}_{n,2}(l_2,t), \quad (6\text{-}13)$$

where $\mathbf{H}_2$ is the transfer matrix. It is shown in Appendix of this chapter.

As for the *n*th lever-type structure on the beam, the dynamic equilibrium equation is

$$f_{n1}(t) + f_{n2}(t) + m\ddot{Z}_n(t) = 0, \tag{6-14A}$$

$$l_2 f_{n1}(t) + (l_1 - l_2)m\ddot{Z}_n(t) = 0, \tag{6-14B}$$

where $Z_n(t)$ is the displacement of the *n*th mass of the lever-type structure; and $f_{n1}(t)$ and $f_{n2}(t)$ are the forces of the spring and support bar on the lever, respectively. Due to the Hooke's Law, we obtain

$$f_{n1}(t) = k\left[\frac{Z_n(t)}{\mu-1} + z_{n,1}(0,t) - z_{n,2}(l_2,t)\right], \tag{6-15}$$

where k is the spring stiffness; and $\mu = l_1/\ l_2$ is lever ratio. Substituting Eq. (6-15) into Eq. (6-14), we obtain

$$f_{n1}(t) = \frac{km\omega^2(\mu-1)^2}{m\omega^2(\mu-1)^2-k}[z_{n,1}(0,t) - z_{n,2}(l_2,t)] \triangleq G_1[z_{n,1}(0,t) - z_{n,2}(l_2,t)], \tag{6-16}$$

$$f_{n2}(t) = \frac{km\omega^2(-\mu^2+3\mu-2)}{m\omega^2(\mu-1)^2-k}[z_{n,1}(0,t) - z_{n,2}(l_2,t)] \triangleq G_2[z_{n,1}(0,t) - z_{n,2}(l_2,t)]. \tag{6-17}$$

Due to the continuities at the interface between $(n-1)$th and *n*th unit cells, we obtain

$$z_{n-1,2}(a,t) = z_{n,1}(0,t), \tag{6-18A}$$

$$\theta_{n-1,2}(a,t) = \theta_{n,1}(0,t), \tag{6-18B}$$

$$M_{n-1,2}(a,t) = M_{n,1}(0,t), \tag{6-18C}$$

$$Q_{n-1,2}(a,t) = Q_{n,1}(0,t) - f_{n1}(t). \tag{6-18D}$$

Substituting Eq. (6-16) into Eq. (6-18), we obtain

$$\mathbf{\Psi}_{n-1,2}(a,t) = \mathbf{H}_3\mathbf{\Psi}_{n,1}(0,t) + \mathbf{H}_4\mathbf{\Psi}_{n,2}(l_2,t), \tag{6-19}$$

where $\mathbf{H}_3$ and $\mathbf{H}_4$ are shown in Appendix of this chapter. Due to the continuities at the interface between sections 1 and 2 of the *n*th unit cell, we obtain

$$z_{n,1}(l_2,t) = z_{n,2}(l_2,t), \tag{6-20A}$$

$$\theta_{n,1}(l_2,t) = \theta_{n,2}(l_2,t), \tag{6-20B}$$

$$M_{n,1}(l_2,t) = M_{n,2}(l_2,t), \tag{6-20C}$$

$$Q_{n,1}(l_2,t) = Q_{n,2}(l_2,t) - f_{n2}(t). \tag{6-20D}$$

Substituting Eq. (17) into Eq. (20), we obtain

$$\mathbf{\Psi}_{n,1}(l_2,t) = \mathbf{H}_5\mathbf{\Psi}_{n,2}(l_2,t) + \mathbf{H}_6\mathbf{\Psi}_{n,2}(0,t), \tag{6-21}$$

where $\mathbf{H}_5$ and $\mathbf{H}_6$ are shown in Appendix of this chapter. Substituting Eqs. (6-11), (6-13), (6-19) and (6-21), the transfer equation of the flexural waves from the right interface of the $(n-1)$th unit cell to the right interface of the nth unit cell is obtain

$$\mathbf{\Psi}_{n,2}(a,t) = \mathbf{T}_{unit}\mathbf{\Psi}_{n-1,2}(a,t), \tag{6-22}$$

where $\mathbf{T}_{unit} = \{\mathbf{H}_3\mathbf{H}_1^{-1}[(\mathbf{I}_\mathrm{A} - \mathbf{H}_6\mathbf{H}_1^{-1})^{-1}\mathbf{H}_5\mathbf{H}_2^{-1}] + \mathbf{H}_4\mathbf{H}_2^{-1}\}^{-1}$ is the transfer matrix in which $\mathbf{I}_\mathrm{A}$ is a 4×4 identity matrix.

Considering the Bloch-Floquet theory, we obtain

$$\mathbf{\Psi}_{n,2}(a,t) = e^{iqa}\mathbf{\Psi}_{n-1,2}(a,t), \tag{6-23}$$

where q is the wavenumber. Substituting Eq. (6-23) into Eq. (6-22), we obtain

$$\left|\mathbf{T}_{unit} - e^{iqa}\mathbf{I}_\mathrm{A}\right| = 0. \tag{6-24}$$

By solving the eigenvalue equation, the band structure can be obtained.

For instance, Fig. 6-3(b) shows the simulated results and analytical results of the band structure of the simplified model, when the lattice constant is a = 1 m; the height, breadth, sectional area, section moment of inertia, Young's modulus and density of the beam is h = 0.05 m, b = 1 m, $A = bh$, $I = bh^3/12$, 207 GPa and 7784 kg/m^3, respectively; l_1 = 0.9 m, l_2 = 0.3 m; m = 15.2838 kg and k = 100,000 N/m. It is worth noting that the support bar and the lever are rigid. The simulation results are calculated by COMSOL 5.4 (Multibody Dynamics Module) to evaluate the accuracy of the analytical solution. The simulated results are almost in agreement with the analytical results, especially for the position of the bandgap. It is worth noting that the frequencies of the two bandgaps are consistent with the predicted result from Eq. (6-1). The effective inertial mass is 4m due to the $\mu = l_1/l_2 = 3$. Obviously, the frequency of the bandgap can be controlled easily in this model by changing one or more parameters of the structure. For instance, an ultra-low frequency bandgap can be achieved when the mass m or lever ratio μ is larger, or when the spring stiffness k is smaller than the example shown in Fig. 6-3.

6.3 Results and Discussions of the MMPs

6.3.1 Band structures

Figure 6-4 shows the band structure of the MMP and the transmission of the flexural waves in the MMP and the bare plate along the ΓX direction (i.e. *x* direction). In Fig. 6-4(a), the out-of-plane polarization in the band structure of the MMP is given. The parameter of the out-of-plane polarization ξ is defined as

$$\xi = \int_S |w|^2 ds \,/\, \int_S (|u|^2 + |v|^2 + |w|^2) dS, \tag{6-25}$$

where *u*, *v* and *w* are the displacement components in the three directions (*x*, *y* and *z*); and *S* is the whole unit cell. A wide bandgap for the flexural waves can be found from 385 to 1200 Hz. It is worth noting that, the end parts of the second and third dispersion curves have high out-of-plane polarization value. However, these two bands almost do not affect the wide bandgap in Fig. 6-4(a). We can easily find these two bands are almost flat, especially when out-of-plane polarization value is large. It means it is just the local resonance at a single frequency, which can be ignored when we determine the bandgap. The vibration modes at these two bands are illustrated in Fig. 6-5. At second band, shown in Fig. 6-5(a), the mass is rotating resonance in *xy* plane. At third band, shown in Fig. 6-5(b), the mass is rotating resonance in *yz* plane. It is worth noting that these two kinds of local resonances are hard to be excited by flexural waves. It also demonstrates why there is no sign of these two bands in the simulated and experimental transmission results.

As shown in Fig. 6-4(b), there is a significant AZ at these frequencies in the simulated and experimental results. Compared with the simulated results, the attenuation effects in the experimental results are not particularly obvious at low frequencies in the bandgap. In addition, in the whole bandgap, the attenuation effects in the experimental results are weaker than those in the simulated results. This is due to the fact that the hinge joint in the experiments is not completely perfect like how it is considered in the simulation. In the experiments, the friction and backlash in the hinged part are difficult to eliminate. Instead, in the simulations, all boundaries in the hinge joint are rigid and smooth. However, it is easy to find that the MMP in the experiments can obviously attenuate the flexural waves in the bandgap compared with the bare plate.

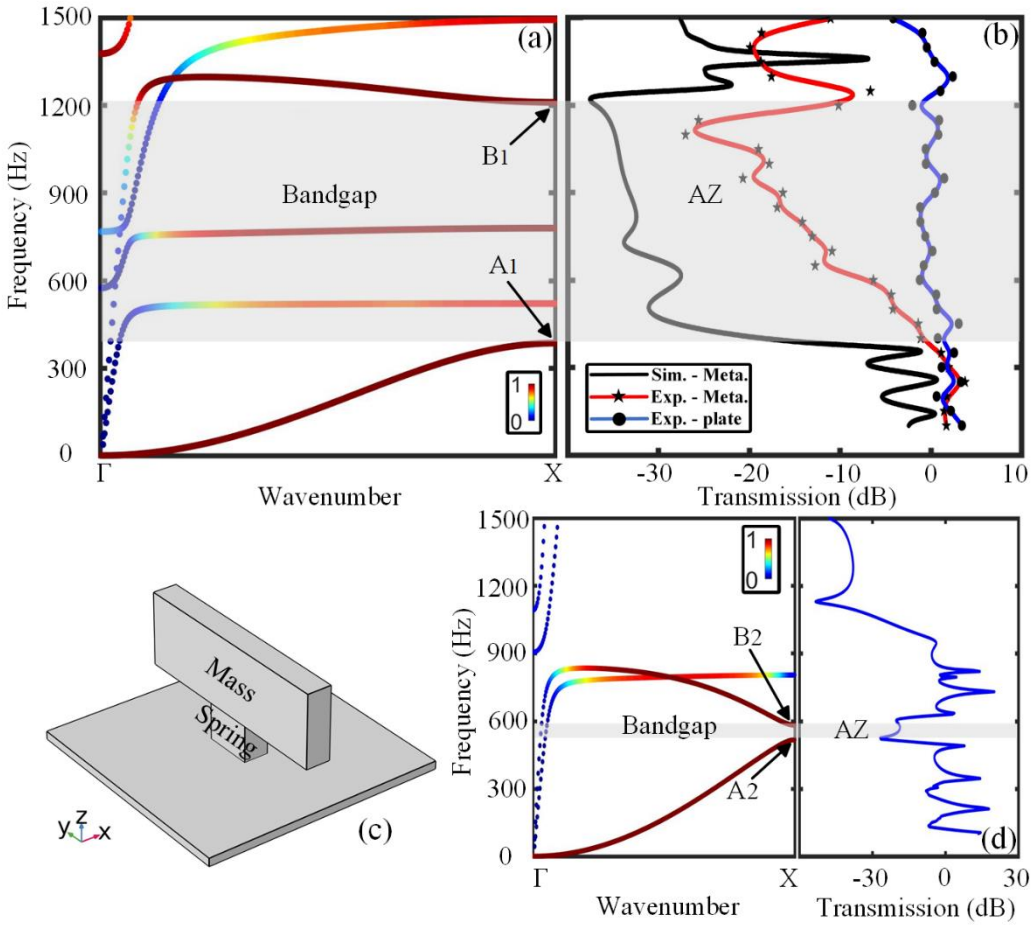

Figure 6-4 The band structure and transmission

(a) The band structure of the MMP along the ΓX direction. (b) The transmissions of the flexural waves in the MMPs and the bare plate along the ΓX direction. (c) The unit cell consisted of the same plate, spring and mass as in MMP. (d) The band structure and transmission of the metamaterial constituted of periodic (c)

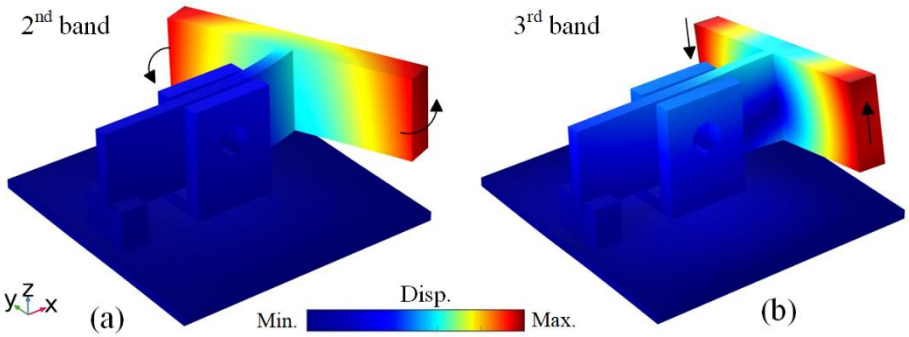

Figure 6-5 The vibration modes at 2nd and 3rd bands

The vibration modes at (a) 2nd and (b) 3rd bands in Fig. 6-3(a)

For a better comparison, as shown in Fig. 6-4(c), a periodic structure composed of the same plate, springs and masses as in the MMP is considered. In the band structure and the transmission of the metamaterial, the first bandgap and AZ is very narrow and its lowest frequency is around 520 Hz in Fig. 6-4(d). In Fig. 6-3, the lever ratio μ of the proposed unit cell is about 2, so the bandgap range of the inertial amplification mechanism is similar to the that of the spring-mass structure in Fig. 6-4(c). When the position of the support bar is near the spring, which means the l_2 becomes smaller and μ becomes larger, the bandgap range significantly reduces.

6.3.2 **Vibration modes**

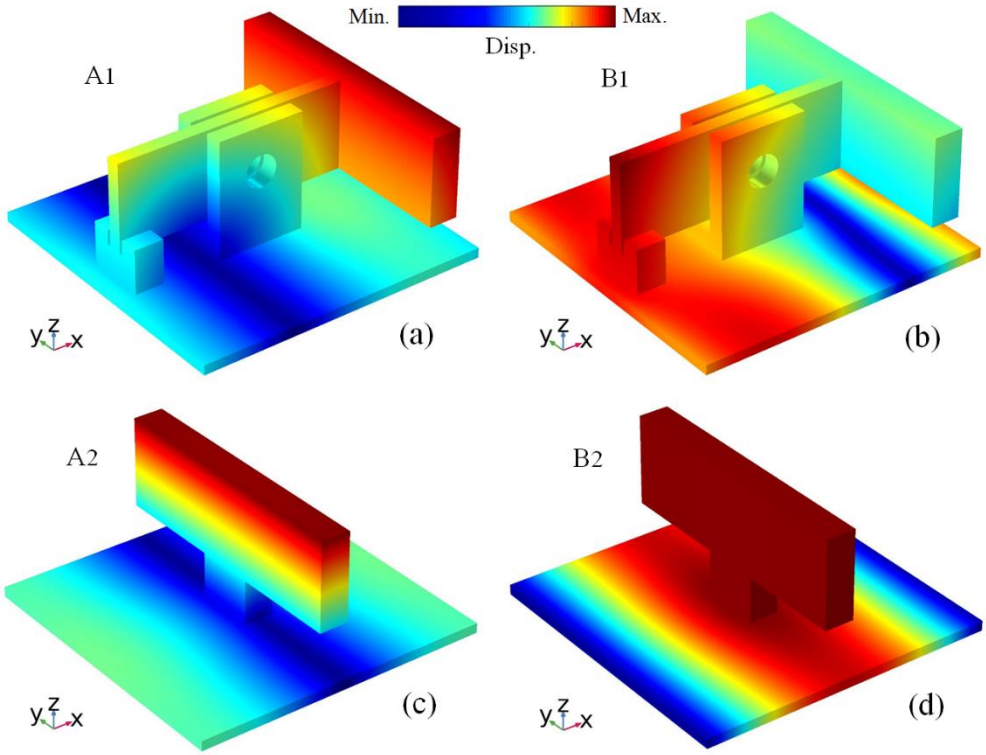

Figure 6-6 Vibration modes of the metamaterial plates

Vibration modes corresponding to points (a) A_1, (b) B_1, (c) A_2 and (d) B_2 marked in 6-4(d). The color bar represents the degree of displacement

The vibration modes at the marked points in the band structures are illustrated in Fig. 6-6. Points A_1 (A_2) and B_1 (B_2) are the two boundaries of the bandgaps shown in Figs. 6-4(a - d). Figure 6-6(a) shows the strong resonance of the mass at point A_1. At point B_1, most of the displacement is around the spring part shown in Fig. 6-6(b). It is clear that the large bandgap is due to the inertial amplification system and the strong

resonance of the mass. In Fig. 6-6(c), most of the displacement is only at the top of the mass, which increases the frequency of the bottom boundary of the first bandgap. In addition, the strong resonance of the mass shown in Fig. 6-6(d) reduces the frequency of the top boundary of the first bandgap. Therefore, in Fig. 6-4(d), the frequency of the first bandgap is higher and the width of the first bandgap is narrower than that in Fig. 6-4(a).

6.3.3 **Transmission**

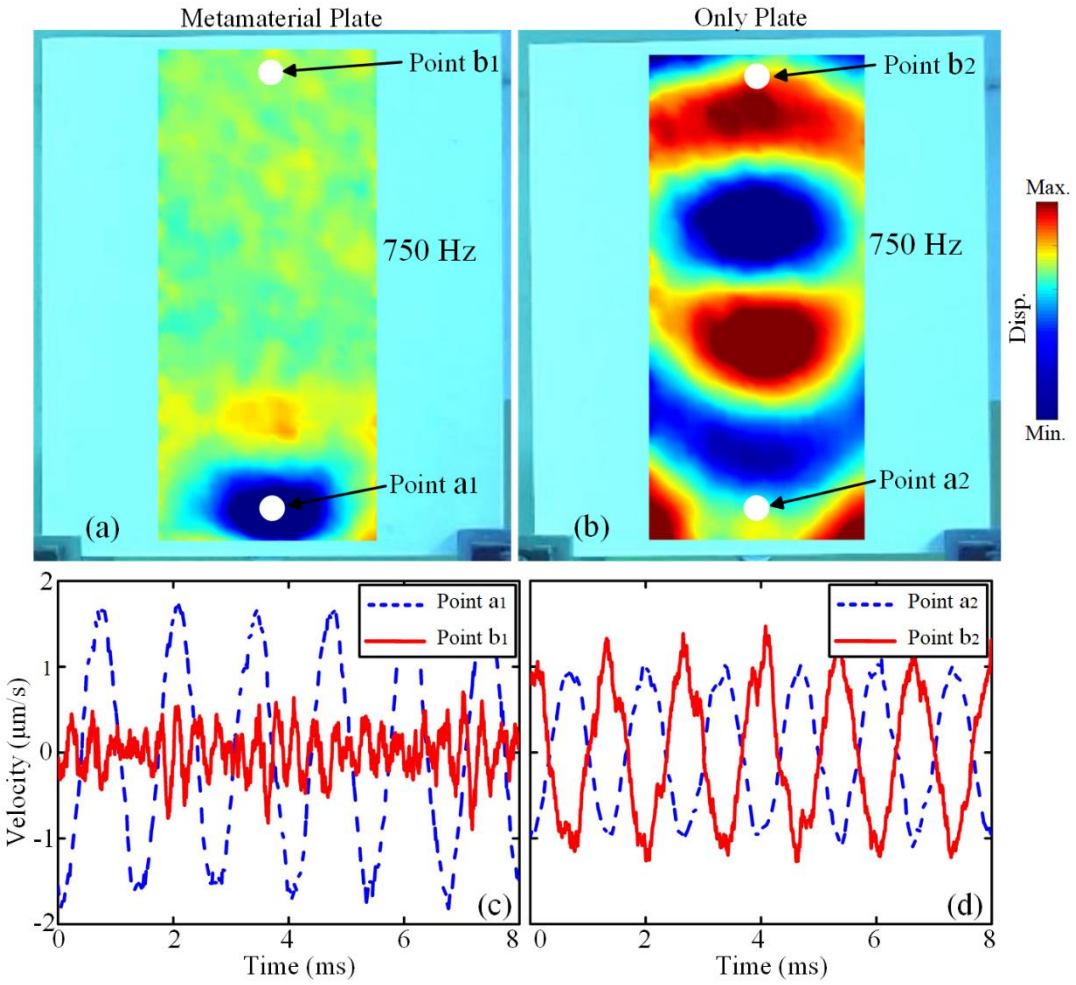

Figure 6-7 The propagations of the flexural waves

Experimentally measured flexural waves on the back sides of (a) the MMP and (b) the bare plate at 750 Hz. The color indicates the velocity field on the samples. (c) and (d) show the Time-Velocity curves for points a_1, b_1, a_2 and b_2 marked in (a) and (b)

The velocity fields of the flexural waves on the back side of the MMP and bare

plate are experimentally measured. At 750 Hz, for instance, the results are shown in Figs. 6-7(a - b). It is easy to distinguish the attenuation and propagation of the flexural waves in the MMP and bare plate, respectively. In addition, the time-velocity curves for points a_1 and a_2 near the source and points b_1 and b_2 far away from the source are illustrated in Figs. 6-7(c - d). Comparing with the vibrations at points a_1 and b_1, we can find that the flexural waves are strongly attenuated in the MMP. Because there is no damping at the boundaries of the plate, the reflected waves can be found from Fig. 6-7(d). Therefore, the velocity of point b_2 is larger than that of point a_2. The results also demonstrate the strong attenuation ability of the MMP.

6.4 Results and Discussions of the SMs

6.4.1 **Model and band structure**

In this section, the similar structure with inertial amplification is utilized on a soil half-space to induce low-frequency bandgap for surface waves. As we know, the artificial structure on a plate, such as the MMP, has an excellent effect in attenuating flexural waves (out-of-plane vibration). The SMs' target is attenuation of surface waves (*xz*-plane vibration) on a half-space. Due to the huge difference between flexural waves and surface waves, the artificial structure in the MMPs that can be used to attenuate flexural waves are not necessarily suitable for a half-space to attenuate surface waves. However, some artificial structures in the MMPs can play a key role in a half-space. For instance, drilling holes periodically in a half-space [40], or burying pillars periodically in a half-space [33,34], or erecting pillars periodically on a half-space [137,228] all can generate bandgaps for surface waves. Moreover, some artificial structures of the MMPs covering a half-space can exert unexpected effects for surface waves. For instance, two-component [53,160] and three-component [52] MMPs on a half space can achieve ultra-low-frequency bandgaps for surface waves. Therefore, due to the excellent performance of the lever-type structure on the plate as shown above, we introduce it into the soil half-space to target seismic surface waves. Similar as the lever-type structure shown in Fig. 6-1, the unit cell of the SM shown in Fig. 6-8(a) is constituted of the lever, support bar, mass, spring, hinge joint and soil substrate.

Comparing with the lattice constant in Fig. 6-1, the lattice constant *a* in Fig. 6-8(a) is scaled to 1.5 m. The relationship between other geometric parameters and lattice constant *a* is consistent with those in Fig. 6-1. Theoretically, the depth of the half-space

should be infinitely deep. In order to facilitate simulation calculations and obtain relatively accurate convergence results, the depth of the soil substrate is selected as $H = 500a$ [114,195]. A part of the spring is replaced by a thin rubber layer with thickness of t_1 to achieve bandgaps at lower frequencies. In addition, the SM is supposed to be constructed by the ordinary building materials, for instance, steel (mass), rubber (spring) and aluminum (support bar and lever). The material properties [34] are shown in Table 6-1.

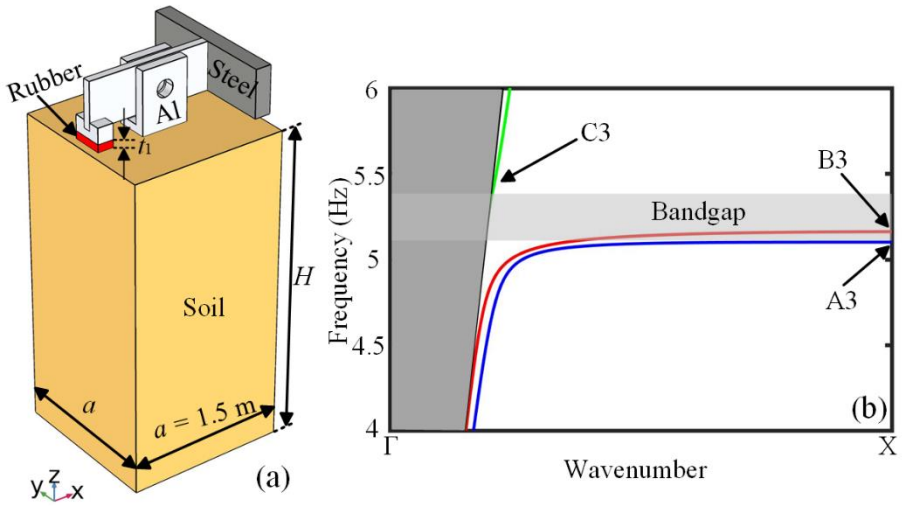

Figure 6-8 The unit cell and band structure

(a) The unit cell of the SM for surface waves. (b) The band structure of the SM for surface waves along the ΓX direction in the range from 4 Hz to 6 Hz

Figure 6-8(b) shows the band structure of the SM along the ΓX direction when the thickness of the rubber is $0.02a$. The area outside the dark gray area is the sound cone. Three bands can be found under the sound cone, which are illustrated by the blue, red and green lines. A bandgap which is marked by the light gray area is shown in the frequency range from 4 Hz to 6 Hz.

6.4.2 **Vibration modes**

Figure 6-9 illustrates the vibration modes of the three points, A_3, B_3 and C_3, marked in Fig. 6-8(b). The central sections of these vibration modes along the *xz* plane are also provided to clearly show the effects of the inertial amplification and the characteristics of the bandgap. The arrows in Figs. 6-9(b), (d) and (f) indicate the displacement

eigenvector; and the length and direction of the arrow indicate the magnitude and trend of the particle movement, respectively.

Figures 6-9(a - b) show that the vibration mainly appears at the two ends of the lever which rotates around the hinge joint in the *xz* plane. This implies that the bandgap for surface waves is induced by the inertial amplification. The vibration modes illustrated in Figs. 6-9(c - d) show that there is almost no vibration in the *xz* plane. Therefore, Rayleigh waves cannot appear in the frequency range of the second band [134]. However, in the range of the third band, Rayleigh waves appear again with the particles mainly moving along *x* direction, see Figs. 6-9(e - f). So, the bandgap region shown in Fig. 6-8(b) for the Rayleigh waves is between the first and third bands [134].

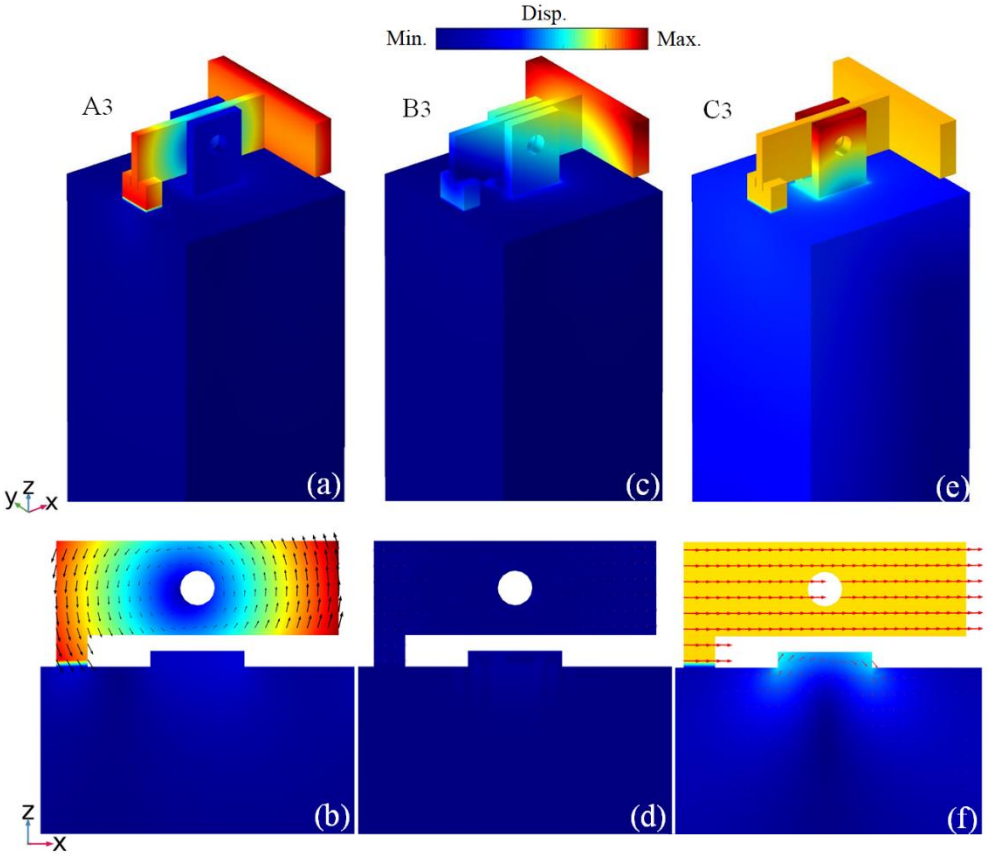

Figure 6-9 Vibration modes of the seismic metamaterial

Vibration modes and their central section along the *xz* plane of the SM for surface waves corresponding to points (a-b) A_3, (c-d) B_3 and (e-f) C_3 marked in Fig. 6-8(b). The arrows in (b), (d) and (f) indicate the displacement eigenvector; and its length and direction indicate the magnitude and trend of the particle movement, respectively. The color bar represents the degree of the displacement

It is known that seismic metamaterials with small mass can hardly achieve bandgaps below 10 Hz. However, the inertial amplification mechanisms with small mass can easily induce low-frequency bandgap, even for surface waves. As the first time of introducing inertial amplification mechanisms into seismic metamaterials, our goal is the existence of this bandgap rather than the enormous width of the bandgap. Therefore, we believe that narrow bandgap in this work is acceptable.

6.4.3 **Effects of the parameters**

The effects of the hinge joint's position, the rubber layer's thicknesses and the Young's modulus of the rubber on the bandgaps are illustrated in Fig. 6-10. The frequencies of the bandgap reduce significantly when the hinge joint moves from right to left along x direction. When the hinge joint moves from right to left, the μ increases and the f in Eq. (6-1) decreases. In addition, the frequencies of the bandgap reduce quickly when the rubber is provided, and keep decreasing when the thickness of the rubber increases. However, the relative bandwidth of the bandgap decreases with the frequency. The frequencies and the relative bandwidth of the bandgaps all increase when the Young's modulus of the rubber increases from 50k to 350 kPa. When the thickness of the rubber decreases or the Young's modulus of the rubber increases, the translational stiffness k in the vertical direction increases [149] and the f in Eq. (6-1) decreases.

Table 6-1 The material parameters used in this chapter

Material	Density (kg/m^3)	Young's modulus (Pa)	Poisson's ratio
Steel	7784	2.07×10^{11}	0.3
Al	2700	7×10^{10}	0.33
Rubber	1300	1.2×10^{5}	0.47
Soil	1800	2×10^{7}	0.3

Comparing with the bandgaps in Fig. 6-4(a), the bandgaps in Fig. 6-10 or Fig. 6-8 (b) are narrow. This is an inevitable result. In Fig. 6-4(a), it is the flexural waves (vibration only along the z axis) that the metamaterials attenuate in a wide frequency range. In Fig. 6-10 and Fig. 6-8(b), it is the Rayleigh surface waves, which include both

longitudinal (x axis) and transverse (z axis) motions, that the SMs are designed to attenuate at ultra-low frequencies. These two kinds of bandgaps cannot be directly compared. In addition, at ultra-low frequencies, the bandgap induced by inertial amplification is quite narrow, as shown in Fig. 6-2. Suitable unit cells can be selected from Fig. 6-10 to construct a new seismic metamaterial to isolate seismic waves in a wide frequency range.

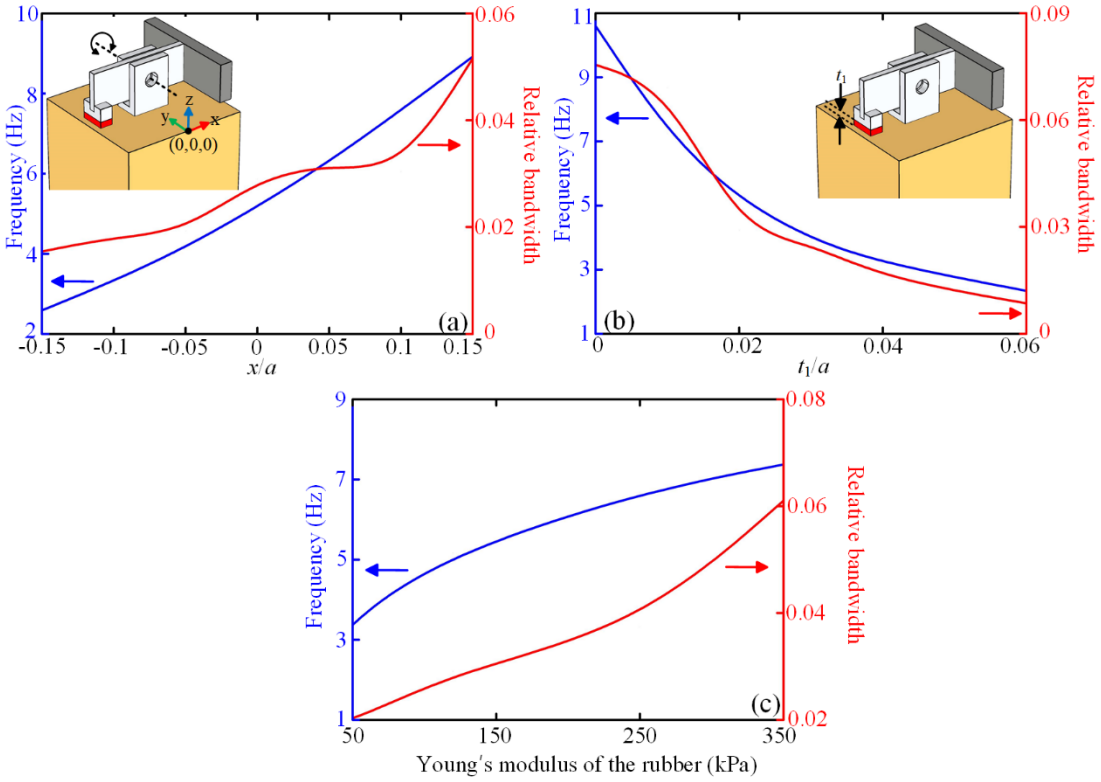

Figure 6-10 Effects of parameters on the first bandgap

Effects of the hinge joint's position along x direction (a), the rubber layer's thickness (b) and the Young's modulus of the rubber (c) on the bandgaps. The blue and red solid lines are the center frequencies and relative bandwidth of the bandgaps, respectively

6.5 Conclusion

An alternative type of seismic metamaterial based on inertial amplification mechanism is presented in this work to open bandgaps for seismic surface waves at low frequency regime. A conceived metamaterial plate with lever-type structures has been experimentally investigated and discussed. It is shown that a wide bandgap for flexural waves appears in a low-frequency region. The propagation analysis measured on the

back side of the MMP has demonstrated that the lever-type structures strongly attenuate the flexural waves. Finally, the similar lever-type structures are introduced into a soil half-space to obtain the bandgaps induced by inertial amplification for seismic surface waves in a low-frequency range. The significant advantage is that inertial amplification mechanisms with small mass can achieve strong vibration attenuation at low frequencies, a property that should be realized for seismic metamaterials. Comparing with the seismic metamaterials proposed in the literature, the width of the bandgap here is not remarkable. However, since it is the first time the inertial amplification mechanism is introduced and considered in seismic metamaterials, our goal is the creation of this bandgap rather than obtaining a large width of the bandgap. Therefore, the narrow bandgap in this work is acceptable. This work provides an alternative way to control seismic surface waves at low frequencies by using a small mass. In addition, the embedded inertial amplification mechanisms have great potential to be used to attenuate seismic surface waves in a wide range at ultra-low frequencies which will be the focus of future researches.

6.6 Appendix: The matrixes used in the analytical calculation

All the matrixes in the analytical calculation of the band structure of the simplified model are shown below:

$$\mathbf{H}_{1\alpha}=\begin{bmatrix} 1 & 1 & 1 & 1 \\ -i\lambda & i\lambda & -\lambda & \lambda \\ -EI\lambda^2 & EI\lambda^2 & EI\lambda^2 & EI\lambda^2 \\ -iEI\lambda^3 & iEI\lambda^3 & EI\lambda^3 & -EI\lambda^3 \end{bmatrix},$$

$$\mathbf{H}_{1\beta}=\begin{bmatrix} e^{-i\lambda l_2} & e^{i\lambda l_2} & e^{-\lambda l_2} & e^{\lambda l_2} \\ -i\lambda e^{-i\lambda l_2} & i\lambda e^{i\lambda l_2} & -\lambda e^{-\lambda l_2} & \lambda e^{\lambda l_2} \\ -EI\lambda^2 e^{-i\lambda l_2} & -EI\lambda^2 e^{i\lambda l_2} & EI\lambda^2 e^{-\lambda l_2} & EI\lambda^2 e^{\lambda l_2} \\ -iEI\lambda^3 e^{-i\lambda l_2} & iEI\lambda^3 e^{i\lambda l_2} & EI\lambda^3 e^{-\lambda l_2} & -EI\lambda^3 e^{\lambda l_2} \end{bmatrix},$$

$$\mathbf{H}_1=\mathbf{H}_{1\beta}\mathbf{H}_{1\alpha}^{-1},$$

$$\mathbf{H}_{2\alpha}=\mathbf{H}_{1\beta},$$

$$\mathbf{H}_{2\beta}=\begin{bmatrix} e^{-i\lambda a} & e^{i\lambda a} & e^{-\lambda a} & e^{\lambda a} \\ -i\lambda e^{-i\lambda a} & i\lambda e^{i\lambda a} & -\lambda e^{-\lambda a} & \lambda e^{\lambda a} \\ -EI\lambda^2 e^{-i\lambda a} & -EI\lambda^2 e^{i\lambda a} & EI\lambda^2 e^{-\lambda a} & EI\lambda^2 e^{\lambda a} \\ -iEI\lambda^3 e^{-i\lambda a} & iEI\lambda^3 e^{i\lambda a} & EI\lambda^3 e^{-\lambda a} & -EI\lambda^3 e^{\lambda a} \end{bmatrix},$$

$$\mathbf{H}_2 = \mathbf{H}_{2\beta}\mathbf{H}_{2\alpha}^{-1},$$

$$\mathbf{H}_3 = \begin{bmatrix} 1 & 0 & 0 & 0 \\ 0 & 1 & 0 & 0 \\ 0 & 0 & 1 & 0 \\ -G_1 & 0 & 0 & 1 \end{bmatrix},$$

$$\mathbf{H}_4 = \begin{bmatrix} 0 & 0 & 0 & 0 \\ 0 & 0 & 0 & 0 \\ 0 & 0 & 0 & 0 \\ G_1 & 0 & 0 & 0 \end{bmatrix},$$

$$\mathbf{H}_5 = \begin{bmatrix} 1 & 0 & 0 & 0 \\ 0 & 1 & 0 & 0 \\ 0 & 0 & 1 & 0 \\ G_2 & 0 & 0 & 1 \end{bmatrix},$$

$$\mathbf{H}_6 = \begin{bmatrix} 0 & 0 & 0 & 0 \\ 0 & 0 & 0 & 0 \\ 0 & 0 & 0 & 0 \\ -G_2 & 0 & 0 & 0 \end{bmatrix}.$$

Chapter 7 Design of enhanced inertial amplification seismic metamaterials with a low frequency bandgap

Inertial amplification mechanism,[183,223] which can achieve low-frequencies resonance just by using a small mass, has been introduced to design elastic metamaterials to obtain low-frequencies bandgaps. The embedded amplification mechanism was proposed by Yilmaz et al.[183,223] to amplify the effective inertia of the wave propagation medium. Frandsen et al.[224] introduced the similar structures into a continuous elastic rod to obtain wide bandgap induced by inertial amplification. The three-dimensional metamaterials based on embedded inertial amplification mechanism have been realized. It has been experimentally demonstrated that they are capable of isolating elastic waves in a wide frequency range.[226] Then, Yuksel et al.[227] have designed a two-dimensional solid structure with embedded inertial amplification mechanisms by using topology optimization to achieve an ultrawide stop band at low frequency. However, the embedded inertial amplification mechanisms have not been introduced into a half space to isolate surface waves.

In this chapter, we propose a unique kind of SM with an ultra-low-frequency bandgap for seismic surface waves by using embedded inertial amplification mechanisms. At first, we design a kind of one-dimensional inertially amplified metamaterial (IAM). The unit cell of the IAM is composed of one base beam, two arms and three hinge joints. The characteristics of the bandgap induced by inertial amplification in the IAM is investigated by using experiments and simulations. Finally, the embedded inertial amplification mechanism is introduced to design the SMs for surface waves at ultra-low frequencies.

7.1 Models of the inertially amplified metamaterial

7.1.1 Models

Three different samples are illustrated in Fig. 7-1(a). The geometric parameter of the bare beam is 180 mm × 30 mm × 1 mm. The traditional metamaterial (TM) has three more rectangles than the bare beam. The geometric parameter of the rectangle is 49 mm × 9.8 mm × 6 mm. The inertially amplified metamaterial (IAM) has three more inertial amplification mechanisms than the bare beam. The lattice constant of the TM

and IAM are all 55 mm. All the samples are fabricated by 3D printer based on polylactic acid (PLA). The material parameters of the PLA are shown in Table 7-1.[212,229] Figure 7-1(b) illustrates the schematic diagram of the experimental setup. The computer outputs the source signal to the piezoelectric patches fixed at the end of the sample. The out-of-plane accelerations at points a and b are measured by the laser vibrometer (Polytec PSV-500). The collected data is input back to the computer and is processed. It is noted that the position of the points a and b are all at the back of the samples.[229]

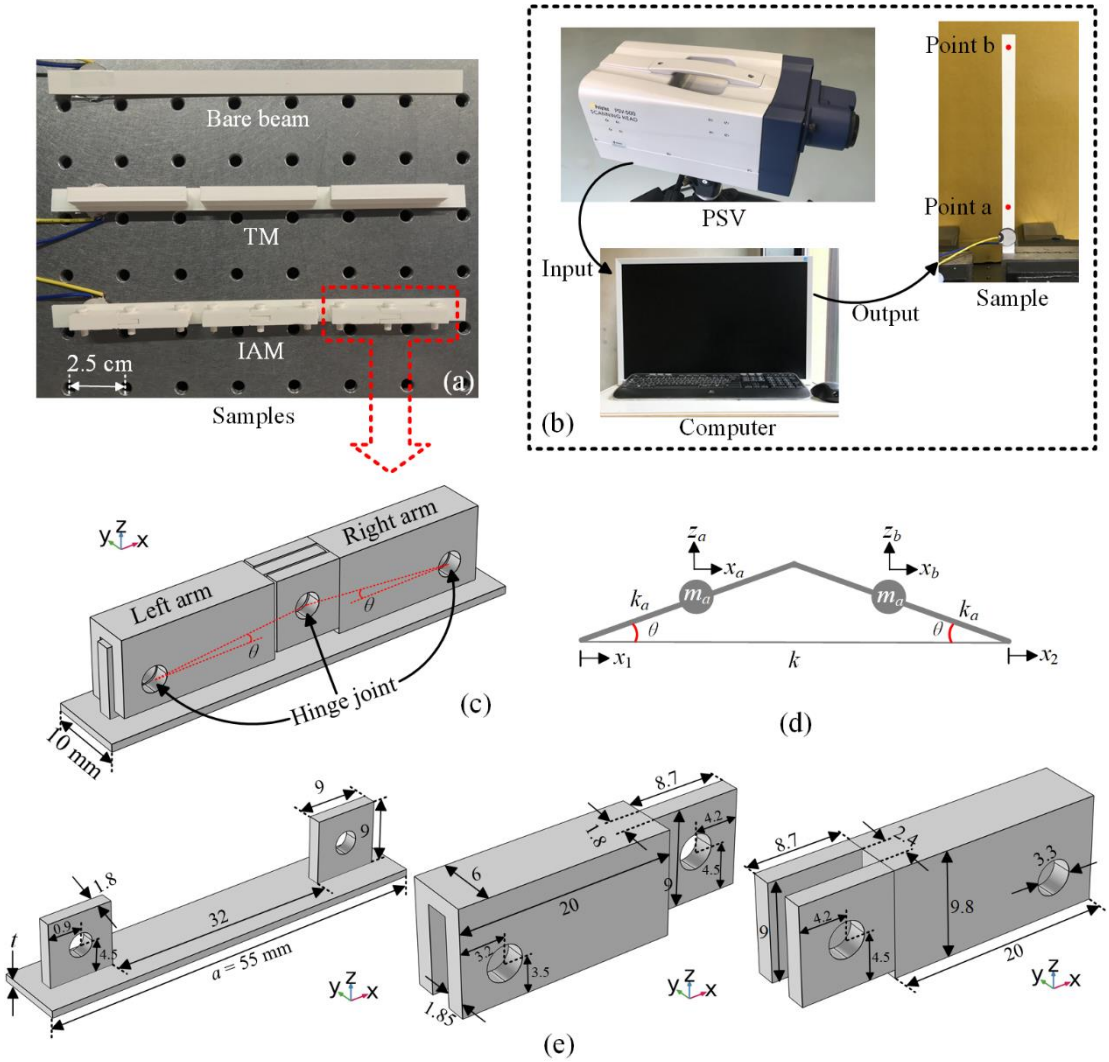

Figure 7-1 The metamaterials and experimental setup

(a) The samples used in the experiments (TM: traditional metamaterial; IAM: inertially amplified metamaterial). (b) Schematic diagram of the experimental setup including laser vibrometer (PSV), the computer and the sample. Points a and b are two data collection points. (c) The unit cell of the IAM. (d) The simplified model of the inertially amplified mechanism in the unit cell and (e) the geometric parameters of the unit cell of the IAM

Figure 7-1(c) illustrates the unit cell of the IAM considered in the numerical simulations and experiments. The unit cell includes one base beam, two arms and three hinge joints. The thickness t of the beam is 1 mm. The angle θ, which determines the magnitude of the amplification generated by the inertially amplified mechanisms, in this work is set at 5°. It is worth noting that hinge joint is not the necessary part for inertial amplification mechanisms. As shown in the literature, Yilmaz et al. [222] designed a passive low-pass filter-type vibration with low stop-band frequencies by using the lever-type structures without hinge joint. However, the hinge joint is a simple way to achieve the inertial amplification mechanism in the metamaterials. Such as in the other literature, Frandsen et al.[224] introduced the inertial amplification mechanism into a continuous elastic rod to obtain wide bandgap by using the hinge joints.

7.1.2 Analysis of the simplified model

The simplified model of the inertially amplified mechanism of the unit cell of the IAM is illustrated in Fig. 7-1(d). The m_a takes the value of the mass of one arm in the middle of the arm. The k and k_a mean the stiffness of the beam and arm, respectively. Here, the k_a can be regard as rigid at ultra-low frequencies. The angle θ between the arm and the beam is 5°. All the geometric parameters are shown in Figs. 7-1(c) and (e). It is noted that the lattice constant a is 55 mm and the unit of all the geometric parameters is millimeter.

In Fig. 7-1(d), the x_1 and x_2 represent the displacement of the input and output, respectively. At ultra-low frequencies, the horizontal and vertical displacement of the two m_a are

$$x_a = \frac{(3x_1+x_2)}{4}, \tag{7-1}$$

$$z_a = \cot(\theta)\frac{(x_1-x_2)}{4}, \tag{7-2}$$

$$x_b = \frac{(x_1+3x_2)}{4}, \tag{7-3}$$

$$z_b = \cot(\theta)\frac{(x_1-x_2)}{4}. \tag{7-4}$$

Therefore, the kinetic energy (T) and potential energy (V) of the system are

$$T = \frac{m_a(\dot{x}_a^2+\dot{z}_a^2)}{2} + \frac{m_a(\dot{x}_b^2+\dot{z}_b^2)}{2}, \tag{7-5}$$

$$V = \frac{k(x_2 - x_1)^2}{2}. \tag{7-6}$$

From the Lagrange's equation, i.e.,

$$0 = \frac{d}{dt}\left(\frac{\partial L}{\partial \dot{x}_2}\right) - \frac{\partial L}{\partial x_2}, \tag{7-7}$$

where the L is the Lagrange function:

$$L = T - V. \tag{7-8}$$

Substituting Eq. (7-8) into Eq. (7-7), we obtain

$$\left(\frac{2m_a[5+\cot^2(\theta)]}{16}\right)\ddot{x}_2 + kx_2 = \frac{2m_a[\cot^2(\theta)-2]}{16}\ddot{x}_1 + kx_1. \tag{7-9}$$

When the two sides of Eq. (7-9) are equal to zero, the first resonance (ω_r) and first anti-resonance (ω_{ar}) [199,224,227] frequencies are obtained:

$$\omega_r = \sqrt{\frac{k}{2m_a[5+\cot^2(\theta)]/16}}, \tag{7-10}$$

$$\omega_{ar} = \sqrt{\frac{k}{2m_a[\cot^2(\theta)-2]/16}}. \tag{7-11}$$

As can be seen from Eqs. (7-10) and (7-11), the ω_r is always lower than the ω_{ar}. When the angle θ is less than 16.7°, the function $\eta = [5 + \cot^2(\theta)]/16$ is larger than 1, which means the amplified motion for the mass is caused by the inertially amplified mechanism and the inertial mass is amplified η times. Of course, according to Eq. (7-10), if the stiffness k is weaker or the mass of two arms is heavier, the lower ω_r can be obtained. It is worth noting that, comparing with the metamaterials based on local resonance,[230,231] the inertial amplification mechanism is also based on the local resonance, which can be found from Eq. (7-10), but it can easily obtain lower-frequency bandgap because of the function $\eta = [5 + \cot^2(\theta)]/16$ appeared in Eq. (7-10). For example, in this work, the angle θ is 5°, so the inertial mass is amplified about 8.5 times. Therefore, the small mass can achieve strong resonance at low frequencies.

In the simulations, all results are calculated by using finite element software COMSOL 5.4 (Multibody Dynamics Module). The Floquet-Bloch boundary conditions are achieved on the unit cell along x direction by using both boundary similarity and pointwise constraint. In the Fig. 7-1(e), the hinge-connection condition is set on the hinge joints between two bodies. The transmission spectrums of the flexural waves in

experiments and simulations are defined as

$$TS = 20 \times \log_{10}(R_b/R_a), \tag{7-12}$$

where R_a and R_b are the root mean square (RMS) of the out-of-plane velocities at the points a and b shown in Fig. 7-1(b), respectively.

Table 7-1 The material parameters used in this chapter

Material	Density (kg/m^3)	Young's modulus (Pa)	Poisson's ratio
PLA	1086.3	3.4398×10^9	0.35
Steel	7784	2.07×10^{11}	0.3
Soil	1800	2×10^7	0.3

7.2 Results of the inertially amplified metamaterial

7.2.1 **Band structure and transmission**

Figure 7-2(a) illustrates the band structure of the IAM along *x* direction and the color bar represents the degree of the out-of-plane polarization. The parameter ξ is used to defined the degree of the out-of-plane polarization:

$$\xi = \left|\int_C w\, dC\right| / \int_C |disp.|\, dC \tag{7-13}$$

where *w* is the integral of the *z* component of the displacement fields in the *yz*-cut plane (to avoid the effect of the torsional modes in the beam); and *disp.* is the total displacement; and *C* means the whole unit cell. Therefore, in Fig. 7-2(a), it is obvious that a bandgap induced by inertial amplification is generated for flexural waves in the frequency range from 70 to 108 Hz.

As shown in Fig. 7-2(b), in the frequency range of the bandgap, a significant attenuation zone can be found in the simulation results. Comparing with all the experimental results, the IAM has an attenuation zone for the flexural waves around from 70 to 108 Hz. Indeed, the experimentally measured attenuation of the IAM is far inferior compared to the simulated one. This is due to the fact that the hinge joints are rigid and smooth in the simulations, but not in the experiments. However, comparing with other two experimental samples (bare beam and TM), the attenuation zone is not

difficult to find. It is noted the unit cell of the TM has more mass than the IAM, but the frequency of the first bandgap of the TM for flexural waves is much higher than the IAM. The band structure of the TM, which is easy to calculate just by using Solid Module of the COMSOL,[33,34,114,218] is not illustrated in this chapter.

7.2.2 Vibration modes

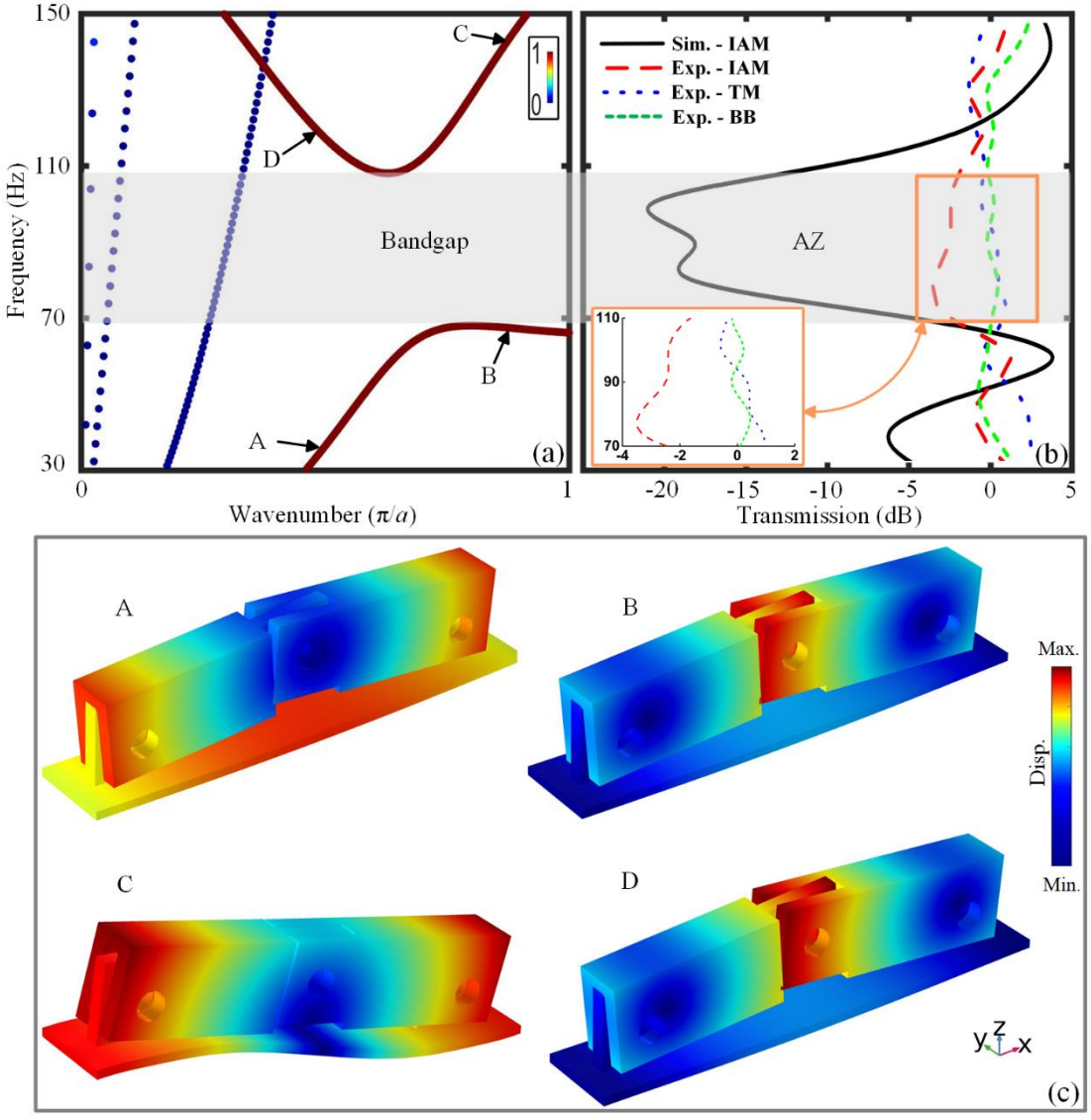

Figure 7-2 The band structure and transmission

(a) The band structure of the IAM. The color bar represents the degree of the out-of-plane polarization. (b) The transmission spectrums of the flexural waves in the IAM, the TM and the BB (bare beam). The AZ is attenuation zone. (c) Vibration modes corresponding to points A – D shown in (a). The color bar in (c) represents the degree of displacement

Figure 7-2(c) illustrates the vibration modes at the marked points A - D in the band

structure shown in Fig. 7-2(a). At points A and C, the significant displacement appears in the beam and around the hinge joints between beam and arms. Due to the similar vibration modes and slopes (in the band structure) of these two points, it is clear that these two points come from the same band which is opened by the bandgap. This is common in the band structures of the metamaterials based on local resonance.[165,232] At points B and D, almost all the displacement appears around the hinge joint between two arms, which means that there is a strong resonance only on the two arms. Based on this information, it is not difficult to infer that the low-frequencies bandgap is opened by the local resonance of the inertial amplification mechanism.

7.3 Results of the inertially amplified seismic metamaterial

7.3.1 **Model and band structure**

It is noted that the simplified model of embedded inertial amplification mechanism shown in Fig. 7-1(d) can also theoretically work on a half-space when the substrate provides the stiffness k. Therefore, in theory, the embedded inertial amplification mechanism is very suitable to design surface wave metamaterials, which, just with small mass, can induce low-frequency bandgap for surface waves. As shown in Fig. 7-3(a), the embedded inertial amplification mechanism is introduced on a half-space to attenuate seismic surface waves. The unit cell of the seismic metamaterial (SM) is constituted of three parts: two steel arms represented by gray area, three hinge joints represented by dotted circle and soil substrate represented by yellow area. The blue and red lines represent Floquet-Bloch boundary condition and fixed constraint, respectively. The lattice constant a in Fig. 7-3(a) is 2 m and the depth of the soil substrate is $H = 500a$ [114,229]. The angle θ is also 5° and other geometer parameters are shown in Fig. 7-3(a). The material parameters of the steel and soil used in this letter are shown in table 7-1.

Figure 7-3(b) illustrates the band structure of the one-dimension periodic SM. The sound cone and the bandgap for surface waves are represented by the dark grey and light grey zones, respectively. The bandgap is in the range from 4.0 to 4.7 Hz and the relative bandwidth is 0.16. Despite the narrow width of this bandgap, the definitive existence of this bandgap is encouraging.

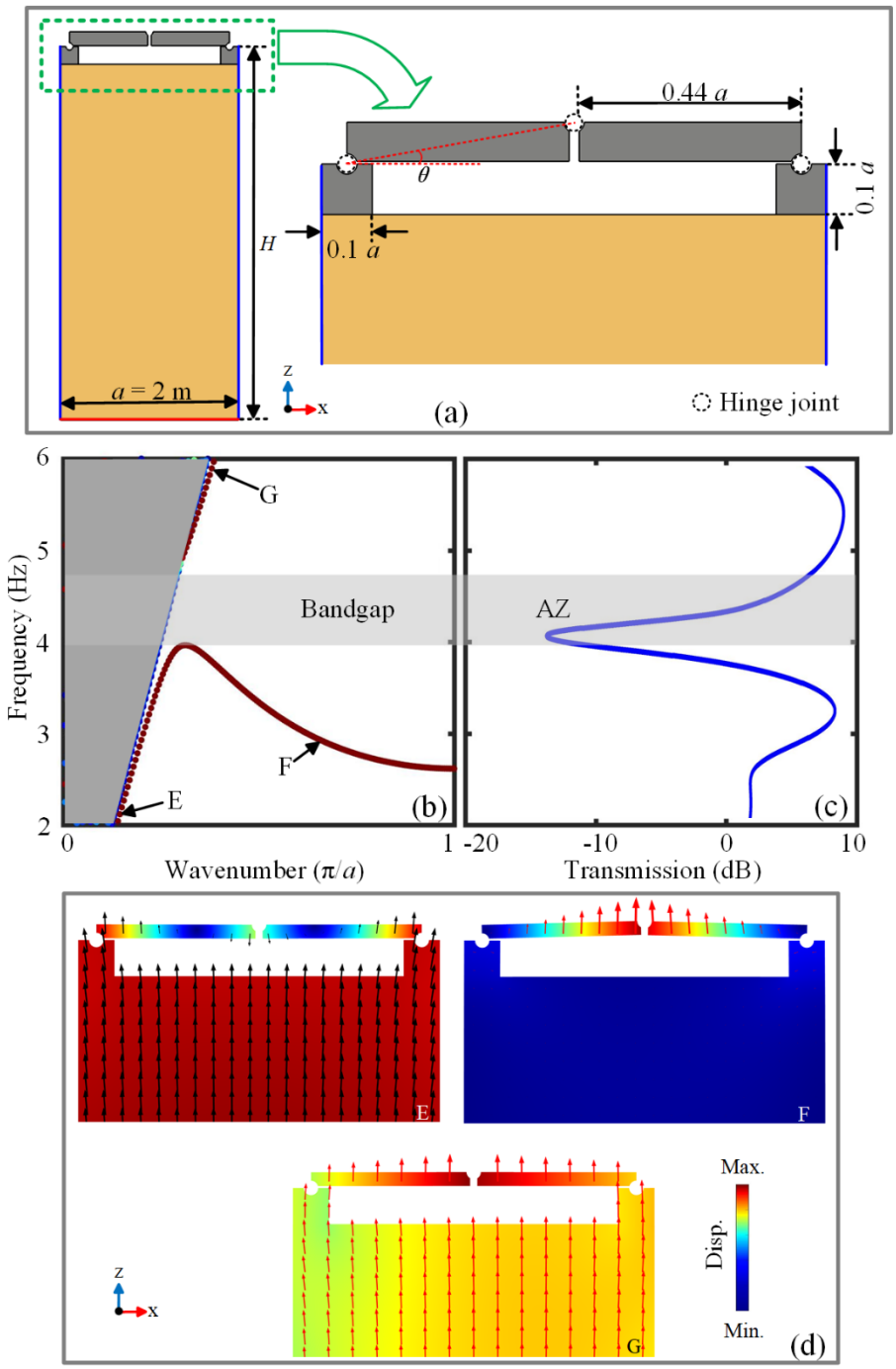

Figure 7-3 Study of the inertially amplified seismic metamaterial

(a) The unit cell of the SM with embedded inertial amplification mechanism. The blue and red lines represent Floquet-Bloch boundary conditions and fixed constraint, respectively. The dotted circle represents hinge joint between two bodies. (b) The band structure of the SM. (c) The transmission spectrum of the surface waves in the SM with 7 unit cells. (d) Vibration modes corresponding to points E – G shown in (b). The color bar in (d) represents the degree of displacement. The arrows indicate the displacement eigenvector, whose length and direction represent the magnitude and trend of the particle movement, respectively

It is noted that the SM based on the embedded inertial amplification mechanism with smaller mass can achieve a bandgap with larger relative bandwidth than the SM based on the inertial amplification mechanism [229] at low frequencies. As shown in Fig. 7-3(c), it is the transmission spectrum of the surface waves in the SM with 7 unit cells.[114,163,164] An attenuation peak can be found around at 4 Hz. The band structure of the SM and the attenuation effects of the surface waves in the SM all demonstrate that the existence of the ultra-low-frequencies bandgap.

7.3.2 **Vibration modes**

Figure 7-3(d) illustrates the vibration modes at the marked points E - G in the band structure shown in Fig. 7-3(b). The arrows shown in the unit cell indicate the displacement eigenvector, whose length and direction represent the magnitude and trend of the particle movement, respectively. At points E and G, the significant displacement appears both in the soil substrate and the arms. At point F, almost all the displacement appears around the hinge joint between the two arms, which is similar as the bandgap shown in Fig. 7-2. The strong local resonance appears only on the two arms of the inertial amplification mechanism. It demonstrates the bandgap for surface waves is induced by the inertial amplification.

7.4 Conclusion

In summary, an alternative type of seismic metamaterial with an ultra-low-frequency bandgap induced by inertial amplification has been presented and discussed to isolate seismic surface waves. We first have proposed a one-dimensional inertially amplified metamaterial, whose unit cell is composed of one base beam, two arms and three hinge joints. The experimental and simulated results of transmissions of the flexural waves in the bare beam, traditional metamaterial and inertially amplified metamaterial have demonstrated that the inertially amplified metamaterial is capable of isolating flexural waves in the bandgap induced by inertial amplification. Finally, the embedded inertial amplification mechanism has been introduced on a soil half-space to design the seismic metamaterial. The band structure and the transmission results have shown that the seismic metamaterial can isolate seismic Rayleigh waves at ultra-low frequencies. It is worth noting that the embedded inertial amplification mechanisms with small mass can strongly attenuate elastic waves at ultra-low frequencies, which is

a very needed and sought property for seismic metamaterials. This work evidences that the embedded inertial amplification mechanisms can induce bandgaps for seismic surface waves at ultra-low frequencies.

Chapter 8 Conclusions and Prospects

8.1 Conclusions

The seismic metamaterials (SMs) make it possible to protect buildings in a way of efficiently attenuating and effectively controlling seismic waves. SMs can attenuate seismic waves on the way of propagating to buildings, thereby protecting people's lives and property. Considering the multiple and high hazard of earthquakes, as well as some disadvantages that cannot be ignored in the seismic isolations, SMs have shown the application prospects. In order to attenuate seismic Rayleigh waves in a wide-low-frequency range, several kinds of SMs are designed in this thesis. The transmission characteristics of seismic Rayleigh waves in the SMs are studied by combining theoretical model analysis, numerical simulation and experimental investigation. The main contents and conclusions include:

1. Basing on the lab-scale experiments and numerical simulation of the SM consisting of the two-component seismic metamaterial plate (SMP) and a half space, a new design methodology to create SMs to attenuate seismic surface waves is demonstrated. In addition, lab-scale experiments are also the important basis for the application of three-component subwavelength SM. Then a three-component subwavelength SM consisting of the three-component SMP and a half space is proposed. By analyzing the propagation of Rayleigh waves in the one-dimensional (1D) and 2D SMs in the frequency range of the ultra-low frequency bandgap, it is found that Rayleigh waves are deflected at a certain angle and converted into bulk waves. In summary, the SM consisting of only one layer of the SMP buried underground and substrate has an ultra-low frequency bandgap and can convert Rayleigh waves into bulk waves in the frequency range of the bandgap.

2. An 1D inverted T-shaped SM (ITSM) with an ultra-wide first bandgap (FBG) has been proposed by improving the pillar-like SM. The effects of the geometrical and material parameters of the ITSM on the FBG have been also discussed. It is found that the appearance of the plate obviously increases the center frequency and relative bandwidth of the FBG of the ITSM. The complex band structure of the ITSM has been calculated to analyze the attenuation mechanism of surface waves. It can be found that

the FBG of the ITSM is composed of two parts. It is found that the propagation modes of surface waves in the ITSM are completely different in different parts of the FBG. Finally, a kind of the 2D ITSM with 25 unit cells is proposed in large-scale field experiments, which can attenuate Rayleigh waves in a ultra-wide frequency range.

3. The mechanical property of the lowest-frequency attenuation zone (LFAZ) of the elastic metamaterial made of pillars on a substrate has been investigated numerically. It is found that the LFAZ is immobile with the changed distances between pillars. The "rainbow trapping effect" in the second attenuation zone (SAZ) has then been demonstrated by numerical simulation and experiments. Therefore, for a properly designed elastic metamaterial, there is an opportunity to connect lower bound of the SAZ and the upper bound of the LFAZ. A wide attenuation zone from an ultra-low frequency for surface waves by just using one kind of artificial structures on a substrate can be obtained. In the case of the seismic Rayleigh waves, these two characteristics of the LFAZ and the SAZ are used to design a kind of seismic metamaterial by just using one kind of artificial steel structure on a soil substrate. The proposed seismic metamaterial can attenuation the Rayleigh waves from 5 to 22 Hz.

4. A conceived metamaterial plate (MMP) with lever-type structures has been experimentally investigated and discussed. It is shown that a wide bandgap for flexural waves appears in a low-frequency region. The propagation analysis measured on the back side of the MMP has demonstrated that the lever-type structures strongly attenuate the flexural waves. Finally, the similar lever-type structures are introduced into a soil half-space to obtain the bandgaps induced by inertial amplification for seismic surface waves in a low-frequency range. The significant advantage is that inertial amplification mechanisms with small mass can achieve strong vibration attenuation at low frequencies, a property that should be realized for SMs.

5. A one-dimensional inertially amplified metamaterial is proposed, whose unit cell is composed of one base beam, two arms and three hinge joints. The experimental and simulated results of transmissions of the flexural waves in the bare beam, traditional metamaterial and inertially amplified metamaterial have demonstrated that the inertially amplified metamaterial is capable of isolating flexural waves in the bandgap induced by inertial amplification. Finally, the embedded inertial amplification mechanism has been introduced on a soil half-space to design the SM. The band structure and the

transmission results have shown that the SM can isolate seismic Rayleigh waves at ultra-low frequencies.

For important infrastructures such as defense, nuclear power stations and government buildings, the three-component SMs that attenuates seismic waves over a wide and ultra-low frequency range. Although at high cost, it can be used for seismic protection. For cities and other places with a large number of buildings, inverted T-shaped SMs are more suitable for seismic protection. For single buildings, such as ancient buildings, SMs based on the inertial amplification mechanism can be used for seismic protection.

8.2 Innovations

In this thesis, based on the local resonance, inverse dispersion effect, Rainbow trapping effect and inertial amplification characteristics, the three-component, inverted T-shaped, gradient, lever-type and embedded-type seismic metamaterials are designed. The transmission characteristics of seismic Rayleigh waves in the seismic metamaterials are studied by combining theoretical model analysis, numerical simulation and experimental investigation. The innovations of the research work in this thesis are:

1. A three-component seismic metamaterial is proposed to attenuate seismic Rayleigh waves over an ultra-wide low frequency range. The inverse-dispersion property of the two-layered structure to attenuate seismic Rayleigh waves is found.
2. An inverted T-shaped seismic metamaterial is proposed to obtain an ultra-wide first bandgap for seismic Rayleigh waves. The attenuation effect of the structure for seismic Rayleigh waves is verified by field experiments and numerical simulations.
3. A gradient seismic metamaterial is proposed, which combines the local resonance property of the first bandgap and the “rainbow trapping effect” of the second bandgap to achieve strong attenuation of seismic Rayleigh waves in an ultra-wide low frequency range.
4. Based on the inertial amplification property, a lever-type seismic metamaterial and an embedded seismic metamaterial are proposed to attenuate seismic Rayleigh waves in the ultra-low frequency range using only a small mass.

8.3 Prospects

On the basis of this thesis, there are still many issues that need to be further

researched, such as:

1. The studies in this thesis are mostly based on the elastic dynamics, which is not exactly the same as reality. The soil half-space commonly used in the thesis instead of the geological environment of the Earth, although it can be approximated as a homogeneous half-space medium in some cases, the geological environment inside the Earth is very complex. For example, the phenomenon of layering of soils and the fact that soils are viscoelastic and porous plasticity are not considered.

2. The simulations and theoretical studies show a perfect continuity between different materials, while in reality it is different. It is difficult to achieve perfect continuity between different materials with vastly different properties. Perfect continuity between soil and steel, for example, needs to be achieved using other means, which have not been considered in this thesis either.

3. At present, academic research on seismic metamaterials is abundant, but practical applications of seismic metamaterials are absent. Efforts should be made to promote seismic metamaterials into practical applications.

4. In this thesis, point source excitation is used to generate surface waves, but the situation in real earthquakes is more complex. Data collected in real earthquakes should be used to verify the practicality of seismic metamaterials.

5. The design methods and theories of phononic crystals and other related metamaterials can be used to achieve a systematic design of seismic metamaterials.

References

[1] Gutenberg B and Richter C. On Seismic Waves [M]. Berlin: Akademische Verlagsgesellschaft, 1934.

[2] Honda H. Earthquake mechanism and seismic waves [J]. Journal of Physics of the Earth, 1962, 10(2): 1-97.

[3] White J E. Seismic Waves: Radiation, Transmission, and Attenuation [M]. New York: McGraw-Hill, 1965.

[4] Ben-Menahem A and Singh S J. Seismic Waves and Sources [M]. Berlin: Springer Science & Business Media, 2012.

[5] Aki K. Earthquake mechanism [J]. Tectonophysics, 1972, 13(1-4): 423-446.

[6] Corwin R F and Morrison H. Self-potential variations preceding earthquakes in central California [J]. Geophysical Research Letters, 1977, 4(4): 171-174.

[7] Mizutani H. Earthquakes and electromagnetic phenomena [J]. Earthquake Prediction Techniques: Their application in Japan, 1982, 1982: 217-246.

[8] Du J, Li D, Wang Y, et al. Late quaternary activity of the Huashan Piedmont fault and associated hazards in the southeastern Weihe Graben, Central China [J]. Acta Geologica Sinica-English Edition, 2017, 91(1): 76-92.

[9] Scholz C. A physical interpretation of the Haicheng earthquake prediction [J]. Nature, 1977, 267(5607): 121-124.

[10] Jin A and Aki K. Temporal change in coda Q before the Tangshan earthquake of 1976 and the Haicheng earthquake of 1975 [J]. Journal of Geophysical Research: Solid Earth, 1986, 91(B1): 665-673.

[11] Wang K, Chen Q-F, Sun S, et al. Predicting the 1975 Haicheng earthquake [J]. Bulletin of the Seismological Society of America, 2006, 96(3): 757-795.

[12] Wyss M and Wu Z. How many lives were saved by the evacuation before the M 7.3 Haicheng earthquake of 1975? [J]. Seismological Research Letters, 2014, 85(1): 126-129.

[13] Sheng Z-Y. Medical support in the Tangshan earthquake: a review of the management of mass casualties and certain major injuries [J]. The Journal of Trauma, 1987, 27(10): 1130-1135.

[14] Liu H, George W H, Xie L, et al. The great Tangshan earthquake of 1976 [J]. EERL Report, 2002, 001: 26539.

[15] Hüffmann G K. Full base isolation for earthquake protection by helical springs and viscodampers [J]. Nuclear Engineering and Design, 1985, 84(3): 331-338.

[16] Coburn A and Spence R. Earthquake Protection [M]. New Jersey: John Wiley & Sons, 2003.

[17] Alhan C and Gavin H P. Reliability of base isolation for the protection of critical equipment from earthquake hazards [J]. Engineering Structures, 2005, 27(9): 1435-1449.

[18] Taranath B S. Wind and Earthquake Resistant Buildings: Structural Analysis and Design [M]. Florida: CRC Press, 2004.

[19] Agrawal P and Shrikhande M. Earthquake Resistant Design of Structures [M]. Delhi: PHI Learning Pvt. Ltd., 2006.

[20] Kmar E R, Mathur E P, and Pandey E T. A study on earthquake resistant construction techniques [J]. American Journal of Engineering Research, 2013, 02(12): 258-264.

[21] Grant D N, Fenves G L, and Whittaker A S. Bidirectional modelling of high-damping rubber bearings [J]. Journal of Earthquake Engineering, 2004, 8(spec01): 161-185.

[22] Kalpakidis I V and Constantinou M C. Effects of heating on the behavior of lead-rubber bearings. I: Theory [J]. Journal of Structural Engineering, 2009, 135(12): 1440-1449.

[23] Kalpakidis I V and Constantinou M C. Effects of heating on the behavior of lead-rubber bearings. II: Verification of theory [J]. Journal of Structural Engineering, 2009, 135(12): 1450-1461.

[24] Kalpakidis I V, Constantinou M C, and Whittaker A S. Modeling strength degradation in lead–rubber bearings under earthquake shaking [J]. Earthquake Engineering & Structural Dynamics, 2010, 39(13): 1533-1549.

[25] Kelly J M and Konstantinidis D. Mechanics of Rubber Bearings for Seismic and Vibration Isolation [M]. New York: Wiley Online Library, 2011.

[26] Fu Y and Kasai K. Comparative study of frames using viscoelastic and viscous dampers [J]. Journal of Structural Engineering, 1998, 124(5): 513-522.

[27] Pekcan G, Mander J B, and Chen S S. Fundamental considerations for the design of non - linear viscous dampers [J]. Earthquake Engineering & Structural Dynamics, 1999, 28(11): 1405-1425.

[28] Youssef N. Viscous dampers at multiple levels for the historic preservation of Los Angeles City Hall [J]. The Structural Design of Tall Buildings, 2001, 10(5): 339-350.

[29] Lin W H and Chopra A K. Earthquake response of elastic SDF systems with non - linear fluid viscous dampers [J]. Earthquake Engineering & Structural Dynamics, 2002, 31(9): 1623-1642.

[30] Tafheem Z, Arafat T A, Chowdhury A, et al. Seismic Isolation Systems in Structures-the State of Art Review [C]. Proceedings of 11th Global Engineering, Science and Technology Conference, Dhaka: Diamond Scientific Publishing,

2015: 18-19.

[31] Kim S-H and Das M P. Artificial seismic shadow zone by acoustic metamaterials [J]. Modern Physics Letters B, 2013, 27(20): 1350140.

[32] Finocchio G, Casablanca O, Ricciardi G, et al. Seismic metamaterials based on isochronous mechanical oscillators [J]. Applied Physics Letters, 2014, 104(19): 191903.

[33] Brûlé S, Javelaud E, Enoch S, et al. Experiments on seismic metamaterials: Molding surface waves [J]. Physical Review Letters, 2014, 112(13): 133901.

[34] Miniaci M, Krushynska A, Bosia F, et al. Large scale mechanical metamaterials as seismic shields [J]. New Journal of Physics, 2016, 18(8): 083041.

[35] Colombi A, Colquitt D, Roux P, et al. A seismic metamaterial: The resonant metawedge [J]. Scientific Reports, 2016, 6: 27717.

[36] Casablanca O, Ventura G, Garescì F, et al. Seismic isolation of buildings using composite foundations based on metamaterials [J]. Journal of Applied Physics, 2018, 123(17): 174903.

[37] Geng Q, Zhu S, and Chong K P. Issues in design of one-dimensional metamaterials for seismic protection [J]. Soil Dynamics and Earthquake Engineering, 2018, 107: 264-278.

[38] Liu W, Yoon G H, Yi B, et al. Ultra-wide band gap metasurfaces for controlling seismic surface waves [J]. Extreme Mechanics Letters, 2020, 41: 101018.

[39] Liu Z, Dong H-W, Yu G-L, et al. Achieving ultra-broadband and ultra-low-frequency surface wave bandgaps in seismic metamaterials through topology optimization [J]. Composite Structures, 2022, 295: 115863.

[40] Meseguer F, Holgado M, Caballero D, et al. Rayleigh-wave attenuation by a semi-infinite two-dimensional elastic-band-gap crystal [J]. Physical Review B, 1999, 59(19): 12169.

[41] Wu T-T, Wu L-C, and Huang Z-G. Frequency band-gap measurement of two-dimensional air/silicon phononic crystals using layered slanted finger interdigital transducers [J]. Journal of Applied Physics, 2005, 97(9): 094916.

[42] Laude V, Wilm M, Benchabane S, et al. Full band gap for surface acoustic waves in a piezoelectric phononic crystal [J]. Physical Review E, 2005, 71(3): 036607.

[43] Benchabane S, Khelif A, Rauch J-Y, et al. Evidence for complete surface wave band gap in a piezoelectric phononic crystal [J]. Physical Review E, 2006, 73(6): 065601.

[44] Norris R C, Hamel J S, and Nadeau P. Phononic band gap crystals with periodic fractal inclusions: Theoretical study using numerical analysis [J]. Journal of Applied Physics, 2008, 103(10): 104908.

[45] Kuo N-K and Piazza G. Fractal phononic crystals in aluminum nitride: An approach to ultra high frequency bandgaps [J]. Applied Physics Letters, 2011, 99(16): 163501.

[46] Li J-B, Wang Y-S, and Zhang C. Tuning of acoustic bandgaps in phononic crystals with Helmholtz resonators [J]. Journal of Vibration and Acoustics, 2013, 135(3): 031015.

[47] Gao N, Hou H, Cheng B, et al. A hollow inclusion self-similarity phononic crystal with an ultra-low-frequency bandgap [J]. International Journal of Modern Physics B, 2017, 32(02): 1850005.

[48] Krushynska A O, Miniaci M, Bosia F, et al. Coupling local resonance with Bragg band gaps in single-phase mechanical metamaterials [J]. Extreme Mechanics Letters, 2017, 12: 30-36.

[49] Lim C and Reddy J. Built-up structural steel sections as seismic metamaterials for surface wave attenuation with low frequency wide bandgap in layered soil medium [J]. Engineering Structures, 2019, 188: 440-451.

[50] Achaoui Y, Antonakakis T, Brûlé S, et al. Clamped seismic metamaterials: ultra-low frequency stop bands [J]. New Journal of Physics, 2017, 19(6): 063022.

[51] Brule S, Enoch S, and Guenneau S. Experimental evidence of auxetic features in seismic metamaterials: Ellipticity of seismic Rayleigh waves for subsurface architectured ground with holes [J]. ArXiv preprint arXiv:#1809.05841, 2018.

[52] Zeng Y, Peng P, Du Q-J, et al. Subwavelength seismic metamaterial with an ultra-low frequency bandgap [J]. Journal of Applied Physics, 2020, 128(1): 014901.

[53] Wang X, Wan S, Nian Y, et al. Periodic in-filled pipes embedded in semi-infinite space as seismic metamaterials for filtering ultra-low-frequency surface waves [J]. Construction and Building Materials, 2021, 313: 125498.

[54] Liu H, Li L, Jia Q, et al. Radial seismic metamaterials based on layering theory: Broadband shielding of ultra-low frequency seismic surface waves [J]. Frontiers in Materials, 2022, 9: 908058.

[55] Agency F E M. Risk Management Series: Designing for Earthquakes–a Manual for Architects (FEMA 454) [M]. District of Columbia: Federal Emergency Management Agency Washington, 2006.

[56] Rikitake T. Earthquake prediction [J]. Earth-Science Reviews, 1968, 4: 245-282.

[57] Mogi K. Earthquake Prediction [M]. United States: U.S. Department of Engergy, 1985.

[58] Rikitake T. Earthquake prediction: an empirical approach [J]. Tectonophysics, 1988, 148(3-4): 195-210.

[59] Keilis-Borok V. Earthquake prediction [J]. Annual Review of Earth and

Planetary Sciences, 2002, 30: 1-33.

[60] Kanamori H. Earthquake prediction: An overview [J]. International Geophysics, 2003, 81(B): 1205-1216.

[61] Harrington D and Shou Z. Bam earthquake prediction & space technology [J]. United Nations Programme on Space Applications, 2005, 16: 39-63.

[62] Berhich A, Belouadha F-Z, and Kabbaj M I. A location-dependent earthquake prediction using recurrent neural network algorithms [J]. Soil Dynamics and Earthquake Engineering, 2022, 161: 107389.

[63] Saini K, Kalra S, and Sood S K. An integrated framework for smart earthquake prediction: IoT, fog, and cloud computing [J]. Journal of Grid Computing, 2022, 20(2): 1-20.

[64] Allen R M and Kanamori H. The potential for earthquake early warning in southern California [J]. Science, 2003, 300(5620): 786-789.

[65] Gasparini P, Manfredi G, and Zschau J. Earthquake Early Warning Systems [M]. New York: Springer, 2007.

[66] Allen R M, Gasparini P, Kamigaichi O, et al. The status of earthquake early warning around the world: An introductory overview [J]. Seismological Research Letters, 2009, 80(5): 682-693.

[67] Allen R M and Melgar D. Earthquake early warning: Advances, scientific challenges, and societal needs [J]. Annual Review of Earth and Planetary Sciences, 2019, 47: 361-388.

[68] Cremen G, Galasso C, and Zuccolo E. Investigating the potential effectiveness of earthquake early warning across Europe [J]. Nature Communications, 2022, 13(1): 1-10.

[69] Böse M, Andrews J, O'Rourke C, et al. Testing the shakealert earthquake early warning system using synthesized earthquake sequences [J]. Seismological Research Letters, 2022, 94(1): 243-259.

[70] Lee W H and Espinosa-Aranda J M. Earthquake Early Warning Systems: Current Status and Perspectives [M]. New York: Springer, 2003.

[71] Peng C, Jiang P, Ma Q, et al. Chinese nationwide earthquake early warning system and its performance in the 2022 Lushan M 6.1 earthquake [J]. Remote Sensing, 2022, 14(17): 4269.

[72] Shi Y and Cai H. The main factors and mechanism effecting on the earthquake resistance stability of grottoes relics and countermeasures [C]. 12th World Conference on Earthquake Engineering, Auckland: New Zealand Society for Earthquake EngineeringUpper Hutt, 2000: 1351.

[73] Hu S. The earthquake-resistant properties of Chinese traditional architecture [J].

Earthquake Spectra, 1991, 7(3): 355-389.

[74] Chen S, Wang S, Li C, et al. A seismic capacity evaluation approach for architectural heritage using finite element analysis of three-dimensional model: A case study of the limestone hall in the ming dynasty [J]. Remote Sensing, 2018, 10(6): 963.

[75] Zayas V A, Low S S, and Mahin S A. A simple pendulum technique for achieving seismic isolation [J]. Earthquake Spectra, 1990, 6(2): 317-333.

[76] Mohammed J and Mohd Z J. Seismic isolation in buildings to be a practical reality: Behaviour of structure and installation technique [J]. Journal of Engineering and Technology Research, 2011, 3(4): 99-117.

[77] Martelli A and Forni M. Seismic isolation and other antiseismic systems: recent applications in Italy and worldwide [J]. Seismic Isolation And Protection Systems, 2010, 1(1): 75-123.

[78] Tsang H H, Lo S, Xu X, et al. Seismic isolation for low - to - medium - rise buildings using granulated rubber – soil mixtures: numerical study [J]. Earthquake Engineering & Structural Dynamics, 2012, 41(14): 2009-2024.

[79] Warn G P and Ryan K L. A review of seismic isolation for buildings: historical development and research needs [J]. Buildings, 2012, 2(3): 300-325.

[80] Johnson W, Kormi K, and Travis F. An investigation into the explosive deep drawing of circular blanks using the plug-cushion technique [J]. International Journal of Mechanical Sciences, 1964, 6(4): 287-294.

[81] Peng C-L, Jost-Brinkmann P-G, and Miethke R-R. The cushion scanning technique: a method of dynamic tongue sonography and its comparison with the transducer-skin coupling scanning technique during swallowing [J]. Academic Radiology, 1996, 3(3): 239-244.

[82] Uraoka T, Kawahara Y, Ohara N, et al. Carbon dioxide submucosal injection cushion: an innovative technique in endoscopic submucosal dissection [J]. Digestive Endoscopy, 2011, 23(1): 5-9.

[83] Mokha A, Constantinou M, and Reinhorn A. Further results on frictional properties of teflon bearings [J]. Journal of Structural Engineering, 1991, 117(2): 622-626.

[84] Makris N and Constantinou M. Analysis of motion resisted by friction. II. Velocity-dependent friction [J]. Journal of Structural Mechanics, 1991, 19(4): 501-526.

[85] Fenz D M and Constantinou M C. Behaviour of the double concave friction pendulum bearing [J]. Earthquake Engineering & Structural Dynamics, 2006, 35(11): 1403-1424.

[86] Fenz D M and Constantinou M C. Modeling triple friction pendulum bearings

for response-history analysis [J]. Earthquake Spectra, 2008, 24(4): 1011-1028.

[87] Kumar M, Whittaker A S, and Constantinou M C. Characterizing friction in sliding isolation bearings [J]. Earthquake Engineering & Structural Dynamics, 2015, 44(9): 1409-1425.

[88] Guerreiro L, Azevedo J, and Muhr A H. Seismic tests and numerical modeling of a rolling-ball isolation system [J]. Journal of Earthquake Engineering, 2007, 11(1): 49-66.

[89] Oliveira F, Botto M A, Morais P, et al. Semi-active structural vibration control of base-isolated buildings using magnetorheological dampers [J]. Journal of Low Frequency Noise, Vibration and Active Control, 2018, 37(3): 565-576.

[90] Sigalas M and Economou E N. Band structure of elastic waves in two dimensional systems [J]. Solid State Communications, 1993, 86(3): 141-143.

[91] Kushwaha M S, Halevi P, Dobrzynski L, et al. Acoustic band structure of periodic elastic composites [J]. Physical Review Letters, 1993, 71(13): 2022.

[92] Floquet G. Sur les équations différentielles linéaires à coefficients périodiques [J]. Annales Scientifiques de l'École Normale Supérieure, 1883, 12: 47-88.

[93] Bloch F. Quantum mechanics of electrons in crystal lattices [J]. Zeitschrift für Physik, 1928, 52: 555-600.

[94] Brillouin L. Wave Propagation in Periodic Structures: Electric Filters and Crystal Lattices [M]. New York: Dover Publications, 1953.

[95] Martínez-Sala R, Sancho J, Sánchez J V, et al. Sound attenuation by sculpture [J]. Nature, 1995, 378(6554): 241-241.

[96] Liu Z, Zhang X, Mao Y, et al. Locally resonant sonic materials [J]. Science, 2000, 289(5485): 1734-1736.

[97] Luo C, Johnson S G, Joannopoulos J, et al. Subwavelength imaging in photonic crystals [J]. Physical Review B, 2003, 68(4): 045115.

[98] Lu Z, Murakowski J A, Schuetz C A, et al. Three-dimensional subwavelength imaging by a photonic-crystal flat lens using negative refraction at microwave frequencies [J]. Physical Review Letters, 2005, 95(15): 153901.

[99] Xia F, Yun M, Liu M, et al. Negative refraction and subwavelength imaging in a hexagonal two-dimensional annular photonic crystal [J]. Journal of Applied Physics, 2013, 113(1): 013109.

[100] Torrent D and Sánchez-Dehesa J. Acoustic cloaking in two dimensions: a feasible approach [J]. New Journal of Physics, 2008, 10(6): 063015.

[101] Vanbésien O, Fabre N, Mélique X, et al. Photonic-crystal-based cloaking device at optical wavelengths [J]. Applied Optics, 2008, 47(10): 1358-1362.

[102] Farhat M, Guenneau S, and Enoch S. Ultrabroadband elastic cloaking in thin

plates [J]. Physical Review Letters, 2009, 103(2): 024301.

[103] Norris A and Shuvalov A. Elastic cloaking theory [J]. Wave Motion, 2011, 48(6): 525-538.

[104] Vasić B and Gajić R. Self-focusing media using graded photonic crystals: Focusing, Fourier transforming and imaging, directive emission, and directional cloaking [J]. Journal of Applied Physics, 2011, 110(5): 053103.

[105] John S. Light trapping and solar energy harvesting with 3D photonic crystals [C]. IEEE Photonics Conference 2012, Burlingame: IEEE, 2012: 126.

[106] Chen Z, Guo B, Yang Y, et al. Metamaterials-based enhanced energy harvesting: A review [J]. Physica B: Physics of Condensed Matter, 2014, 438(4): 1-8.

[107] Chang S-Y, Cheng P, Li G, et al. Transparent polymer photovoltaics for solar energy harvesting and beyond [J]. Joule, 2018, 2(6): 1039-1054.

[108] Shen Y, Wang X, Lou S, et al. Evaluation of optical properties for real photonic crystal fiber based on total variation in wavelet domain [J]. Optical Fiber Technology, 2016, 31: 1-12.

[109] Lu G, Duan Z, Yin H, et al. Determining the effective electromagnetic parameters of photonic crystal by phase unwrapping and denoising method [J]. International Journal of Antennas and Propagation, 2019, 2019: 8513150.

[110] Lim C. From photonic crystals to seismic metamaterials: A review via phononic crystals and acoustic metamaterials [J]. Archives of Computational Methods in Engineering, 2021, 29(2): 1-62.

[111] Meng H, Bailey N, Chen Y, et al. 3D rainbow phononic crystals for extended vibration attenuation bands [J]. Scientific Reports, 2020, 10(1): 1-9.

[112] Wang Y-F, Wang Y-S, and Su X-X. Large bandgaps of two-dimensional phononic crystals with cross-like holes [J]. Journal of Applied Physics, 2011, 110(11): 113520.

[113] Ma G, Fu C, Wang G, et al. Polarization bandgaps and fluid-like elasticity in fully solid elastic metamaterials [J]. Nature Communications, 2016, 7: 13536.

[114] Zeng Y, Zhang S-Y, Zhou H-T, et al. Broadband inverted T-shaped seismic metamaterial [J]. Materials & Design, 2021, 208: 109906.

[115] Cao L, Yang Z, Xu Y, et al. Pillared elastic metasurface with constructive interference for flexural wave manipulation [J]. Mechanical Systems and Signal Processing, 2021, 146: 107035.

[116] Pu X, Palermo A, and Marzani A. A multiple scattering formulation for finite-size flexural metasurfaces [J]. Proceedings of the Royal Society A, 2022, 478(2262): 20210669.

[117] Habibullah Y B and Ishihara T. The role of nonlocal response in second harmonic generation at metasurfaces with triangular metaatoms [J]. European

Physical Journal-Applied Metamaterials, 2022, 9: 12.

[118] Yang M, Li T, and Yan X. Dual-stimulus control for ultra-wideband and multidimensional modulation in terahertz metasurfaces comprising graphene and metal halide perovskites [J]. ACS Applied Materials & Interfaces, 2021, 14(1): 2155-2165.

[119] Yuan J, Meng X, Ran J, et al. Manipulation of acoustic wave reflection for arbitrary reflecting surfaces based on acoustic metasurfaces [J]. International Journal of Modern Physics B, 2022, 36(6): 2250053.

[120] Seyed E H, Mohsen K, Wang F, et al. Spatial domain communication technique for future chipless ID sensors based on vortex terahertz beams generated by metasurfaces [J]. Results in Physics, 2022, 143: 106096.

[121] Liu J, Zhu X, He J, et al. Metasurfaces enabled dual-wavelength decoupling of near-field and far-field encoding [J]. Chinese Optics Letters, 2023, 21(2): 023602.

[122] Li Y, Luo Y, and Zhang X. Topological design of phononic crystals for multiple wide band gaps [J]. Journal of Sound and Vibration, 2022, 529: 116962.

[123] Chaunsali R, Feng L, and Yang J. Stress wave isolation by purely mechanical topological phononic crystals [J]. Scientific Reports, 2016, 6(1): 30662.

[124] Tang Y, Liang B, Yang J, et al. Topological phononic crystals with tunable interface state based on local resonance [J]. Applied Physics Express, 2019, 12(9): 094002.

[125] Laforge N, Wiltshaw R, Craster R V, et al. Acoustic topological circuitry in square and rectangular phononic crystals [J]. Physical Review Applied, 2021, 15(5): 054056.

[126] Hu G, Lan C, Tang L, et al. Local resonator stimulated polarization transition in metamaterials and the formation of topological interface states [J]. Mechanical Systems and Signal Processing, 2022, 165: 108388.

[127] Zhao J, Yang C, Yuan W, et al. Elastic valley spin controlled chiral coupling in topological valley phononic crystals [J]. Physical Review Letters, 2022, 129(27): 275501.

[128] Rayleigh L. On waves propagated along the plane surface of an elastic solid [J]. Proceedings of the London Mathematical Society, 1885, 1(1): 4-11.

[129] Tanaka N, Yagisawa J, and Yasuda S. Breaking pattern and critical breaking condition of Japanese pine trees on coastal sand dunes in huge tsunami caused by Great East Japan Earthquake [J]. Natural Hazards, 2013, 65(1): 423-442.

[130] Ogawa S, Ishiki M, Nako K, et al. Effects of the great east Japan earthquake and huge tsunami on glycaemic control and blood pressure in patients with diabetes

mellitus [J]. BMJ Open, 2012, 2(2): e000830.

[131] Kim S-H and Das M. Seismic negative belt of acoustic metamaterials [J]. ArXiv preprint arXiv:#1710.11273, 2017.

[132] Du Q, Zeng Y, Huang G, et al. Elastic metamaterial-based seismic shield for both Lamb and surface waves [J]. AIP Advances, 2017, 7(7): 075015.

[133] Colombi A, Roux P, Guenneau S, et al. Forests as a natural seismic metamaterial: Rayleigh wave bandgaps induced by local resonances [J]. Scientific Reports, 2016, 6: 19238.

[134] Du Q, Zeng Y, Xu Y, et al. H-fractal seismic metamaterial with broadband low-frequency bandgaps [J]. Journal of Physics D: Applied Physics, 2018, 51(10): 105104.

[135] Zeng Y, Xu Y, Deng K, et al. Low-frequency broadband seismic metamaterial using I-shaped pillars in a half-space [J]. Journal of Applied Physics, 2018, 123(21): 214901.

[136] Roux P, Bindi D, Boxberger T, et al. Toward seismic metamaterials: The metaforet project [J]. Seismological Research Letters, 2018, 89(2A): 582-593.

[137] Zeng Y, Xu Y, Yang H, et al. A Matryoshka-like seismic metamaterial with wide band-gap characteristics [J]. International Journal of Solids and Structures, 2020, 185-186: 334-341.

[138] Pu X, Palermo A, Cheng Z, et al. Seismic metasurfaces on porous layered media: Surface resonators and fluid-solid interaction effects on the propagation of Rayleigh waves [J]. International Journal of Engineering Science, 2020, 154: 103347.

[139] Wang Y-F and Wang Y-S. Complete bandgaps in two-dimensional phononic crystal slabs with resonators [J]. Journal of Applied Physics, 2013, 114(4): 043509.

[140] Wang Y-F, Wang Y-S, and Zhang C. Two-dimensional locally resonant elastic metamaterials with chiral comb-like interlayers: Bandgap and simultaneously double negative properties [J]. The Journal of the Acoustical Society of America, 2016, 139(6): 3311-3319.

[141] Wang Y-F, Wang Y-Z, Wu B, et al. Tunable and active phononic crystals and metamaterials [J]. Applied Mechanics Reviews, 2020, 72(4): 040801.

[142] Achaoui Y, Ungureanu B, Enoch S, et al. Seismic waves damping with arrays of inertial resonators [J]. Extreme Mechanics Letters, 2016, 8: 30-37.

[143] Bursi O S, Basone F, and Wenzel M. Stochastic analysis of locally resonant linear and hysteretic metamaterials for seismic isolation of process equipment [J]. Journal of Sound and Vibration, 2021, 510: 116263.

[144] Bao J, Shi Z, and Xiang H. Dynamic responses of a structure with periodic

foundations [J]. Journal of Engineering Mechanics, 2012, 138(7): 761-769.

[145] Xiang H, Shi Z, Wang S, et al. Periodic materials-based vibration attenuation in layered foundations: experimental validation [J]. Smart Materials and Structures, 2012, 21(11): 112003.

[146] Zhou X-Z, Wang Y-S, and Zhang C. Effects of material parameters on elastic band gaps of two-dimensional solid phononic crystals [J]. Journal of Applied Physics, 2009, 106(1): 014903.

[147] Yan Y, Cheng Z, Menq F, et al. Three dimensional periodic foundations for base seismic isolation [J]. Smart Material Structures, 2015, 24(7): 075006.

[148] Aravantinos-Zafiris N and Sigalas M. Large scale phononic metamaterials for seismic isolation [J]. Journal of Applied Physics, 2015, 118(6): 064901.

[149] Palermo A, Krödel S, Marzani A, et al. Engineered metabarrier as shield from seismic surface waves [J]. Scientific Reports, 2016, 6: 39356.

[150] Basone F, Wenzel M, Bursi O S, et al. Finite locally resonant metafoundations for the seismic protection of fuel storage tanks [J]. Earthquake Engineering & Structural Dynamics, 2018, 48(5): 1-21.

[151] Colquitt D, Colombi A, Craster R, et al. Seismic metasurfaces: Sub-wavelength resonators and Rayleigh wave interaction [J]. Journal of the Mechanics and Physics of Solids, 2017, 99: 379-393.

[152] Krödel S, Thomé N, and Daraio C. Wide band-gap seismic metastructures [J]. Extreme Mechanics Letters, 2015, 4: 111-117.

[153] Wu T-T, Huang Z-G, and Lin S. Surface and bulk acoustic waves in two-dimensional phononic crystal consisting of materials with general anisotropy [J]. Physical Review B, 2004, 69(9): 094301.

[154] Khelif A, Achaoui Y, Benchabane S, et al. Locally resonant surface acoustic wave band gaps in a two-dimensional phononic crystal of pillars on a surface [J]. Physical Review B, 2010, 81(21): 214303.

[155] Achaoui Y, Khelif A, Benchabane S, et al. Experimental observation of locally-resonant and Bragg band gaps for surface guided waves in a phononic crystal of pillars [J]. Physical Review B, 2011, 83(10): 104201.

[156] Assouar M B and Oudich M. Dispersion curves of surface acoustic waves in a two-dimensional phononic crystal [J]. Applied Physics Letters, 2011, 99(12): 123505.

[157] Lim C. Natural seismic metamaterials: the role of tree branches in the birth of Rayleigh wave bandgap for ground born vibration attenuation [J]. Trees, 2021, 35(4): 1299-1315.

[158] Wu X, Wen Z, Jin Y, et al. Broadband Rayleigh wave attenuation by gradient

metamaterials [J]. International Journal of Mechanical Sciences, 2021, 205: 106592.

[159] Palermo A, Vitali M, and Marzani A. Metabarriers with multi-mass locally resonating units for broad band Rayleigh waves attenuation [J]. Soil Dynamics and Earthquake Engineering, 2018, 113: 265-277.

[160] Zeng Y, Xu Y, Deng K, et al. A broadband seismic metamaterial plate with simple structure and easy realization [J]. Journal of Applied Physics, 2019, 125(22): 224901.

[161] Liu Z, Dong H-W, and Yu G-L. Topology optimization of periodic barriers for surface waves [J]. Structural and Multidisciplinary Optimization, 2021, 63(1): 463-478.

[162] Zhang S-Y, Wang Y-F, and Wang Y-S. Evanescent surface acoustic waves in 1D viscoelastic phononic crystals [J]. Journal of Applied Physics, 2021, 129(24): 245111.

[163] Graczykowski B, Alzina F, Gomis-Bresco J, et al. Finite element analysis of true and pseudo surface acoustic waves in one-dimensional phononic crystals [J]. Journal of Applied Physics, 2016, 119(2): 025308.

[164] Cai R, Jin Y, Rabczuk T, et al. Propagation and attenuation of Rayleigh and pseudo surface waves in viscoelastic metamaterials [J]. Journal of Applied Physics, 2021, 129(12): 124903.

[165] Wang Y, Zhang C, Chen W, et al. Precise and target-oriented control of the low-frequency Lamb wave bandgaps [J]. Journal of Sound and Vibration, 2021, 511: 116367.

[166] Gao J, Zou X-Y, Cheng J-C, et al. Band gaps of lower-order Lamb wave in thin plate with one-dimensional phononic crystal layer: Effect of substrate [J]. Applied Physics Letters, 2008, 92(2): 023510.

[167] Mindlin R. Influence of rotatory inertia and shear on flexural motions of isotropic, elastic plates [J]. Journal of Applied Mechanics, 1951, 18(1): 31-38.

[168] Chen Y, Feng Q, Scarpa F, et al. Harnessing multi-layered soil to design seismic metamaterials with ultralow frequency band gaps [J]. Materials & Design, 2019, 175: 107813.

[169] Wang G, Wen J, Liu Y, et al. Lumped-mass method for the study of band structure in two-dimensional phononic crystals [J]. Physical Review B, 2004, 69(18): 184302.

[170] Hsu J-C and Wu T-T. Efficient formulation for band-structure calculations of two-dimensional phononic-crystal plates [J]. Physical Review B, 2006, 74(14): 144303.

[171] Wang Y-Z, Li F-M, Kishimoto K, et al. Wave band gaps in three-dimensional

periodic piezoelectric structures [J]. Mechanics Research Communications, 2009, 36(4): 461-468.

[172] Oudich M and Badreddine Assouar M. Complex band structures and evanescent Bloch waves in two-dimensional finite phononic plate [J]. Journal of Applied Physics, 2012, 112(10): 104509.

[173] Du Q, Yang H, Lv T, et al. Multiband and polarization-independent left-handed metamaterial with cross fractal structure [J]. Optics Communications, 2013, 301: 74-77.

[174] Liu X-J and Fan Y-H. Band structure characteristics of T-square fractal phononic crystals [J]. Chinese Physics B, 2013, 22(3): 036101.

[175] Yan Z-Z and Wang Y-S. Wavelet-based method for calculating elastic band gaps of two-dimensional phononic crystals [J]. Physical Review B, 2006, 74(22): 224303.

[176] Khelif A, Aoubiza B, Mohammadi S, et al. Complete band gaps in two-dimensional phononic crystal slabs [J]. Physical Review E, 2006, 74(4): 046610.

[177] Wu T-T, Huang Z-G, Tsai T-C, et al. Evidence of complete band gap and resonances in a plate with periodic stubbed surface [J]. Applied Physics Letters, 2008, 93(11): 111902.

[178] Clorennec D and Royer D. Analysis of surface acoustic wave propagation on a cylinder using laser ultrasonics [J]. Applied Physics Letters, 2003, 82(25): 4608-4610.

[179] Pennec Y, Vasseur J O, Djafari-Rouhani B, et al. Two-dimensional phononic crystals: Examples and applications [J]. Surface Science Reports, 2010, 65(8): 229-291.

[180] Khelif A, Achaoui Y, and Aoubiza B. Surface acoustic waves in pillars-based two-dimensional phononic structures with different lattice symmetries [J]. Journal of Applied Physics, 2012, 112(3): 033511.

[181] Achaoui Y, Laude V, Benchabane S, et al. Local resonances in phononic crystals and in random arrangements of pillars on a surface [J]. Journal of Applied Physics, 2013, 114(10): 104503.

[182] Wang G, Wen X, Wen J, et al. Two-dimensional locally resonant phononic crystals with binary structures [J]. Physical Review Letters, 2004, 93(15): 154302.

[183] Yilmaz C, Hulbert G M, and Kikuchi N. Phononic band gaps induced by inertial amplification in periodic media [J]. Physical Review B, 2007, 76(5): 054309.

[184] Deymier P A. Acoustic Metamaterials and Phononic Crystals [M]. Berlin: Springer Science & Business Media, 2013.

[185] Khelif A and Adibi A. Phononic Crystals [M]. New York: Springer, 2015.

[186] Buchwald V. Rayleigh waves in transversely isotropic media [J]. The Quarterly Journal of Mechanics and Applied Mathematics, 1961, 14(3): 293-318.

[187] Alterman Z, Jarosch H, and Pekeris C. Propagation of Rayleigh waves in the earth [J]. Geophysical Journal International, 1961, 4(Supplement_1): 219-241.

[188] Xia J, Miller R D, and Park C B. Estimation of near-surface shear-wave velocity by inversion of Rayleigh waves [J]. Geophysics, 1999, 64(3): 691-700.

[189] Yang T-C, He J-S, Lu S-L, et al. Dispersion curves of Rayleigh wave in three-layer media [J]. Geophysical and Geochemical Exploration, 2004, 28(1): 41-45.

[190] Maurin F, Claeys C, Deckers E, et al. Probability that a band-gap extremum is located on the irreducible Brillouin-zone contour for the 17 different plane crystallographic lattices [J]. International Journal of Solids and Structures, 2018, 135: 26-36.

[191] Zhang S-Y, Yan D-J, Wang Y-S, et al. Wave propagation in one-dimensional fluid-saturated porous phononic crystals with partial-open pore interfaces [J]. International Journal of Mechanical Sciences, 2021, 195: 106227.

[192] Li F, Xia X, Deng Z, et al. Ultrafast Rayleigh-like streaming in a sub-wavelength slit between two phononic crystal plates [J]. Journal of Applied Physics, 2019, 125(13): 134903.

[193] Liu Z, Qin K-Q, and Yu G-L. Partially embedded gradient metabarrier: Broadband shielding from seismic Rayleigh waves at ultralow frequencies [J]. Journal of Engineering Mechanics, 2020, 146(5): 04020032.

[194] Pu X and Shi Z. Surface-wave attenuation by periodic pile barriers in layered soils [J]. Construction and Building Materials, 2018, 180: 177-187.

[195] Zeng Y, Cao L, Zhu Y, et al. Coupling the first and second attenuation zones in seismic metasurface [J]. Applied Physics Letters, 2021, 119(1): 013501.

[196] Shi Z and Huang J. Feasibility of reducing three-dimensional wave energy by introducing periodic foundations [J]. Soil Dynamics and Earthquake Engineering, 2013, 50: 204-212.

[197] Yan Y, Laskar A, Cheng Z, et al. Seismic isolation of two dimensional periodic foundations [J]. Journal of Applied Physics, 2014, 116(4): 044908.

[198] Pu X and Shi Z. A novel method for identifying surface waves in periodic structures [J]. Soil Dynamics and Earthquake Engineering, 2017, 98: 67-71.

[199] Li J and Li S. Generating ultra wide low-frequency gap for transverse wave isolation via inertial amplification effects [J]. Physics Letters A, 2018, 382(5): 241-247.

[200] Wang Y-F, Wang Y-S, and Laude V. Wave propagation in two-dimensional viscoelastic metamaterials [J]. Physical Review B, 2015, 92(10): 104110.

[201] Wang Y-F, Laude V, and Wang Y-S. Coupling of evanescent and propagating guided modes in locally resonant phononic crystals [J]. Journal of Physics D: Applied Physics, 2014, 47(47): 475502.

[202] Zhang B, Yu M, Lan C-Q, et al. Elastic wave and excitation mechanism of surface waves in multilayered media [J]. The Journal of the Acoustical Society of America, 1996, 100(6): 3527-3538.

[203] Cao L, Yang Z, Xu Y, et al. Flexural wave absorption by lossy gradient elastic metasurface [J]. Journal of the Mechanics and Physics of Solids, 2020, 143: 104052.

[204] Guo J, Cao J, Xiao Y, et al. Interplay of local resonances and Bragg band gaps in acoustic waveguides with periodic detuned resonators [J]. Physics Letters A, 2020, 384(13): 126253.

[205] Huang J, Shi Z, and Huang W. Multiple band gaps of phononic crystals with quasi-Sierpinski carpet unit cells [J]. Physica B: Condensed Matter, 2017, 516: 48-54.

[206] Yang T, Forward Modeling of Zigzag Dispersion and Pavement Systems Dispersion Curves [D]. Central South University Doctoral dissertation, 2004.

[207] Haskell N A. The dispersion of surface waves on multilayered media [J]. Bulletin of the seismological Society of America, 1953, 43(1): 17-34.

[208] Beaty K, Schmitt D, and Sacchi M. Simulated annealing inversion of multimode Rayleigh wave dispersion curves for geological structure [J]. Geophysical Journal International, 2002, 151(2): 622-631.

[209] Rydén N and Park C. Surface waves in inversely dispersive media [J]. Near Surface Geophysics, 2004, 2(4): 187-197.

[210] Zhou J, Zhang X, and Fang Y. Three-dimensional acoustic characteristic study of porous metasurface [J]. Composite Structures, 2017, 176(9): 1005-1012.

[211] Diatta A, Achaoui Y, Brûlé S, et al. Control of Rayleigh-like waves in thick plate Willis metamaterials [J]. AIP Advances, 2016, 6(12): 121707.

[212] Cao L, Zhu Y, Xu Y, et al. Elastic Bound State in the Continuum with Perfect Mode Conversion [J]. Journal of the Mechanics and Physics of Solids, 2021: 104502.

[213] Gan Q, Gao Y, Wagner K, et al. Experimental verification of the rainbow trapping effect in adiabatic plasmonic gratings [J]. Proceedings of the National Academy of Sciences, 2011, 108(13): 5169-5173.

[214] Hu H, Ji D, Zeng X, et al. Rainbow trapping in hyperbolic metamaterial waveguide [J]. Scientific Reports, 2013, 3: 1249.

[215] Zeng Y, Zhang S-Y, Zhou H-T, et al. Broadband inverted T-shaped seismic

metamaterial [J]. arXiv preprint arXiv:2012.09928, 2020.

[216] Gao G, Li N, and Gu X. Field experiment and numerical study on active vibration isolation by horizontal blocks in layered ground under vertical loading [J]. Soil Dynamics and Earthquake Engineering, 2015, 69: 251-261.

[217] Arnold C. EARTHQUAKE EFFECTS ON BUILDINGS 4 [J]. Des. Earthquakes, A Man. Archit., Federal Emergency Management Agency, 2006.

[218] Ding Y, Liu Z, Qiu C, et al. Metamaterial with simultaneously negative bulk modulus and mass density [J]. Physical Review Letters, 2007, 99(9): 093904.

[219] Colombi A, Craster R V, Colquitt D, et al. Elastic wave control beyond band-gaps: shaping the flow of waves in plates and half-spaces with subwavelength resonant rods [J]. Frontiers in Mechanical Engineering, 2017, 3: 10.

[220] An S, Shu H, Liang S, et al. Band gap characteristics of radial wave in a two-dimensional cylindrical shell with radial and circumferential periodicities [J]. AIP Advances, 2018, 8(3): 035110.

[221] Wu X, Wen Z, Jin Y, et al. Broadband Rayleigh wave attenuation by gradient metamaterials [J]. International Journal of Mechanical Sciences, 2021: 106592.

[222] Yilmaz C and Kikuchi N. Analysis and design of passive low-pass filter-type vibration isolators considering stiffness and mass limitations [J]. Journal of Sound and Vibration, 2006, 293(1-2): 171-195.

[223] Yilmaz C and Hulbert G. Theory of phononic gaps induced by inertial amplification in finite structures [J]. Physics Letters A, 2010, 374(34): 3576-3584.

[224] Frandsen N M, Bilal O R, Jensen J S, et al. Inertial amplification of continuous structures: Large band gaps from small masses [J]. Journal of Applied Physics, 2016, 119(12): 124902.

[225] Acar G and Yilmaz C. Experimental and numerical evidence for the existence of wide and deep phononic gaps induced by inertial amplification in two-dimensional solid structures [J]. Journal of Sound and Vibration, 2013, 332(24): 6389-6404.

[226] Taniker S and Yilmaz C. Design, analysis and experimental investigation of three-dimensional structures with inertial amplification induced vibration stop bands [J]. International Journal of Solids and Structures, 2015, 72: 88-97.

[227] Yuksel O and Yilmaz C. Realization of an ultrawide stop band in a 2-d elastic metamaterial with topologically optimized inertial amplification mechanisms [J]. International Journal of Solids and Structures, 2020, 203: 138-150.

[228] Brûlé S, Javelaud E H, Enoch S, et al. Flat lens effect on seismic waves propagation in the subsoil [J]. Scientific reports, 2017, 7(1): 18066.

[229] Zeng Y, Cao L, Wan S, et al. Seismic metamaterials: Generating low-frequency

bandgaps induced by inertial amplification [J]. International Journal of Mechanical Sciences, 2022: 107224.

[230] Mei J, Ma G, Yang M, et al. Dark acoustic metamaterials as super absorbers for low-frequency sound [J]. Nature communications, 2012, 3(1): 1-7.

[231] Mei J, Zhang X, and Wu Y. Ultrathin metasurface with high absorptance for waterborne sound [J]. Journal of Applied Physics, 2018, 123(9): 091710.

[232] Wang Y-F, Liang J-W, Chen A-L, et al. Wave propagation in one-dimensional fluid-saturated porous metamaterials [J]. Physical Review B, 2019, 99(13): 134304.

Vita

My name is Yi ZENG. I was born in January 1994 at Hubei, China. My research interests are in the field of seismic metamaterial designs. The acquired research results during my Ph.D. career in the form of papers and conference presentation are listed below.

List of Publications

[1] **Yi Zeng**, Shu-Yan Zhang, Hong-Tao Zhou, Yan-Feng Wang, Liyun Cao, Yifan Zhu, Qiu-Jiao Du, Badreddine Assouar, Yue-Sheng Wang. Broadband inverted T-shaped seismic metamaterial, Materials & Design, 2021, 208, 109906

[2] **Yi Zeng**, Liyun Cao, Sheng Wan, Tong Guo, Yan-Feng Wang, Qiu-Jiao Du, Badreddine Assouar, Yue-Sheng Wang. Seismic metamaterials: Generating low-frequency bandgaps induced by inertial amplification, International Journal of Mechanical Sciences, 2022, 221, 107224

[3] **Yi Zeng**, Liyun Cao, Sheng Wan, Tong Guo, Shuowei An, Yan-Feng Wang, Qiu-Jiao Du, Brice Vincent, Yue-Sheng Wang, Badreddine Assouar. Inertially amplified seismic metamaterial with an ultra-low-frequency bandgap, Applied Physics Letters, 2022, 121, 081701

[4] **Yi Zeng**, Liyun Cao, Yifan Zhu, Yan-Feng Wang, Qiu-Jiao Du, Yue-Sheng Wang, Badreddine Assouar. Coupling the first and second attenuation zones in seismic metasurface, Applied Physics Letters, 2021, 119, 013501

[5] **Yi Zeng**, Pai Peng, Qiu-Jiao Du, Yue-Sheng Wang, Badreddine Assouar. Subwavelength seismic metamaterial with an ultra-low frequency bandgap, Journal of Applied Physics, 2020, 128 (1), 014901

[6] Liyun Cao, Yifan Zhu, Sheng Wan, **Yi Zeng**, Badreddine Assouar. On the design of non-Hermitian elastic metamaterial for broadband perfect absorbers, International Journal of Engineering Science, 2022, 181, 103768

[7] Tingting Huang, Xin Ren, **Yi Zeng**, Yi Zhang, Chen Luo, Xiang Yu Zhang, Yi Min Xie. Based on auxetic foam: A novel type of seismic metamaterial for Lamb waves, Engineering Structures, 2021, 246, 112976

[8] Sheng Wan, Liyun Cao, **Yi Zeng**, Tong Guo, Mourad Oudich, Badreddine Assouar. Low-frequency nonreciprocal flexural wave propagation via compact cascaded time-modulated resonators, Applied Physics Letters, 2022, 120, 231701

[9] Liyun Cao, Yifan Zhu, Sheng Wan, **Yi Zeng**, Yong Li, Badreddine Assouar. Perfect absorption of flexural waves induced by bound state in the continuum, Extreme Mechanics Letters, 2021, 47, 101364

Conference

[1] **Yi Zeng** and Yue-Sheng Wang, *Research on a Novel Zero-Frequency Seismic Metamaterial*, The 1st National Conference on Metamaterials, 2019, Xi'an, oral presentation

[2] **Yi Zeng**, Badreddine Assouar and Yue-Sheng Wang, *Design and properties of broadband seismic metamaterials*, The 2th International Conference on Applied Mechanics and Advance Materials, 2023, Changsha, oral presentation

Étude et réalisation de métamatériaux séismiques large bande

Résumé

Le tremblement de terre désigne la vibration de la surface de la terre provoquée par la vibration d'un endroit ou d'une certaine zone sous la surface de la terre ou sous la surface de la terre. Il est généralement causé par des phénomènes naturels tels que les mouvements de la croûte terrestre, l'impact d'une météorite et une éruption volcanique. Il peut également être causé par des activités humaines telles que les explosions d'armes nucléaires. Les séismes catastrophiques connus à ce jour sont tous causés par un mouvement violent de la croûte terrestre. Les tremblements de terre peuvent provoquer des failles en surface, des secousses en surface, une liquéfaction en surface, des glissements de terrain, des répliques et même des tsunamis, ainsi que le moment où ils se produisent. Le nombre et l'intensité des répliques rendront la catastrophe plus grave. Par rapport à d'autres catastrophes naturelles, les tremblements de terre constituent une grande menace pour la sécurité des vies et des biens des personnes. Dans les temps anciens, comme le tremblement de terre de Jiajing qui s'est produit en janvier 1556, 830 000 personnes ont été tuées et des pertes économiques incommensurables ont été causées. Les villes modernes se caractérisent par des bâtiments denses et des taux d'occupation élevés, ainsi que par des problèmes tels que le sous-développement des systèmes d'alerte précoce et le manque de sensibilisation du public aux risques sismiques, qui exacerbent tous la gravité des catastrophes sismiques.

Après la fondation de la République Populaire de Chine, le tremblement de terre de Haicheng s'est produit dans la province du Liaoning. Il s'agit du seul cas réussi où le gouvernement a évacué la population de manière ordonnée et a réduit considérablement les dégâts en se basant sur une prédiction précise d'un tremblement de terre. Le nombre de victimes du tremblement de terre a été de 18 308, ce qui ne représente que 0,22% du nombre total de personnes dans la zone du tremblement de terre, avec seulement 0,02% du nombre total de décès. Un an plus tard, le tremblement de terre de Tangshan a coûté la vie à plus de 242 000 personnes. Bien qu'il y ait eu de nombreux observatoires sismiques dans la zone où le séisme s'est produit, les prévisions à court terme ont complètement échoué. Parce qu'il y avait peu d'activité de pré-chocs avant le

tremblement de terre de Tangshan et que d'autres phénomènes précurseurs sont apparus tardivement. En conséquence, le tremblement de terre de Tangshan a également été classé parmi les dix principales catastrophes naturelles du 20e siècle. À ce jour, il est toujours difficile de prévoir avec précision les tremblements de terre.

La technologie de résistance sismique est une méthode importante pour protéger les bâtiments cibles en les concevant et en les aménageant avant les tremblements de terre. La technologie conventionnelle de résistance sismique résiste aux forces des tremblements de terre en augmentant la force, la rigidité et la ductilité des éléments structurels du bâtiment, plus précisément en augmentant la taille de la section transversale des éléments structurels et en ajoutant des murs en béton armé pour résister aux tremblements de terre. Ces dernières années, les nouvelles technologies de résistance aux séismes sont devenues plus "souples", utilisant des dispositifs d'isolation et d'amortissement sismiques tels que des paliers en caoutchouc et des amortisseurs pour isoler et dissiper l'énergie sismique. Lorsqu'un tremblement de terre se produit, les dispositifs d'amortissement dissipent l'énergie des ondes sismiques dans le bâtiment en le comprimant, le pliant et le déviant de manière à modifier sa structure et sa forme, protégeant ainsi le bâtiment.

Au début des années 1990, le concept de cristaux phononiques a été proposé sur la base des cristaux photoniques. Les ondes acoustiques ou les ondes élastiques dans un cristal phononique constitué de milieux périodiques élastiques ne se propagent pas dans une certaine gamme de fréquences en raison de la diffusion de Bragg. En 1995, des chercheurs ont testé les propriétés de transmission acoustique d'une sculpture disposée périodiquement "Flowing Melody". L'existence d'une bande interdite acoustique a été démontrée expérimentalement pour la première fois. La caractéristique la plus distinctive d'un cristal phononique est la propriété de la bande interdite. La structure de bande d'un cristal phononique se compose de bandes interdites et de bandes. Dans la gamme de fréquences de la bande interdite, les ondes ne peuvent pas se propager dans les cristaux phononiques. Dans la gamme de fréquences de la bande passante, les ondes peuvent se propager normalement dans les cristaux phononiques.

En 2000, un métamatériau acoustique a été proposé sur la base du mécanisme de résonance locale. La bande interdite la plus basse de ce métamatériau acoustique correspond à une longueur d'onde de 300 fois la constante de réseau, ce qui permet

d'atteindre l'objectif de "contrôle de petite taille de grande longueur d'onde". La fréquence de la bande interdite du métamatériau acoustique est presque indépendante de la périodicité de la cellule unitaire, mais étroitement liée à la fréquence de résonance de la cellule unitaire de résonance. Les bandes plates et les bandes interdites peuvent être trouvées dans les structures de bande. La vitesse de groupe de l'onde dans le métamatériau acoustique est nulle à ce moment-là, l'onde ne peut donc pas se propager dans le cristal phononique.

Ces dernières années, des chercheurs inspirés par les cristaux phononiques et les métamatériaux acoustiques ont proposé des métamatériaux sismiques. La protection des bâtiments est réalisée d'une nouvelle manière : Les métamatériaux sismiques sont placés autour des bâtiments pour réfléchir et atténuer les ondes sismiques à des fins de protection.

Après un séisme, les vibrations mécaniques générées à la source se propagent à l'intérieur et à la surface de la Terre, formant ainsi des ondes sismiques. Les ondes sismiques peuvent être simplement distinguées en deux catégories principales: les ondes de masse et les ondes de surface. Dans les régions de champ moyen et lointain d'un tremblement de terre, les ondes de masse sont couplées sur la surface du demi-espace pour former des ondes de surface (également appelées ondes de Rayleigh). L'amplitude de la vibration décroît de manière exponentielle dans le sens de la profondeur du sol, de sorte que l'énergie des ondes de Rayleigh est presque entièrement concentrée près du sol. Les ondes de Rayleigh se trouvent généralement loin de la source du tremblement de terre. Les ondes de Rayleigh ont une grande amplitude, une décroissance lente, et peuvent se propager dans la surface de la terre plusieurs fois après un grand tremblement de terre et avoir encore une grande énergie. Par conséquent, dans le champ lointain d'un tremblement de terre, les ondes de Rayleigh sont plus destructrices pour les bâtiments que les ondes de masse et peuvent menacer les bâtiments à une plus grande distance. La conception et la recherche de métamatériaux sismiques pour les ondes de Rayleigh revêtent donc une grande importance.

Les métamatériaux sismiques, généralement basés sur la résonance locale et la diffusion de Bragg, utilisent les propriétés de la bande interdite pour isoler et atténuer les ondes sismiques, voire changer la direction de leur propagation. Les métamatériaux sismiques peuvent être placés autour ou au pied d'un bâtiment pour contrôler les ondes sismiques. La fréquence de résonance de la plupart des bâtiments construits par

l'homme est inférieure à 20 Hz, de sorte que la plupart des métamatériaux sismiques actuels sont conçus pour cette gamme. En outre, les chercheurs utilisent souvent des matériaux courants sur les chantiers de construction pour réduire le coût des métamatériaux sismiques, comme l'acier, le caoutchouc industriel et le béton.

Afin d'atténuer les ondes sismiques de Rayleigh dans une large gamme de basses fréquences, plusieurs types de SMs sont conçus dans cette thèse. Les caractéristiques de transmission des ondes sismiques de Rayleigh dans les SMs sont étudiées en combinant l'analyse du modèle théorique, la simulation numérique et l'investigation expérimentale. Les principaux contenus et conclusions se déclinent comme suit :

1. En se basant sur des expériences à l'échelle du laboratoire et sur la simulation numérique du SM constitué d'une plaque métamatériau sismique (SMP) à deux composants et d'un demi-espace, une nouvelle méthodologie de conception pour créer des SM afin d'atténuer les ondes sismiques de surface est démontrée. En outre, les expériences à l'échelle du laboratoire constituent également une base importante pour l'application du métamatériau sub-longueur d'onde à trois composants. Ensuite, un SM sous-longueur d'onde à trois composants, composé d'un SMP à trois composants et d'un demi-espace, est proposé. En analysant la propagation des ondes de Rayleigh dans les SM unidimensionnels (1D) et 2D dans la gamme de fréquences de la bande interdite à ultra-basse fréquence, on constate que les ondes de Rayleigh sont déviées à un certain angle et converties en ondes de masse. En résumé, le SM constitué d'une seule couche de SMP enterrée et d'un substrat possède une bande interdite à ultra-basse fréquence et peut convertir les ondes de Rayleigh en ondes de masse dans la gamme de fréquences de la bande interdite.

2. Un SM 1D en forme de T inversé (ITSM) avec une première bande interdite ultra-large (FBG) a été proposé en améliorant le SM en forme de pilier. Les effets des paramètres géométriques et matériels de l'ITSM sur le FBG ont également été discutés. On constate que l'apparition de la plaque augmente manifestement la fréquence centrale et la largeur de bande relative du FBG de l'ITSM. La structure de bande complexe de l'ITSM a été calculée pour analyser le mécanisme d'atténuation des ondes de surface. On constate que le FBG de l'ITSM est composé de deux parties. On constate que les modes de propagation des ondes de surface dans l'ITSM sont complètement différents dans les différentes parties du FBG. Enfin, un type d'ITSM 2D avec 25 cellules unitaires

est proposé dans des expériences de terrain à grande échelle, qui peut atténuer les ondes de Rayleigh dans une gamme de fréquences ultra large.

3. La propriété mécanique de la zone d'atténuation de la plus basse fréquence (LFAZ) du métamatériau élastique constitué de piliers sur un substrat a été étudiée numériquement. Il s'avère que la ZAF est immobile lorsque les distances entre les piliers changent. L'"effet de piégeage de l'arc-en-ciel" dans la deuxième zone d'atténuation (SAZ) a ensuite été démontré par simulation numérique et par des expériences. Par conséquent, pour un métamatériau élastique correctement conçu, il est possible de relier la limite inférieure de la SAZ et la limite supérieure de la LFAZ. Une large zone d'atténuation à partir d'une fréquence ultra-basse pour les ondes de surface peut être obtenue en utilisant simplement un type de structures artificielles sur un substrat. Dans le cas des ondes sismiques de Rayleigh, ces deux caractéristiques de la LFAZ et de la SAZ sont utilisées pour concevoir un type de métamatériau sismique en utilisant simplement un type de structure artificielle en acier sur un substrat de sol. Le métamatériau sismique proposé peut atténuer les ondes de Rayleigh de 5 à 22 Hz.

4. Une plaque métamatérielle conçue (MMP) avec des structures à bras de levier a été étudiée expérimentalement et discutée. Il est démontré qu'une large bande interdite pour les ondes de flexion apparaît dans une région à basse fréquence. L'analyse de propagation mesurée sur la face arrière de la MMP a démontré que les structures à bras de levier atténuent fortement les ondes de flexion. Enfin, les structures à bras de levier similaires sont introduites dans un demi-espace de sol pour obtenir les bandes interdites induites par l'amplification inertielle pour les ondes sismiques de surface dans une gamme de basses fréquences. L'avantage significatif est que les mécanismes d'amplification inertielle avec une petite masse peuvent atteindre une forte atténuation des vibrations à basse fréquence, une propriété qui devrait être réalisée pour les SMs.

5. Un métamatériau unidimensionnel à amplification inertielle est proposé, dont la cellule unitaire est composée d'une poutre de base, de deux bras et de trois articulations. Les résultats expérimentaux et simulés des transmissions des ondes de flexion dans la poutre nue, le métamatériau traditionnel et le métamatériau à amplification inertielle ont démontré que le métamatériau à amplification inertielle est capable d'isoler les ondes de flexion dans la bande interdite induite par l'amplification inertielle. Enfin, le mécanisme d'amplification inertielle intégré a été introduit dans un demi-espace de sol pour concevoir le SM. La structure de bande et les résultats de transmission ont montré

que le SM peut isoler les ondes sismiques de Rayleigh à des fréquences ultra-basses.

En résumé, plusieurs métamatériaux sismiques ont été conçus dans cette thèse pour isoler les ondes sismiques de Rayleigh. Ces métamatériaux peuvent atténuer les ondes sismiques de Rayleigh dans la gamme des basses fréquences et des ultra-basses fréquences, afin de protéger les bâtiments construits par l'homme et de réduire les dommages causés par les tremblements de terre. Ce travail fournit non seulement de nouvelles approches pour contrôler les ondes sismiques de surface à ultra-basse fréquence, mais aussi de nouvelles idées de conception pour diriger les ondes de surface.

Mots clés: Métamatériaux sismiques; ondes de Rayleigh; bande interdite; large-basse fréquence; dispersion inverse; résonance locale; amplification inertielle.

Abstract

The seismic metamaterials (SMs) make it possible to protect buildings in a way of efficiently attenuating and effectively controlling seismic waves. The SMs can attenuate seismic waves on the way of propagating to buildings, thereby protecting people's lives and property. Considering the multiple and high hazard of earthquakes, as well as some disadvantages that cannot be ignored in the seismic isolations, SMs have shown the application prospects. Several SMs are design in this thesis for isolating seismic Rayleigh waves. These SMs can attenuate seismic Rayleigh waves in the wide-low-frequency range and ultra-low frequency range, to protect man-made buildings and reduce the damage of earthquakes. This work not only provides new approaches for controlling seismic surface waves at ultra-low frequency, but also provides new design ideas for steering surface wave.

Keywords: seismic metamaterial; Rayleigh waves; bandgap; wide-low frequency; Inverse dispersion; local resonance; inertial amplification

Résumé

Les métamatériaux sismiques (SMs) permettent de protéger les bâtiments en atténuant et en contrôlant efficacement les ondes sismiques. Les SM peuvent atténuer les ondes sismiques qui se propagent vers les bâtiments, protégeant ainsi la vie et les biens des personnes. Compte tenu des risques multiples et élevés des tremblements de terre, ainsi que de certains inconvénients qui ne peuvent être ignorés dans les isolations sismiques, les SM ont montré des perspectives d'application. Plusieurs métamatériaux sismiques ont été conçus dans cette thèse pour isoler les ondes sismiques de Rayleigh. Ces métamatériaux peuvent atténuer les ondes sismiques de Rayleigh dans la gamme des basses fréquences et des ultra-basses fréquences, afin de protéger les bâtiments construits par l'homme et de réduire les dommages causés par les tremblements de terre. Ce travail fournit non seulement de nouvelles approaches pour contrôler les ondes sismiques de surface à ultra-basse fréquence, mais aussi de nouvelles idées de conception pour la direction des ondes de surface.

Mots clés: Métamatériau sismique; ondes de Rayleigh; bande interdite; large-basse fréquence; dispersion inverse; résonance locale; amplification inertielle